Universidad de Concepción
Dirección de Postgrado
Facultad de Ingeniería Agrícola
Programa de Doctorado en Ingeniería Agrícola con mención en Recursos Hídricos
en la agricultura

Estimación de evapotranspiración espacialmente distribuida mediante un enfoque GEOBIA

(Estimation of spatially distributed evapotranspiration through of GEOBIA approach)

Tesis para optar al grado de Doctor en Ingeniería Agrícola con mención en Recursos Hídricos en la Agricultura

DAVID ALEXANDER FONSECA LUENGO
CHILLÁN-CHILE
2015

Profesor guía: Mario Lillo Saavedra
Departamento de Mecanización y Energía,
Facultad de Ingeniería Agrícola.
Universidad de Concepción.
Profesor guía: Octavio Lagos Roa
Departamento de Recursos Hídricos,
Facultad de Ingeniería Agrícola.
Universidad de Concepción.

Estimación de evapotranspiración espacialmente distribuida mediante un enfoque GEOBIA

Aprobada por:

Mario Lillo Saavedra	_____
Electrical Civil Engineer, PhD.	Advisor
Octavio Lagos Roa	_____
Agricultural Civil Engineer, PhD.	Advisor
Consuelo Gonzalo Martín	_____
PhD. in Physics Science	Co-Advisor
Eduardo Holzapfel Hoces	_____
Agricultural Engineer, PhD.	Internal evaluator
María González Rodriguez	_____
Agricultural Engineer, PhD.	Program director (s)

Acknowledgements

Author (David Fonseca-Luengo) thanks to the National Commission for Scientific and Technological Research (CONICYT) for support the accomplishment of the Doctoral Thesis.

Authors also thanks to grants FONDEF D09I1069, FONDECYT 11100083, FONDAP 15130015, BMBF-CONICYT 231-2010 and ITECMA2 Laboratory (Faculty of Agricultural Engineering, Universidad de Concepción, Chillán, Chile.), in which the current research has been framed.

Dedicatoria

Si están leyendo esto supongo que la tesis salió bien :P, eso espero. Bueno, en la sección de agradecimiento puse lo que DEBÍA poner, pero en realidad acá van mis verdaderos agradecimientos.

Muchas gracias a Mario Lillo, que siempre cumplió su rol como profesor asesor de mi tesis, pero que además siempre me apoyó y aconsejó en el plano tanto como personal y profesional para llegar a buen puerto con mi tesis, y sigue haciéndolo ya no como profesor sino como un partner.

Pelao (Angel), muchas gracias por siempre ofrecer tu ayuda no sólo en el desarrollo de códigos (que tanto amas jajaja) sino también en discutir temas relacionados a mi tesis, y por sobretodo por la amistad que me diste, apoyo en mis momentos difíciles, que si que hubieron. Y feliz porque la amistad va a continuar.

Un especial agradecimiento a los profesores de mi comisión, de los cuales recibí su apoyo y comprensión en todas las etapas del desarrollo de la tesis. En especial en el último periodo en el cual estuve siempre al debe con las fechas :(. A las secretarias mas bellas (Alesita, Eugeee y Clarita) que siempre estaban ahí cuando pedía ayuda.

Agradezco con todo mi corazón haber pasado por el Doctorado, no sólo por el grado académico que he conseguido, sino que principalmente por haber conocido tanta gente bella. Primero pude relacionarme con compañeros de mi carrera y de mi generación que por cosas de la vida no había podido compartir tanto. Waldo (mi jefe), el cual con su alegría y capacidad de reírse de sí mismo compartimos muchos buenos momentos, nos apoyamos y pudimos sacar adelante los desafíos que se nos presentaron. Aún recuerdo cuando trabajábamos en la oficina chica con la María Paz Lisboa, Matías Mendoza, Feliciano Aguilera...Ahí olvido un poco el orden de la gente con la cual estuve...mi memoria es frágil :P...pero recuerdo a Felipe (de la escuela agrícola, una maquina cavando jajaja), la Marcela, Gustavo, Chacal, David Mellado, Shundito (gran persona Jonathan), Lucares, Marcelo, Labrin. Conocí a las hermosas Oruga, Cami, a la siempre wena pal webeo Marisel jjaja,,a esa personita tan especial como lo es la MeriPiz Rojas, a la flaca mas bella de la Claudiña, la Dani Aguayo la morena más simparicaaaa...a mi Vivii...a los cauros del equipo del campeonato agrícola donde shundo fue el arquero revelación jajaja..a los cauros del equipo del campeonato agrícola con el Camilo (rojo, jose, rodo... :))...A Braulio y Jimmy de Ecuador (algún día iré y les cobraré la invitación ;)), a mi morena maravillosa de Panamá (Haydee). A los malandras de posgrado, Gabriel, Walter, Julito,,el malandra mayor, quien

más que Javier y esos 5 minutos insuperables jaja...a Lecaros, el Feña (que junto a Javier y Felo podrían hacer un trio perfecto jajaaj), Denisse (cuidate en la motooo)...al Mathias y su especialización en perforaciones en casetas de riego....pucha estoy seguro que me faltan muchas personas que de verdad fueron muy bellas en mi estadía en la UDEC en mi etapa de posgrado, ya que me alegraban los días y me servían de apoyo, un apoyo que es necesario cuando la presión está puesta en lo que debes rendir, en lo que dices y en lo que enseñas en el caso de guiar a algún compañero o realizar alguna ayudantía. Mis disculpas y cariños a todos los que se me olvidan :P.

Dedico esta tesis a mi madre, que casi nunca me preguntaba sobre mis estudios, no porque no le preocupara sino porque siempre confió en mi, gracias mami. A mi hermano le podré decir que finalmente la terminé, así que ya no podrá molestarme más con esto jajaja. Agradezco a Francisca, ya que siempre sentí tu apoyo y comprensión en el desarrollo de mi tesis de pregrado y la tesis de doctorado, gracias pancha.

Esta tesis o el grado no la mencionaré para que los demás sepan lo que he logrado académicamente, sino que siempre la mencionaré tratando de llegar a recordar las buenas experiencias personales que viví en la Universidad en esta oportunidad, mi segunda oportunidad.

Y Finalmente....dejaré de ser estudiante, o al menos formalmente :).

Contents

List of Figures

List of Tables

Page

Part I

Abstract

Estimation of the crop water requirement is critical in the optimization of agricultural production process, due yield and costs are directly affected by this estimation. Important benefits of a correct estimation of water requirement are the increasing irrigated area, and a high production due a better root condition.

Actually in most cases the crop water requirement, represented by the Evapotranspiration (ET), is estimated through local approaches. Some of these approaches use classical and novel techniques, that can estimate ET with high accurate but precluding the spatial crop representation of ET.

In this sense, remote sensing appears as a way to ET estimation considering spatial and temporal variability. ET models using satellite images have been developed in the last decades, using in most cases the surface energy balance which has generated good ET representation in different study sites. One of these models is METRIC (Mapping Evapotranspiration at high Resolution using Internalized Calibration) that using a simple and physical-empirical basis solving the surface energy balance to estimate ET.

The main drawback of METRIC model is the low robustness in the selection of a pair of parameters called anchor pixels, that in the original version of METRIC were selected by an operator, but aiming to standardize this selection and avoid the effect of different operator criteria an automation was proposed. Although this automation standardizes the model response, this requires a selection of an area where to find these anchor pixels, moreover a high sensibility to different anchor pixel candidates still can be observed. In addition, where this automation is implemented selecting different areas where anchor pixels are found, important differences in the ET estimation are generated.

In this dissertation an object based image analysis (GEOBIA) is implemented to anchor objects (changing the approach from pixel to object) identification. With the GEOBIA approach, segmentation and classification processes are used to a correct selection of segments in the image that fulfill the requirements for anchor objects, considering spectral and contextual information. The implementation of this approach aiming to increase the model robustness regarding to anchor objects selection.

Image segmentation was done using an adaptation of SLIC algorithm proposed to carry out a hierarchical segmentation, in order to identify the optimal scale segmentation for each parent segment. While, classification was divided in two processes: a primary classification using Random Forest that was trained considering seasonal and humidity conditions; and a post-classification step considering contextual and statistical information.

Results showed that the proposed GEOBIA approach allows to improve the robustness

in the selection of anchor objects, which was validated through comparison with original selection of anchor pixels in two scenes, moreover, entire set of scenes where the methodology was implemented showed a decrease in the variability of the result.

Homogeneity analysis showed that ET objects with classes where crops can be found have low intra-object variability and high inter-object separability. These results are a good indicator of that segmentation process allowed to generate homogeneous segments without loss of spectral characteristics and correctly separated from one another.

Validation of the proposed methodology comparing estimated with measured data showed that the proposed methodology generates a slight error greater than original model. This result suggest that some improvements to final selection of anchor objects can be carried out, in this sense, could be considered different metrics to describe the segments, additional maps, and to explore other relations between segments considering spatial, temporal and hierarchical characteristics.

Part II

Introduction

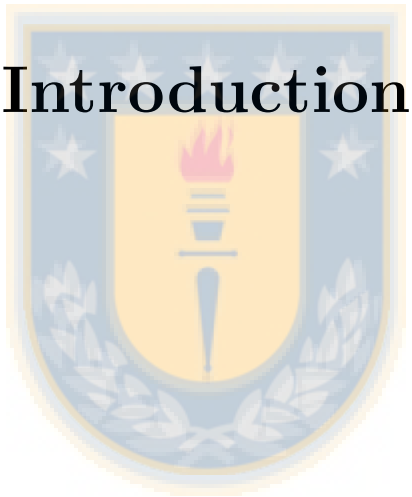

Water requirement estimation is performed through the quantification of ET, using local estimation or quantification models. In Allen et al. (2010), it is stated that, although the ET estimation using lysimeters, Eddy covariance systems and Bowen ratio are accurate, there are still limitations extrapolating local estimates at regional scale. It is also stated in Allen et al. (2010) that local estimates do not represent the real amount of crop ET with spatial and temporal variation caused by the rainfall heterogeneity, soil, vegetation types, density, climate variability and phenological stage. About this, remote sensing allows ET quantification in both local and regional scales, monitoring the crops in temporal and/or spatial sense.

Remote sensing is the method used for information extraction without a direct contact with an object of interest. Nowadays, this is performed by processing and analysis satellite imagery captured by sensors mounted in spacecrafts. The increasing availability of imagery allows to perform the crop monitoring, and use these images as a tool for crop management. In this sense, ET estimation models that using satellite imagery have been developed, considering different approaches and input data.

METRIC (Allen et al., 2007) model is one of the latest and widely used models of ET estimation over full coverage crops through of surface energy balance using multispectral satellite imagery with optical and thermal bands. METRIC is based on SEBAL (Surface Energy Balance Algorithm for Land) model (Bastiaanssen et al., 1998a,b), that did a great contribution to solving the estimation of sensible heat flux from satellite imagery through the relation found between the temperature difference at different heights and surface temperature considering pixels of the same images with extreme water conditions. The main contribution done by METRIC was the model calibration by means the use of reference ET which allows an inclusion of the local ET conditions.

In Gowda et al. (2008), a description of the main methods used in ET models using satellite imagery was presented. The main methods are those based on surface energy balance and models that estimate the relationship between the ET and reference ET (ETr) through of a coefficient.

In last models that use a coefficient, two approaches can be followed. On one hand, to generate the coefficient from ground data following the assumption that crops have a standard management (without water restriction and with optimal soil condition). These ensure that the fraction between ET and ETr corresponds to crop coefficient (Kc), widely used in agriculture (Kc= $\frac{ET}{ETr}$). On the other hand, if the coefficient is generated from remote sensing data, the relationship is similar to Kc but with the exceptions that

assumptions related with water restriction and management are not ensured. In this work, coefficient generated from remote sensing data will be called ET_rF using same denomination of METRIC and SEBAL models. Models that use crop coefficient relations (Kc or ET_rF) are widely implemented with high spatial resolution images, because the majority of these kind of images lacks the thermal band, which does not allow to estimate ET through surface energy balance models. NDVI-Kc (Kc or ET_rF) relation is the most used of these models, where NDVI refers to *Normalized Difference Vegetation Index*. NDVI-Kc estimates Kc from NDVI, which is then multiplied by ETr estimated from ground data. It is stated in Gowda et al. (2008) that, although the NDVI-Kc models are relatively easy to implement, require consider the water stress and calibration for each individual crop.

METRIC and SEBAL are among the mostly used models to generate ET maps through satellite imagery at this time. This is because of the physical basis, relatively easy to implement models and the good results observed in different study sites. However, despite the good results obtained by implementing these models, a sensitive dependence of the results to the selection of anchor pixels that have to be identified on the image for deployment of models SEBAL and METRIC has been found (Long et al., 2011). The anchor pixels consist of two pixels located in the scene of the satellite image with extreme water conditions. While the hot pixel is a bare soil pixel without evaporating water, the cold pixel corresponds to a pixel with a full vegetation cover without water restrictions. The anchor pixels are used to estimate the temperature difference between the surface and the air through the relation developed in Bastiaanssen et al. (1998a,b), being this a fundamental parameter in the estimation of sensitive heat flux in the scene and therefore the crop ET estimation as residual of the surface energy balance.

In Choi et al. (2009) there is a comparison between three models to estimate ET from satellite imagery, METRIC, TSEB (Two-Source Energy Balance) and TIM (Trapezoid Interpolation Model). The results showed that METRIC and TSEB presented a better adjustment of the estimations of heat fluxes regarding the ground-based measurements. However, with a further analysis of the results discrepancies appeared in the estimations in low vegetation cover zones (Leaf area index less than 2) concluding that, in the METRIC model, special attention should be paid to both the selection of the hot pixel and the parameter that defines the fraction of reference ET that the hot pixel evaporates.

Long et al. (2011) provides a sensitivity analysis of the SEBAL model regarding the input of model and the anchor pixels. The sensitivity of the model, related to the scale

and spatial resolution of the image was also assessed. The results showed that SEBAL model is highly sensitive to the selection of anchor pixels, especially to the hot pixel. It was also observed that the model results vary in relation to the employed scales and the spatial resolution of the image. Long and Singh (2013) evaluated the RMSE (Root mean square error) of METRIC model in the evaporative fraction produced by 3 anchor pixels (3 cold and 3 hot pixels) versus flux tower measurements, the RMSE ranged from 0.08 to 0.13, showing that despite a manual selection of good anchor pixels candidates, exist a probability of error in the estimation. In this same sense, Morton (2013) showed the differences in the evaporative fraction estimated by 5 trained users, that reinforces the high sensitivity of the model to manual selection of anchor pixels.

In Choragudi (2011) a sensitivity analysis of the METRIC model was performed in relation to several input, the information from satellite imagery and anchor pixels. The results showed that the METRIC model is particularly sensitive to selection of anchor pixels, especially to the hot pixel which is also showed in Wang et al. (2009).

This model sensitivity regarding to anchor pixel selection was tried to be reduced via automation of the selection of these parameters. In Morton (2013) an automatic methodology to select the anchor pixels was proposed. The automation generated good estimation compared with measurement on ground, but the main problem was the use of a key assumption about a similarity across image dates and study areas. In Allen et al. (2013) was proposed a methodology to try to avoid the high variability of the results due different criteria of supervisors that select the anchor pixels. This automation helps standardize this selection but also needs to be supervised by an operator that select the areas of interest where the anchor pixels can be found. These areas of interest are done up of agricultural zones where vegetation covers without water restriction and bare soil without water contribution can be found. Also, with this methodology there is still the possibility of selecting an incorrect anchor pixel that does not fulfill the requirements due to the sole use of dichotomous rules that are applied to the spectral characteristics of the pixels, not taking into account textural, morphological or contextual characteristics.

Nowadays, most water resource management in agriculture does not take into account the intra-heterogeneity of farmland, using the same amount of water on cropland regardless their differences in behavior or state. In this sense, satellite imagery appears as the tool for the identification of variability in temporal and spatial scale, allowing the crop analysis and management by homogeneous sectors.

The actual ET estimation models based in satellite images still have limitation about

the use of pixel based approach to generate ET maps, causing that maps are composed by a large ET points that do not provide a clear information to farmers. This is because the pixels, by themselves, have not information about shape, variability or neighborhood, which do not allows the identification of areas with a specific behavior (Blaschke, 2010). Moreover, this pixel based information is not useful for farmers since the manage their crops considering management zones instead of management points or pixels.

GEOBIA (Geographic Object based image analysis) approach correspond to the development of methods to divide images into objects that are useful for information extraction (Hay and Castilla, 2008). GEOBIA approach have the same guidelines than OBIA (Object based image analysis) approach, but OBIA is applied in Computer Vision and Biomedical field while GEOBIA is used in images from remote sensing characterized by have a geographical meaningful. From now on, the term GEOBIA will be used to designate both approaches, GEOBIA and OBIA, considering that this dissertation is developed in the field of remote sensing.

GEOBIA approach has been used more widely since approximately the year 2000 due to its advantages over the pixel based approach in spatial information extraction from satellite imagery (Blaschke, 2010). GEOBIA approach has been implemented to reduce noise generated by the large amount of pixels from covers in high or very high resolution images and to extract more relevant information from objects, such as size, shape, location, variability and cover classes. Another advantage of GEOBIA over the pixel based approach is the considerable computing workload reduction of the classification process because it considers image objects instead of pixels (Hay and Castilla, 2008).

Segmentation and classification are the main processes in GEOBIA (Gao and Mas, 2008). Segmentation consists on separating the images into several regions or segments that have homogeneous features, among others, spectral and/or textural. After this process, the generation of features is performed using spectral, textural, morphological and/or contextual information for each individual segment. Classification consists of groups generation from similar regions created in the segmentation process using its features (Vieira et al., 2012).

The main differences in the GEOBIA implementations are the methods used for the segmentation and classification, and the inputs of both processes. In Castillejo-González et al. (2009), pixel and GEOBIA approaches using different supervised classification methods and spatial resolution images are evaluated, concluding that the use of GEOBIA improves the classification of farmland covers.

An associated concept to the implementation of GEOBIA in remote sensing is the spatial scale. The scale is defined as the period or space over which the signals are integrated or smoothed to deliver a message (Allen, 1982). Humans are capable of identifying multiple scales and analyzing them naturally, integrating information from multiples scales or considering only one. This analysis is known as multi-scale analysis and it is a matter of interest in the remote sensing field because the selection of one or another scale can generate different information of a same scene (Burnett and Blaschke, 2003). Levin (1992) proposed that the problem is not the recognition of the correct scale, but the identification of phenomena at different scales and their interaction. This analysis suggests that remote sensing research must consider different scales in order to identify and analyze the scene.

GEOBIA approach allows the incorporation of contextual, variability and hierarchical information to improve the selection of classes of interest in the image, as in the METRIC model are the anchor pixels.

Finally, scenario previously detailed encourages the design and implementation of a methodology allowing to increase the robustness in the ET estimation using METRIC model, via GEOBIA approach in the automatic anchor pixel selection (designated as anchor objects in the GEOBIA context) considering spectral, textural and contextual information.

Part III

Hypothesis and Objectives

0.1 Hypothesis

For the realization of the present Doctoral Thesis following hypotheses were proposed:

- Through GEOBIA approach the generation of homogeneous evapotranspiration objects at different scales is possible.

  This hypothesis is based in the conceptual definition of the segmentation process, i.e, the subdivision of an image into homogeneous regions considering homogeneity and heterogeneity criteria (Baatz et al., 2004).

- The implementation of ET estimation model through GEOBIA approach allows to improve the robustness in the selection of anchor pixels.

  GEOBIA approach is a relatively novel methodology that allows to improve the generation of useful information based in spatial patterns, compared with the classical pixel approach analysis. This useful information is an advantage that can be used to incorporate them in the identification of anchor pixels using different criteria, e.g., textural, morphological and/or contextual.

0.2 Main Objective

- To design, implement and evaluate a methodology to ET estimation through GEOBIA approach.

0.2.1 Specific Objectives

1. To design the GEOBIA architecture to ET estimation.
2. To design and implement the methodologies to multi-scale segmentation and optimal scale definition of objects.
3. To design and implement the methodology to automatic selection of anchor objects.
4. To validate the robustness of anchor objects selection, ET estimated and ET object.

0.3 Expected contributions

1. ET estimation using the GEOBIA approach and surface energy balance would increase the robustness of the automatic selection of anchor objects compared to the

classical selection of anchor pixels, due to the incorporation of spectral, contextual and/or morphological information in the selection.

2. Considering the GEOBIA approach, ET objects can be generated at different spatial scales, which provides the ability to address attributes at different levels. This additional information can be used by final users to analyze different management units with an area-based behavioral approach.

Part IV

Global Methodology

The first Chapter highlights the need of carry out this Thesis. In this sense, Chapters 1 shows the sensitivity of METRIC model regarding to some intermediate parameters and inputs, generating relevant information about the importance of some parameters and relationship between parameters and ET estimation. But mainly, this Chapter stated the robustness problem referent to anchor pixel selection, which is the main problematic that is addressed in this Thesis.

The remaining parts of the Thesis development are explained below. The main proposal of the methodology is related to the identification of uniform areas, represented by segments, to select the anchor objects. In this sense, Figure 1 shows the principal processes of the methodology: **Preprocessing**, **Training** and **Implementation**.

The goals of the preprocessing step are to correct the gap of pixels of Landsat-7 EMT+ and to generate an uniform data-set from satellite images. In this sense, a brief evaluation of 3 methods to the gap filling process of Landsat-7 ETM+ images is showed in the Chapter C in the Appendix.

The objective in training process is that a machine learning be able to classify any scene in a specific number of classes previously settled. This is done through a training process using Regions of Interest (ROI) generated by manual delineation in specific scenes. To allow the use of homogeneous information, training is carried out over segments instead pixels, for this reason an oversegmentation is applied previously to classifier generation. This is a primary classification, then the objects are re-classified to identify anchor objects. Full explanation of training process is done in Chapter 2.

Classifier, previously generated, is implemented to classify the segments of new scenes, producing the desired classes. Moreover, as is showed in the Figure 1, an **Anchor Objects Identification** process is implemented through a contextual and statistics rules. Finally, the METRIC model is implemented considering two experiments, over original pixels and over segments at optimal spatial scale. Full details of this process is explained in Chapter 3, where results of the proposed methodology are generated and validated.

In Appendix some researches that contributed to accomplish the Thesis are shown. In this sense, Chapter A is a research carried out to evaluate how can improve the METRIC model if some parameters are locally calibrated. In addition, Chapter B is a research that addresses the generation of optimal scale object through a hierarchical segmentation.

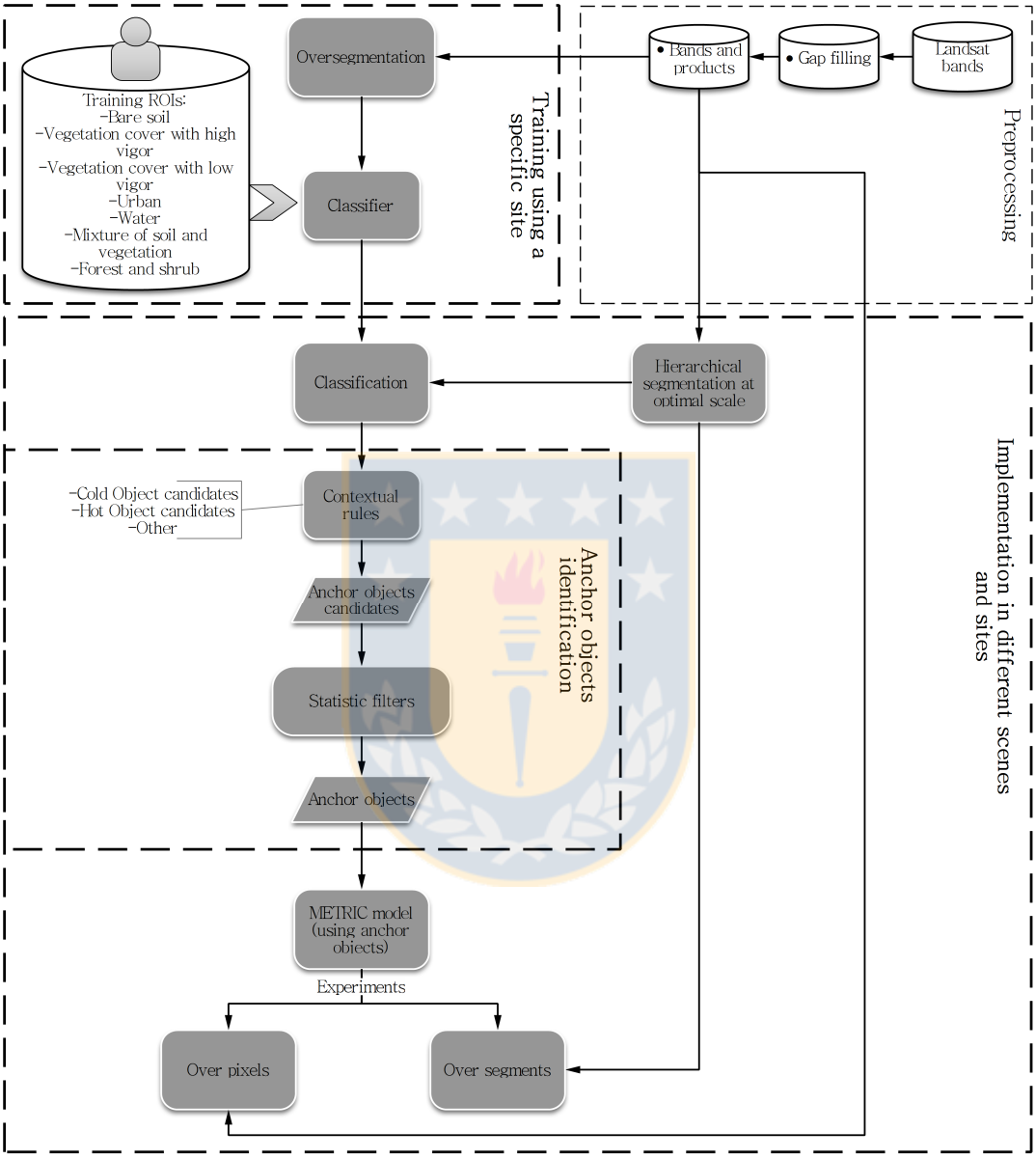

Figure 1: Conceptual diagram of the proposed methodology.

Part V

Results of the proposed methodology

Chapter 1

Sensitivity analysis of METRIC model

1.1 Introduction

SEBAL and METRIC models are the most popular methods to estimate ET using satellite images at medium-high scale considering them being a good combination between a physical based approach and not very complex process to generate ET maps. SEBAL model has been implemented in several locations with different climatic conditions, with accuracy in the results ranging from 67% to 95% for instantaneous ET, and 70% to 98% for daily ET (Bastiaanssen et al., 2005). In Tang et al. (2009) is showed that instantaneous and daily ET estimation have 10% and 15% error, respectively. Despite this good result in the ET estimation, additional analysis on the response of the model to input and intermediate parameters is necessary.

As mentioned in Part II of this dissertation, some sensitivity analysis of SEBAL and METRIC models has been carried out addressing the input, intermediate parameters and domain scale which based the analysis in a possible error in the estimation of an input, or if some values in intermediate parameters were incorrect. Although these results generated an extensive amount of information about the response of METRIC/SEBAL model in function of most of the parameters, some of the research do not consider the possible error in realistic conditions, limited to an analysis on a range based on a percentage of the basic condition. In this sense, in a sensitivity analysis done by Tasumi (2003) on METRIC model showed a minimal sensitivity to surface roughness, even if doubling this value, but

this result hides a possible condition since the values of surface roughness for different land covers can vary from 0.02 to 1 m, for pasture and tree respectively.

Important parameters in METRIC and SEBAL models are the anchor pixels. These are two pixels in extreme water condition: the cold pixel which is a full vegetative pixel without water stress; while the hot pixel is a bare soil pixel without soil moisture. In the first approaches of these models, the selection of these anchor pixels was performed by an operator, but the possible error induced by different criteria of these operators became necessary to investigate about the automatic selection of anchor pixels. In Allen et al. (2013) a methodology to automation of anchor pixels selection was proposed using statistical analysis of NDVI (Normalized Difference Vegetation Index) and surface temperature. Another proposal was done in Morton (2013), where an iterative statistical analysis considering simulations and assumption of population distribution was designed. These approaches have good results but could need some calibrations for a new landscape.

In this research a sensitivity analysis of METRIC model was made over a study site located in the Central Valley of Chile considering the following parameters: reference Evapotranspiration (ETr), wind speed (WS), near surface vapor pressure (ea), albedo, surface temperature (Ts), reflectance at the surface in different bands (Refs_{band}), surface roughness (zom) for cold anchor pixel and zom for the analyzed crop. Furthermore, a sensitivity analysis of METRIC depending of different anchor pixels candidates was done.

1.2 Materials and Methods

The full description of METRIC model can be found in Allen et al. (2007, 2010), while a brief description is shown in Chapter D.

In this research the sensitivity analysis is implemented by varying the analyzed parameters and computing the *fraction of reference evapotranspiration* (ET_rF, which is the fraction of estimated ET and ETr, $\text{ET}_r\text{F}= \frac{ET}{ETr}$) and instantaneous ET ($\text{ET}_{ins}$). ET_rF is analyzed for two reasons: this output of METRIC is used to daily ET calculation, therefore the impact of the parameters on ET_rF directly affects the daily ET; considering ET_rF, possible errors in the incorporation of daily ETr from meteorological station are avoided. ET_{ins} is analyzed since this is the primary output of the model derived from the surface energy balance. This methodology (varying parameters and analyzing the output) was implemented in other researches (Tasumi, 2003; Long et al., 2011; Choragudi, 2011) being it a simple way to evaluate the influence of each parameters in the estimation model.

An important step is the definition of the range for each parameters analyzed, since an erroneous range can hide or increase the sensitivity of some parameters. Different approaches to define the ranges were used. For ETr a percentage of possible error in the estimation was used based in Estévez et al. (2009), where it was stated that around a 20% of error in ETr can be possible incorporating random and systematic errors. WS was varied between +-50%, based on similar research (Long et al., 2011; Choragudi, 2011). ea is not a recurrently analyzed parameter, but in this research it is considered because it is an input in the atmospheric correction process, and this analysis can give a guide to replace it for a best process. In our case, the ea varied between +-20% from base condition. Albedo is an important parameter to analyze because it has been shown that random deviation, canopy structure and shadows can affect the albedo values (Choragudi, 2011). Also, estimation of albedo for inclusive similar sensor, e.g. Landsat-7 and Landsat-8, shows differences that can likely affect the ET estimation. Based on the range of albedo for soil and vegetation covers, albedo was varied +-20% from the base condition. About Ts, results in Tasumi (2003) showed that an uncorrected surface temperature can generate an error of more than 5 degrees. However, this error was seen in extreme hot pixel, while in more cold surface the error was less. Following this, Ts was varied by +-2°K from base condition based on that inaccuracy in Ts estimation (Coll et al., 2010). Refs_{band} was varied in a +-50% from base condition, based on that shadow effect can vary the value of Refs_{band} in this range (Leblon et al., 1996). Finally, the sensitivity for zom was analyzed considering an erroneously estimation for the cold pixel (zom_{cp}) and for a specific crop pixel zom_{sp}. zom_{cp} was varied considering the possible error generated by the empirical equations used to estimate it. This is that there exist a possibility that a cold pixel could be a full covered crop pixel or a pixel composed by trees, ranging the zom_{cp} from 0.2 to 1 m, respectively. While analyzing a specific pixel from our study site (in this case Sugar Beet crop), the possible errors in the estimation of zom_{sp} should be less, due to that the equations to estimate it were developed in Tasumi (2003) and Allen et al. (2007) for annual irrigated crops, like Sugar Beet. In this case zom_{sp} was varied in +-50% from base condition. However, a third condition can be analyzed: if the specific crop analyzed is a tree crop, the error in the zom estimation could be greater, in this case the zom for hypothetical tree crop (zom_{tc}) was analyzed ranging from 0.2 to 1 m.

In Table 1.1 the ranges for all parameters are shown. It should be also mentioned that two scenes were evaluated, 2012-092 and 2012-364 (where the denotation consider the year and the Julian day). The values of base condition for both scenes are shown in

Table 1.2. In addition, values of NDVI for Sugar beet crop; and Ts, NDVI, fraction of evapotranspiration (ETrF, which corresponds to) for cold and hot pixels are shown (all of them with a respective sub-index *cold* or *hot*).

Parameter	**Range**
ETr	+-20%
WS	+-50%
ea	+-20%
Albedo	+-20%
Ts	+-2°K (around 0.68%)
Refs_{band}	+-50%
zom_{cp}	0.02 to 1
zom_{sp}	+-50%
zom_{tc}	0.02 to 1

Table 1.1: Ranges of variation for all parameters analyzed.

Parameter	**Base value**		**Unit**
	2012-092	2012-364	
ETr	0.43	0.67	mm*h^{-1}
ET_{ins}	0.41	0.57	mm*h^{-1}
ET_rF	0.95	0.85	-
WS	4.39	3.79	m*s^{-1}
ea	1.18	1.24	KPa
Albedo	0.15	0.21	-
Ts	293.6	296.0	°K
Refs_{NIR}	0.44	0.58	-
zom_{cp}	0.07	0.06	m
zom_{sp}	0.07	0.09	m
Ts_{cold}	292.8	294.7	°K
Ts_{hot}	302.3	306.1	°K
NDVI_{cold}	0.78	0.76	-
NDVI_{hot}	0.21	0.34	-
NDVI_{crop}	0.79	0.83	-
ETrF_{hot}	0.1	0.33	-
ETrF_{cold}	1.0	1.0	-

Table 1.2: Values of base condition.

In the sensitivity analysis based on the anchor pixels a range of variation was not used, since this is not a realistic scenario. The analysis was performed considering different

anchor pixels candidates, so that the sensitivity is estimated for different possible anchor pixels selected, either by a different operator that selects the pixels, or by changes in the automatic criteria for pixels selection. The selection of these anchor pixels candidates was implemented using the proposal of Allen et al. (2013).

To evaluate the sensitivity for each parameter, a sensitivity coefficient was calculated. This coefficient allows comparing the sensitivity of different parameters and a better interpretation of the results. In Gong et al. (2006) a non-dimensional relative sensitivity coefficient that analyzes the model output and the punctual value of the parameter analyzed (equation 1.1) is showed. This coefficients was first adopted by McCuen (1974) and allows to compare variables with different dimensions and ranges of values. S_i represents the fraction of change in p_i (where i denote the parameter analyzed) that is transmitted to the Out of model, i.e. a S_i equal to 0.1 would suggest that a 10% of increasing in p_i may increase the Out by 1% (Aydin and Keçecioğlu, 2010). The coefficient is calculated from the values resulting from each model simulation considering the variation of the parameter analyzed.

$$S_i = \frac{\partial Out}{\partial p_i} * \frac{p_i}{Out} \tag{1.1}$$

1.2.1 Study site

In this research, one area was analyzed, with coordinates in the center of the image of 36.53° S and 72.10° W, with an extension of 25x25 kilometers. The climate is warm temperate, the annual mean temperature is 14°C, with a short dry season and annual rainfall that varies from 1,000 to 1,300 mm (Novoa et al., 1989). The study site corresponds to a central valley located in central-south of Chile, predominated by annual crops and some orchards. In the scene a city (Chillán) and the principal river of the region (Ñuble river) can be observed.

Sensitivity analysis was implemented over a rotation Sugar Beet crop of Sandrina, Magnolia and Donella varieties, which can be observed in Figure 1.10 in 5952200 S and 219000 W coordinates (WGS 84 / UTM 19S). The plantation frame is 0.5 m between rows and 0.07 m between plants, with a center pivot irrigation system with I-Wob emitters. The total area of the farm is around 450 ha, and the area of crop covered for the center pivot (study site) is around 17 ha. The extraction of information from the images was carried out considering a window of 3x3 pixels around the location of a Surface Renewal station

installed over the crop (for more detail about the station please refer to *Site 2* in Chapter A).

1.2.2 Data set

Images were captured by the ETM+ sensor on board of Landsat-7 satellite. Images corresponding to the *path*/*row*: 233/85 were used, which were downloaded from the USGS Glovis official site (http://glovis.usgs.gov), with 1T preprocessing level. The year and DOY (Day of year) of each scene used are: 2012-092 and 2012-364. These two scenes allow evaluating the different responses of METRIC in different phenological conditions.

Due to the failure in the "scan line corrector" (SLC) mechanism of the Landsat-7 EMT+ sensor on May 31, 2003, the images required the implementation of a preprocessing consisting of the gap filling process of pixels without information. In order to achieve this, the method proposed by Scaramuzza et al. (2004) (later published in Storey et al. (2005)) was implemented. In Chapter C an evaluation of different methods to gap filling is showed.

Meteorological parameters to estimate ETr were obtained from a meteorological stations network, with website http://agromet.inia.cl/, this is managed by the *Instituto de Investigaciones Agropecuarias* (Agricultural Research Institute appointed under the Chilean Ministry of Agriculture).

1.3 Results and discussion

1.3.1 Sensitivity analysis for albedo

The albedo corresponds to the fraction of incident radiation that is reflected by the land cover. It is calculated by METRIC using a empirical model that considers different weights determined for each band by Tasumi et al. (2008). The importance of the analysis about the effect of albedo in ET, arises because there are different methodologies to estimate albedo from satellite images, which can generate different values. Furthermore, since the launch of Landsat-8 satellite, new sources of images to implement the METRIC model exist. The problems appear since the spectral ranges of the bands in Landsat-8 are different that Landsat-7, therefore weights used in Landsat-7 are unable to be used in the albedo estimation. This analysis seeks to find the importance that the albedo can have in the estimation of ET, considering scenarios with differences in the procedure to estimate it or different sources of information (sensors).

Figure 1.1 shows that ET_rF and ET_{ins} decrease with an increment of albedo. Albedo affects the estimation of net radiation (NR) and soil heat flux (G), generating a decrease of NR due mainly to an increase of the outgoing shortwave radiation, and a direct proportion of change of G (insignificant considering the change of NR). Reduction of NR due to an increase of albedo, generates an important reduction of ET_{ins} since there is less available energy to use in evapotranspiration process.

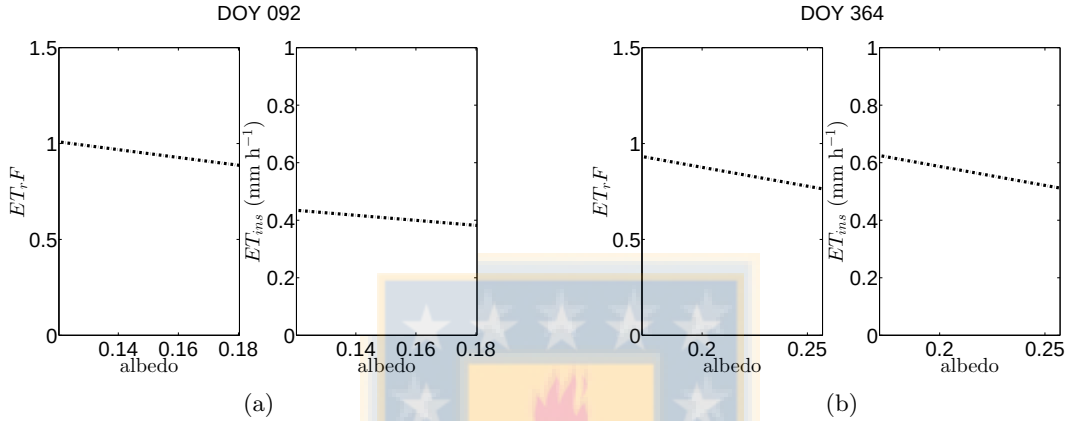

Figure 1.1: Model behavior regarding Albedo.

1.3.2 Sensitivity analysis for surface temperature

Surface temperature is, according to previous research, one of the most important factors that influence ET estimation with METRIC and SEBAL models. Moreover, Ts is used to estimate NR, G and sensible heat flux (H), which can affect to each component of surface energy balance in different manners and therefore latent energy flux (LE).

In Figure 1.2 it is observed that with an increase of Ts, a decrease of ET_rF and ET_{ins} is generated. This can be explained since NR decrease, due to an increment in the outgoing longwave radiation, and H increase due to an increase in the temperature gradient over the surface. The effect over G is a minimal increase, due to a greater flux to the soil.

If the sensitivity analysis is performed, considering the change of Ts before to estimate dT and Ts relation, the impact over ET_rF and ET_{ins} would be less, because dT estimation would absorb it, as it is shown in Tasumi (2003). In this sense, the analysis presented here addresses possible local error in Ts estimation, generated by possible local conditions of

shadows, atmospheric humidity or anomalies caused by the instrumental equipment (Jacob et al., 2004).

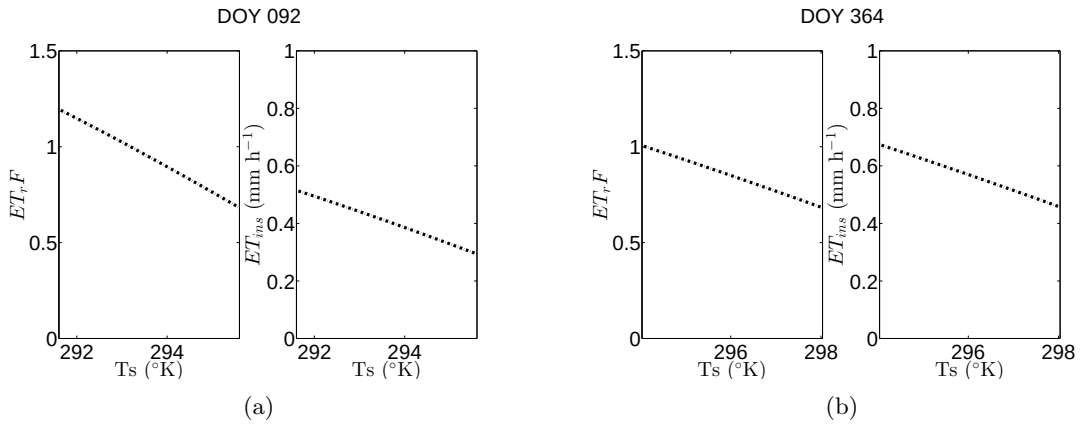

Figure 1.2: Model behavior regarding surface temperature.

1.3.3 Sensitivity analysis for reflectance at the surface

In this research all reflectance bands are evaluated, but only Near Infrared band (NIR) is shown because this band has the most influence over ET estimation. This analysis is very important since it can helps to consider the use of other methods for radiometric and atmospheric corrections. In this instance, these corrections have been done using the manual refereed in Allen et al. (2010).

The model response to an increasing of Refs_{NIR} possess a similar explanation that for albedo, because it generates an increase in the albedo, affecting the NR. The important effect of Refs_{NIR} over the albedo can be explained since this band represents around 30% of the energy captured by the Landsat-7 sensor in shortwave radiation.

1.3.4 Sensitivity analysis for zom_{cp}

As it was explained above, the zom can be analyzed over the anchor pixels or the studied crops. zom_{cp} represents the zom of the cold pixel identified in the image following some of the proposed methodologies to select these anchor pixels. zom_{cp} can vary (erroneously) in an extensive range due that knows the real coverage of cold pixel is not easy, unless that a land cover map be available.

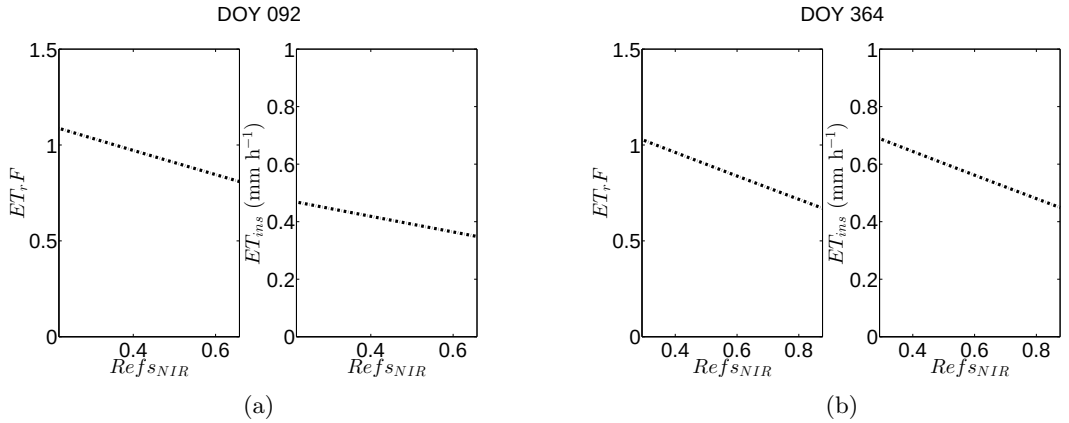

Figure 1.3: Model behavior regarding surface reflectance of near infrared band.

In Figure 1.4, the base condition is in the zom_{cp} equals to 0.07 and 0.06 m for 2012-092 and 2012-364 scenes, respectively. It is observed that the sensitivity has a non lineal response as a result of the estimation of friction velocity using a logarithm function. When zom_{cp} increases, the friction velocity (u^* in Chapter D) also increases, then the resistance of heat transport (r_{ah} in Chapter D) decreases, but, as H for cold pixel is maintained then dT decreases. This effect generates that dT for all pixels in the image decrease, therefore H decreases, and ET_{ins} increases.

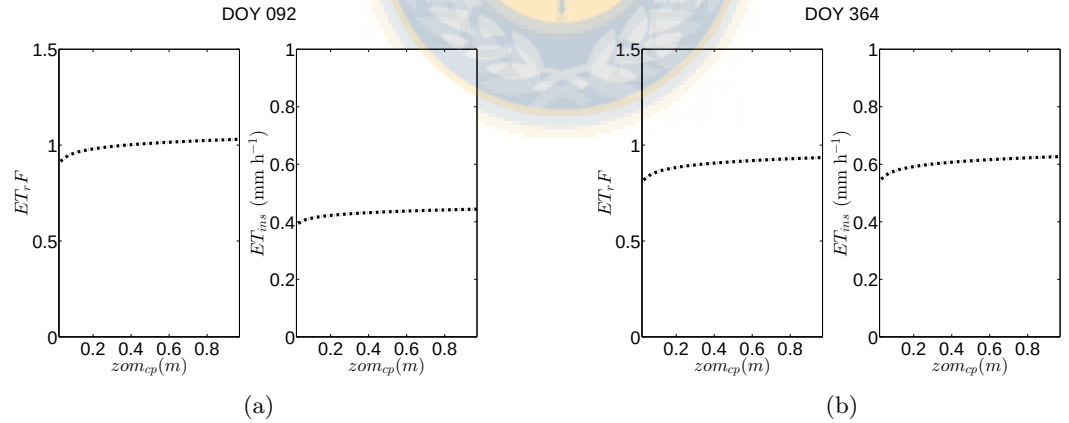

Figure 1.4: Model behavior regarding zom of cold pixel.

1.3.5 Sensitivity analysis for zom_{sp} and zom_{tc}

Despite this parameter is the same as above, the effect generated by varying the zom for cold pixel and analyzed pixel (crop of interest) is very different. In Figure 1.5, different effects of zom_{sp} over ET_rF and ET_{ins} in comparison to zom_{cp} can be observed. In this case an increase in zom_{sp} generates an increase in friction velocity and a decrease in the resistance of heat transport. Then, as dT is maintained, H increases and ET_{ins} decreases.

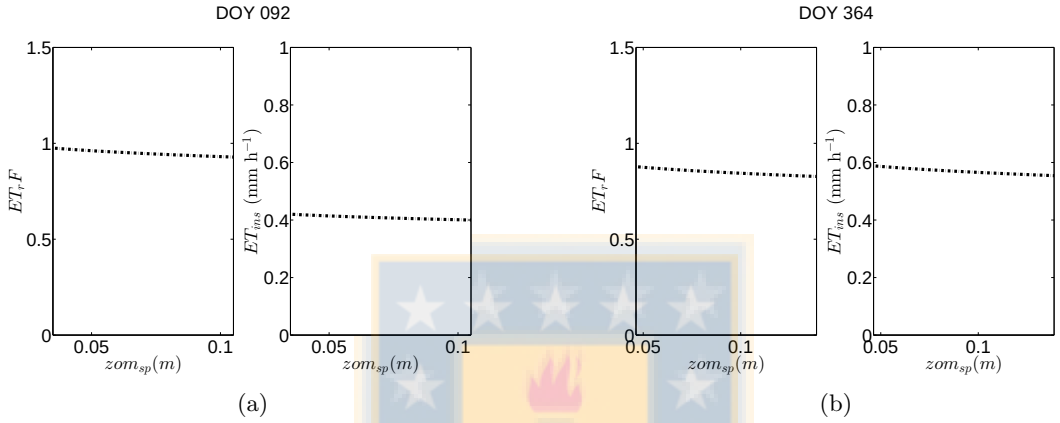

Figure 1.5: Model behavior regarding zom of the crop analyzed.

The behavior of the model regarding to zom_{tc} is the same as the above, the only advantage of this analysis it is able to show the possible impact by greater error in the estimation of zom for a crop different than full coverage crop. The Figure 1.6 presents the same non lineal behavior than Figure 1.4, hidden in Figure 1.5 due to the lesser range of analysis.

The model response regarding zom_{sp} is similar to that shown in Choragudi (2011). However, as in our case the range of analysis was extended (zom_{tc}), the model response shows the real impact if METRIC is erroneously implemented over a tree crop assuming that is a full coverage crop.

1.3.6 Sensitivity analysis for reference evapotranspiration

ETr is an important input of METRIC model as that ETr helps to calibrate the method for sensible heat flux estimation, moreover, using ETr the *fraction of reference evapotranspiration* (ET_rF, Chapter D in the Appendix) is estimated to calculate ET for

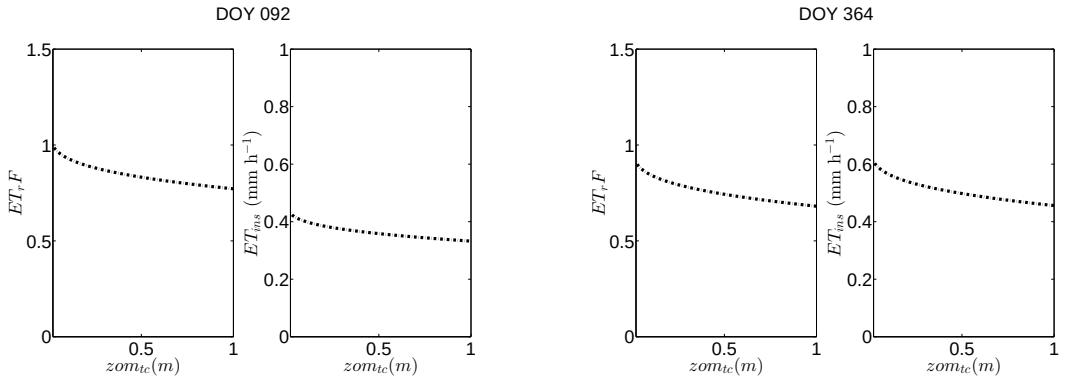

Figure 1.6: Model behavior regarding zom, supposing an error in zom ranging for pasture to tree crop.

a daily scale. Some errors in ETr may be due to instrumentation (installation, sensor problems, errors in reading code, etc.) or calculation.

The results presented in Figure 1.7 show the response of the model regarding ETr. While ETr increases, H and dT for cold pixel decreases, then dT and H for all pixels in the image decreases and therefore ET_{ins} increases.

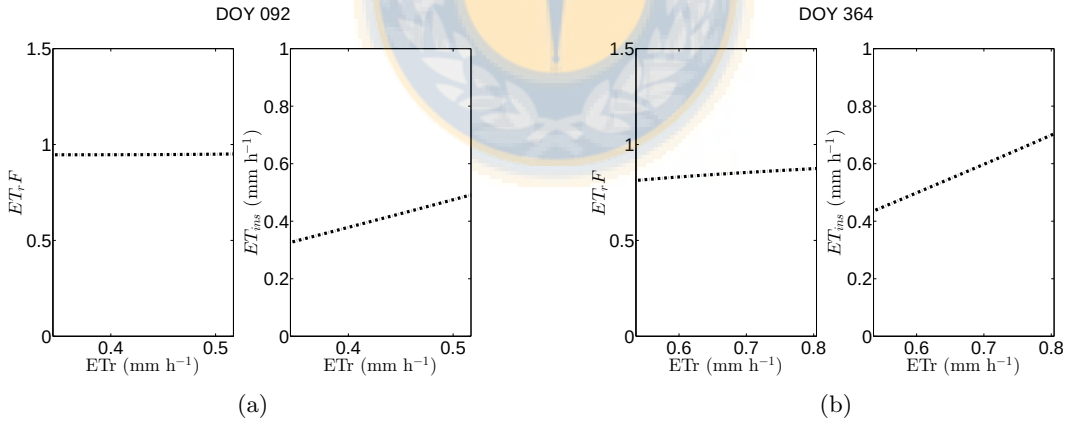

Figure 1.7: Model behavior regarding reference evapotranspiration.

1.3.7 Sensitivity analysis for wind speed

WS is analyzed individually because both, WS and ETr, are used separately in the estimation of sensible heat flux, and some error in WS can be compensated in the estimation of ETr by other input.

In the METRIC model, WS has different ways to make an impact on the ET estimation. First, WS generates an increase in the ETr estimation. Then WS is used in the calibration to obtain the relation between dT and Ts. Finally, WS is used for ET estimation of all pixels in the image. In some research, the sensitivity regarding WS was done considering only the effect of WS on METRIC model, and not over the ETr estimation. In this research the change in WS was incorporated in ETr estimation and METRIC model.

Figure 1.8 shows that an increase in WS generates an increase in ET_{ins}, due mainly to the effect over the ETr estimation. However, the effect of an increase in WS generates a decrease in ET_rF, due to the increase in ETr being greater than the increase of ET_{ins}. This behavior of ET_rF is similar to the results showed in Choragudi (2011).

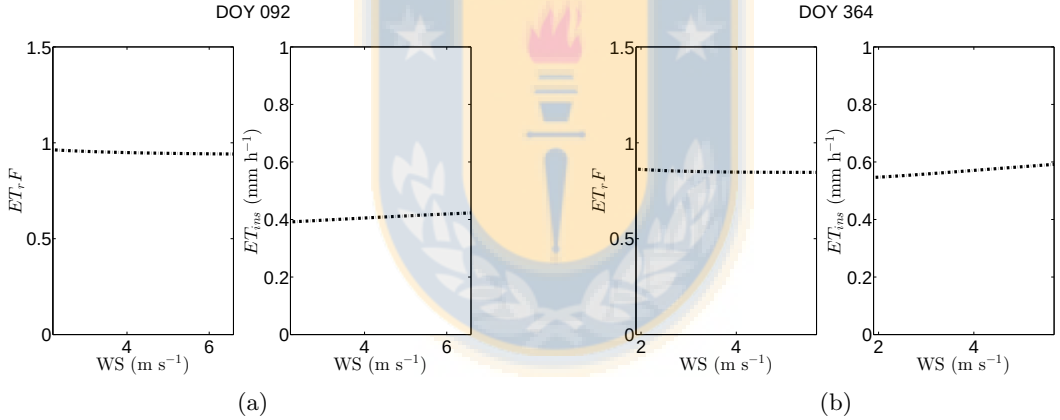

Figure 1.8: Model behavior regarding wind speed.

1.3.8 Sensitivity analysis for near surface vapor pressure

ea is a parameter used in atmospheric correction, net radiation estimation and ETr estimation (out of METRIC model). This parameter can impact in different ways the ET estimation given the different steps where it is used.

The increase of ea induces a decrease in the atmosphere transmissivity that generates

NR decreases. This effect over the atmospheric correction is minimal, with around 10 W*m^{-2} of change in NR ranging from minimum to maximum ea in the 2012-092 scene. The main effect of change in ea affects to ETr estimation, causing that ET$_{ins}$ decreases when ea increases. This decrease in ET$_{ins}$ is mostly canceled in the estimation of ET$_r$F because both, ET$_{ins}$ and ET$_r$F, decrease in similar magnitude.

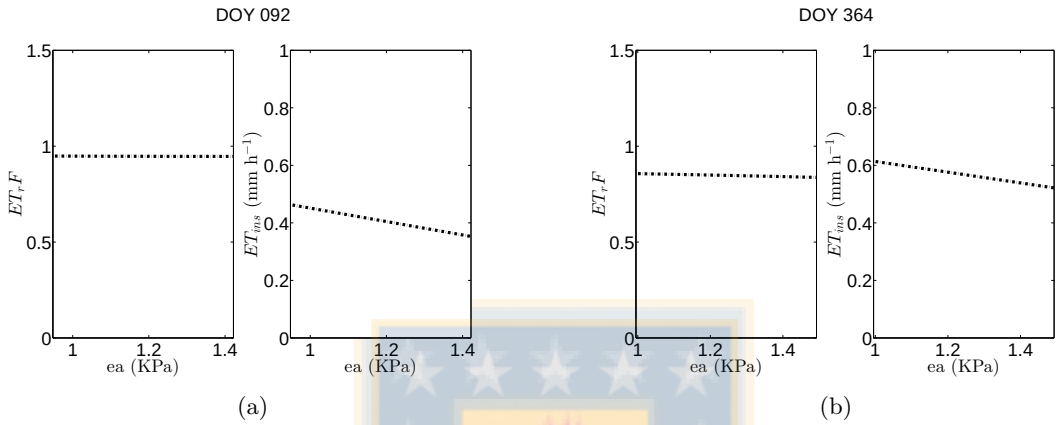

Figure 1.9: Model behavior regarding near surface vapor pressure.

1.3.9 Sensitivity coefficient (S_i)

Table 1.3 shows all sensitivity coefficients calculated for the parameters analyzed. S_i was estimated from ET$_r$F for all parameters, and additionally was estimated from ET$_{ins}$ for parameters that affect ETr estimation in order to shows the effects over instantaneous (ET$_{ins}$) and daily (ET$_r$F) results. Furthermore, in Table 1.3 the maximum % of change in output (ET$_r$F and ET$_{ins}$) are shown (Max$_{\%-change}$), estimated multiplying the *Max* S_i by maximum % of change from Table 1.1.

Considering Max$_{\%-change}$, for two scenes and two output analyzed, Ts and Refs$_{NIR}$ are the most important parameters that make an impact on the model, with % of change in the outputs greater than 24%.

When ET$_{ins}$ is analyzed; Refs$_{NIR}$, Ts and ETr affect more than 20%; ea, albedo and WS between 5 and 18%; while zom$_{sp}$ generates 2.6% of change. It is worth mentioning that the effect of zom$_{cp}$ and zom$_{tc}$ cannot be analyzed using Max$_{\%-change}$ as the responses are not linear and may increase the effect.

On the other hand, when ET_rF is analyzed, the main impacts are from $Refs_{NIR}$, Ts and albedo, with $Max_{\%-change}$ greater than 8%, while ETr do not alter so much ET_rF as the change in ET_{ins} is canceled by the change in the input ETr. All the rest of parameters, including ETr, generate a $Max_{\%-change}$ less than 4%.

In both scenes, the results tends to be similar, only presenting minimal changes in the order of the impact of the parameters in the model.

	S_i							
Parameter	**2012-092**				**2012-364**			
	Min	Max	BC[1]	$Max_{\%-change}$	Min	Max	BC	$Max_{\%-change}$
ETr	1.2394e-04	0.0373	0.0098	0.746	0.1701	0.2040	0.1729	4.08
ETr	0.9991	1.0379	1.0100	20.76	1.1733	1.2091	1.1764	24.18
WS	0.0115	0.0273	-0.0198	1.37	2.0013e-04	0.0344	-0.0156	1.72
WS	0.0416	0.0938	0.0724	4.69	0.0308	0.1121	0.0765	5.61
ea	6.6494e-04	0.0081	-0.0043	0.16	0.0404	0.0785	-0.0580	1.57
ea	0.4787	0.9085	-0.6767	18.17	0.2996	0.5237	-0.4087	10.47
Albedo	0.2439	0.4022	-0.3228	8.04	0.3647	0.6400	-0.4975	12.80
Ts	29.2661	53.2237	-40.2560	36.19	22.6665	34.6442	-28.5263	23.56
$Refs_{NIR}$	0.1293	0.4831	-0.2929	24.16	0.1768	0.7423	-0.4218	37.12
zom_{cp}	0.0170	0.0302	0.0249	*[2]	0.0190	0.0344	0.0281	*
zom_{sp}	0.0369	0.0516	-0.0458	2.58	0.0441	0.0635	-0.0557	3.18
zom_{tc}	0.0280	0.1267	-0.0443	*	0.0307	0.1485	-0.0541	*

Table 1.3: S_i coefficients. Gray rows refers to S_i estimated from ET_{ins}. Min and max values are calculated from $|S_i|$.

1.3.10 Analysis regarding to Anchor pixels

Aforementioned, the sensitive analysis in function of anchor pixels was done changing the pixels that are identified as candidates, unlike in others researches were only their characteristics were varied (Long et al., 2011; Long and Singh, 2013). Moreover, different *regions of interest* (ROIs) where the anchor pixels can be identified, were considered (Figure 1.10). This analysis shows the robustness of the method for anchor pixel selection, regarding the rules of selection and delimitation of the region of interest.

Anchor pixels identified, have been ranked following the criteria presented in Allen et al. (2013), so that the first pixels shown in following figures are the pixels that have a better fulfillment of criteria than the last pixels.

Figures 1.11 and 1.12 show ET_rF values generated by different anchor pixels selected on different ROIs defined. All ROIs fulfill the same requirements: farm areas that include

[1] *BC* refers to S_i in Base Condition.

[2] * means that estimation is not applicable due response is non linear in analyzed range

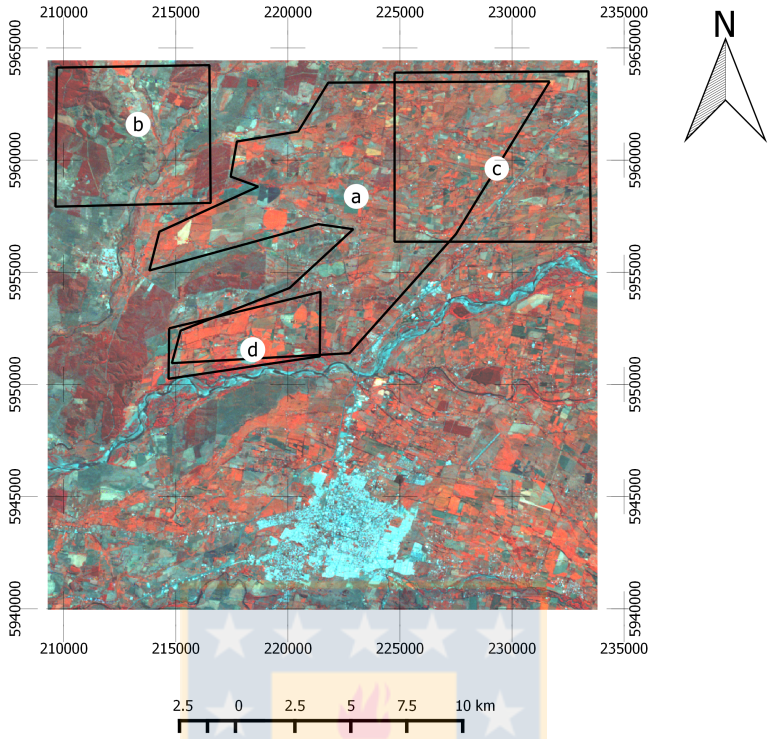

Figure 1.10: Four ROIs where anchor pixels were identified are shown. These ROIs are overlapped to the IGB composition of the scene 2012-092. The coordinates system showed is WGS 84 / UTM zone 19S.

pixels with full crop coverage and agricultural soil; without urban and river classes. However, variations of ET_rF from around 0.6 to 1.1 can be observed, mainly because NDVI and Ts histograms for all ROIs are different, then anchor pixels selected in each ROI have different attributes (NR, Ts, albedo, etc.). In Figure 1.13 different NDVI histograms of the 2012-092 scene for all ROIs are shown, moreover the NDVI threshold values used as the primary criterion to select the anchor pixels are also shown. It can be seen that there are slight differences in the NDVI threshold and histograms.

Figures 1.14 and 1.15 shows the available energy (AE) for the first pair of anchor pixels selected in each ROI for scenes 2012-092 and 2012-364, respectively. For scene 2012-092, AE for hot pixels vary between around 340 and 390 W*m^{-2}, while AE for cold pixels has not a standard range, e.g., for ROI *(a)* vary between around 370 and 380 W*m^{-2} versus in ROI *(b)* vary between around 410 and 430 W*m^{-2}. This indicates that the slight differences in the populations showed in Figure 1.13, although at the definition of these

ROIs are the same, generate differences in the attributes of the anchor pixels selected, and finally different estimated ET. These results also shows the high sensitivity of METRIC respect to AE from cold pixel, more than hot pixel. In this sense, also were analyzed other parameters from anchor pixels, such as NDVI, Ts and albedo, but AE shows the highest correlation with ET_rF.

Considering that the correct ET_rF are 0.95 and 0.85 (calculated from estimated ET by Surface Renewal system and ETr), for 2012-092 and 2012-364 scenes respectively, the best results are generated with the ROI *(a)* in both scenes. Analyzing Figure 1.13, it can be seen that ROI *(a)* has a greater population, with a high variety of crops with different phenological stages and more similar to a normal distribution in comparison with other ROIs. Additionally, it can be observed that selecting a ROI with a heterogeneous presence of different classes of soil and vegetative cover is important, unlike ROIs *(b)* and *(d)*.

Furthermore, Figures 1.11 and 1.12 show that there is not a clear major sensitivity between cold and hot pixels, because depending of the ROI selected, the characteristics of both anchor pixels vary.

1.4 Conclusions

The sensitivity of METRIC model is relatively consistent for different stages of the crop, maintaining similar order and values of impact of the parameters over the outputs. Differences are found in the model sensitivity analyzing different output, as some impacts over ET_{ins} are canceled in the estimation of ET_rF, is the case of ETr and near surface vapor pressure. Most important parameters in the generation of ET_{ins} and ET_rF are Ts and $Refs_{NIR}$ parameters, that generate $Max_{\%-change}$ greater than 24% in both scenes.

About the anchor pixels, it was detected that different ROIs, used to find the anchor pixels, can generate values of ET_rF from around 0.6 to 1.1, which can change the daily ET from 3.6 to 6.6 mm*day^{-1}, considering a hypothetical daily ETr of 6 mm*day^{-1}. One recommendation to avoid this high sensitivity is to define a ROI composed by different phenological stages of vegetative cover in order to avoid specific coverage and pixel distribution not representative.

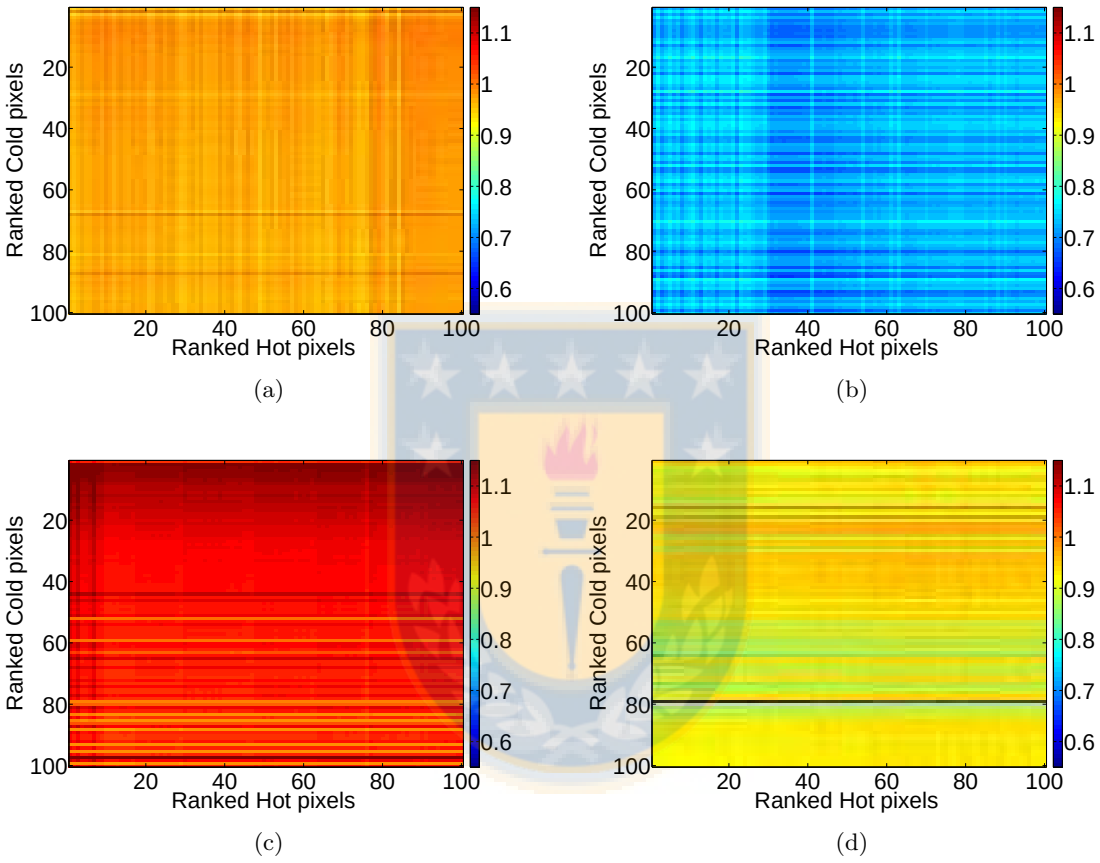

Figure 1.11: Variation in ET_rF generated by different ROIs (*a, b, c* and *d*) for anchor pixels selection in the scene 2012-092. Rows and Columns represent the different cold and hot pixels identified and ranked, respectively.

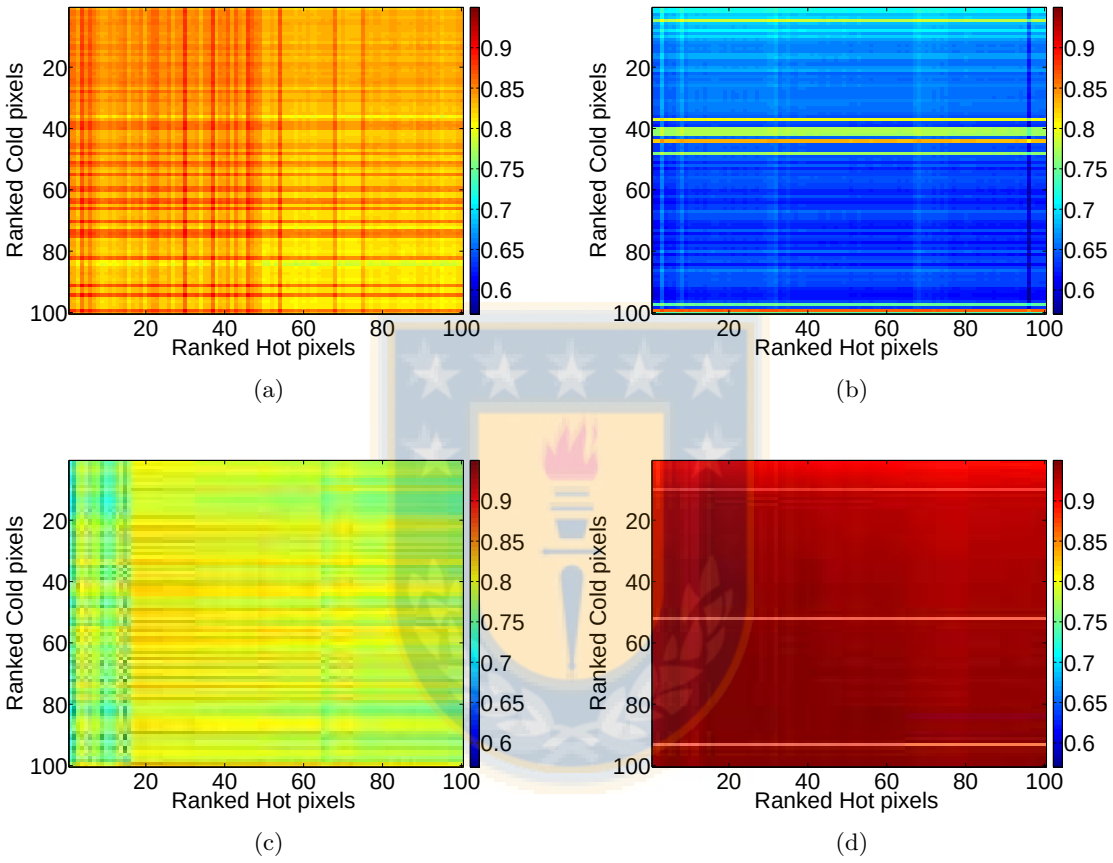

Figure 1.12: Variation in ET_rF generated by different ROIs (*a, b, c* and *d*) for anchor pixels selection in the scene 2012-364. Rows and Columns represent the different cold and hot pixels identified and ranked, respectively.

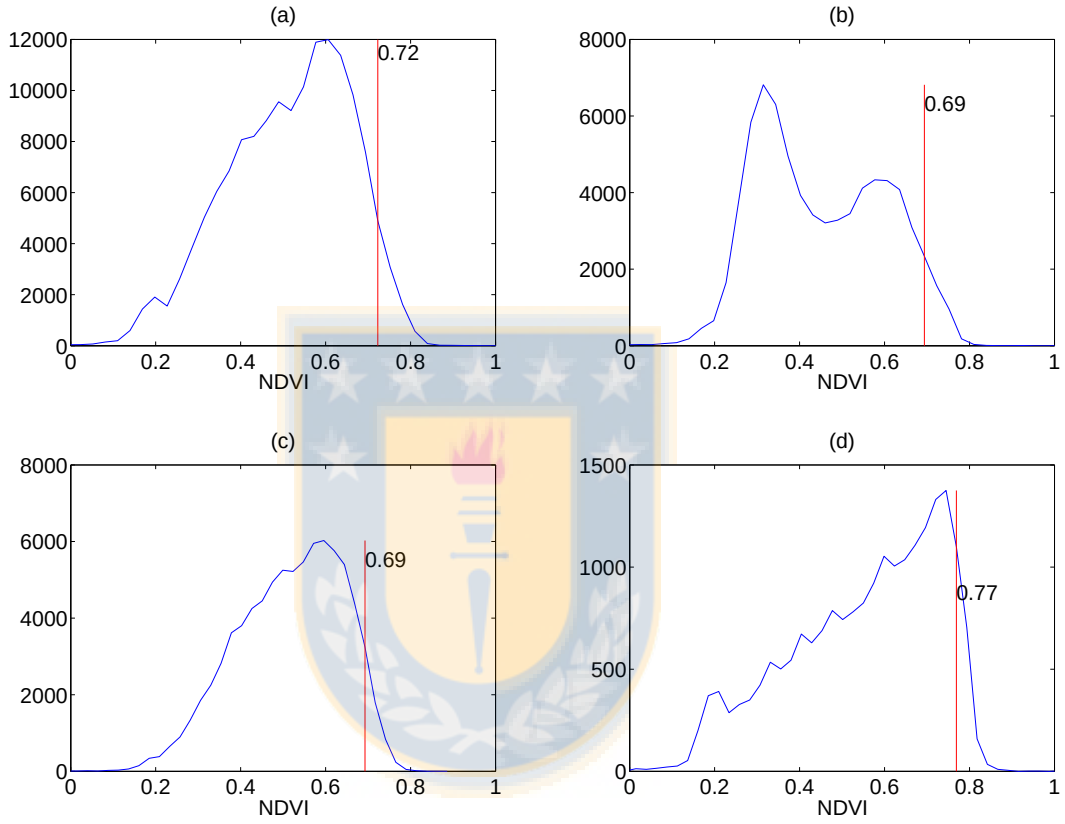

Figure 1.13: NDVI histograms for all ROIs evaluated, including the NDVI threshold value for 5% more high NDVI used as criterion to identify the cold pixel. (a), (b), (c) and (d) histograms corresponds to ROIs with same names showed in Figure 1.10.

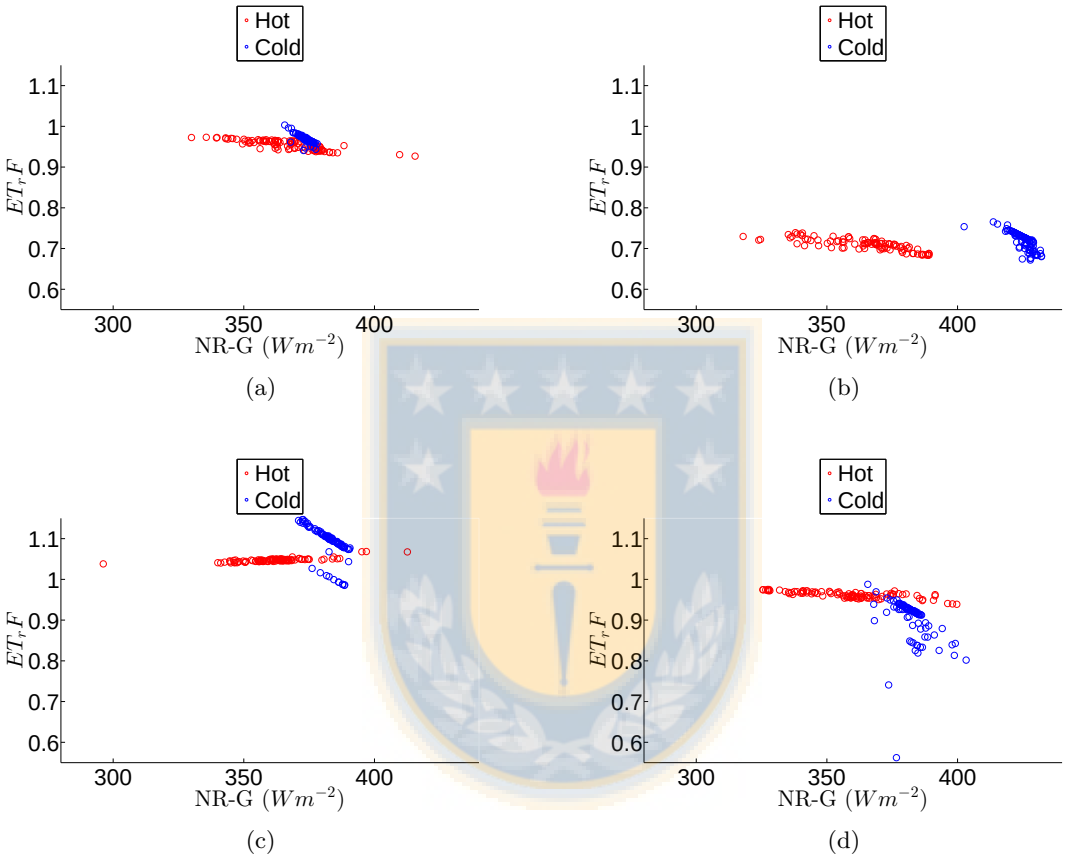

Figure 1.14: Available energy (NR-G, in W*m^{-2}) versus ET$_r$F in the different ROIs, for scene 2012-092. Hot points were generated using all hot pixels and the first ranked cold pixel, while Cold points were generated using all cold pixels and the first ranked hot pixel. (a), (b), (c) and (d) plots corresponds to ROIs with same names showed in Figure 1.10.

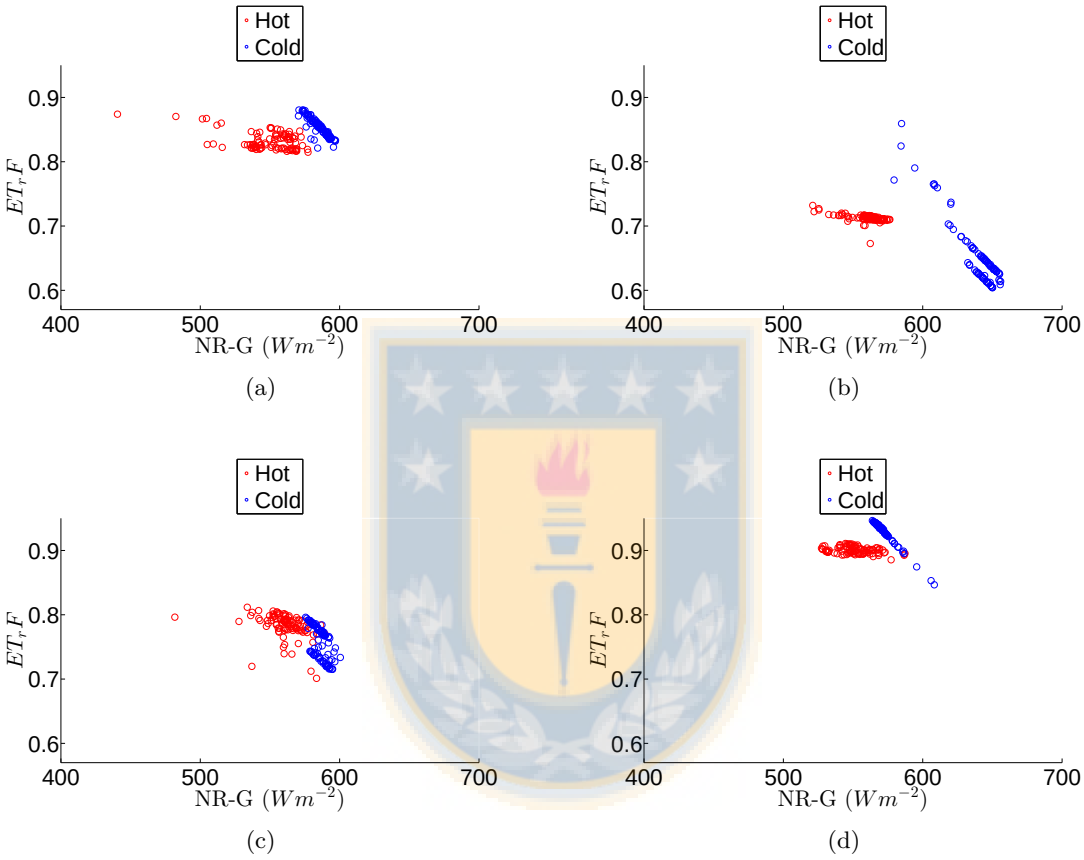

Figure 1.15: Available energy (NR-G, in W*m^{-2}) versus ET$_r$F in the different ROIs, for scene 2012-364. Hot points were generated using all hot pixels and the first ranked cold pixel, while Cold points were generated using all cold pixels and the first ranked hot pixel. (a), (b), (c) and (d) plots corresponds to ROIs with same names showed in Figure 1.10.

Chapter 2

Training process to primary classification

2.1 Introduction

The image classification is one of the main applications in remote sensing, considering visual interpretation or digital analysis Chuvieco (2002). Since the first applications of remote sensing, the image classification has been used in the agricultural area in order to generate knowledge related to the distribution and state of agricultural land cover and to allow the authorities to create effective development plans (Anderson, 1976). In addition, the classification process allows mapping and monitoring of the land cover, identifying changes produced on temporal and spatial scale (Rodriguez-Galiano et al., 2012b).

The availability of satellite images has increased in the last decades with multiple kinds of images related to spatial resolution (low, medium, high and very high), temporal resolution (daily, close to weekly and by programmed capture), spectral range (visible, thermal infrared or hyperspectral), preprocess (digital numbers, geometrically corrected, reflectivity, at surface reflectivity or final products) and price (free or with charge). This major availability allows, among other goals, to improve the image classification in order to mapping land cover changes (Körting et al., 2012; Rodriguez-Galiano et al., 2012b).

Different classification methods have been developed in the past, within these methods we can mention: common algorithms such as K-means, Isodata, minimum distance; and more advanced algorithms such as artificial neural networks, decision trees and support vector machines (Otukei and Blaschke, 2010; Lu and Weng, 2007). However, during the last decades, it has been reported that a combination of individual classifiers, called *ensemble* can generate more accurate results than any individual classifier (Breiman, 1996; Pal, 2005; Kuncheva and Rodríguez, 2014). In Breiman (2001) was proposed a classifier called *random forest* (RF) which is an ensemble of numerous trees that provides a prediction considering the most frequent individual vote by each tree, that in addition the prediction can be a class label (classification) or a numerical value (regression) (Breiman, 2001; Rodriguez-Galiano et al., 2012b). RF generates the classification with each tree using a random subset of input features, this helps to reduce generalization errors. Additionally, it uses different training data subsets created by techniques as bagging (**b**ootstrap **agg**regat**ing**) (Walker et al., 2010; Bauer and Kohavi, 1999; Rodriguez-Galiano et al., 2012a).

In this dissertation, the proposed methodology requires a primary classification process to identify the anchor objects to be used in the METRIC model. Primary classification uses different information from the images to assign a segment to a specific class. These results will be used for anchor objects identification considering contextual information,

among others. The main goal of the present chapter is to train a RF classifier considering different experiments in order to select an optimal methodology implementation.

2.2 Methodology

In this Chapter, a classifier is trained using manually delineated classes over specific Landsat-7 ETM+ scenes. In this sense, an improvement in the classification process is possible considering segments as minimum units instead of pixels, which can be explained because segments can be used to generate more features than from pixels, e.g. textural, geometrical, neighborhood, contextual and hierarchical relations. Furthermore, problems related to high variability of pixels can be solved since segments can be generated considering neighborhood variability, then these segments comprise pixels variability in a set of features (Baatz and Schäpe, 2000; Blaschke, 2010; Peña Barragan et al., 2011; Whiteside et al., 2011; Corcoran et al., 2015).

The proposed methodology consists in a classifiers that learns taking into account different attributes from all segments within the training ROIs. To accomplish this, the segmentation process must be done considering an oversegmentation, so that each ROI will be composed by numerous small segments, then the ensemble will be generated considering all attributes in these segments. These steps are similar to the methodology proposed by Corcoran et al. (2015), which concluded that Random Forest classifier trained using image objects is most accurate than pixel and windowing approaches.

In order to accomplish an accurate classification, different land cover conditions had to be considered. In this sense, following same criteria of Sexton et al. (2013) and Homer et al. (2004), annual season was divided into triplets aiming to consider different climatic and vegetative characteristics, in order to avoid that these different conditions could difficult the training process. In our case, the ground-truth data used in training was generated considering three climatic seasons, in addition two humidity conditions for each season were considered, i.e. wet and dry conditions, based on the previous precipitation for each training scene.

Study site corresponds to *Site 2*, detailed in the Chapter A of this dissertation. Satellite images for training process were captured from year 2011, 2012 and 2013 by the Landsat-7 ETM+ sensor. The images were preprocessed with a gap-filling process detailed in the appendices section, Chapter C. Detail about the images used in the training process is shown in Table 2.1.

DOY-Year	Season	Humidity condition	Previous precipitation	$ETrF_{soil}$ [1]
345-2011	Spring	Dry	-	0
361-2011	Summer	Dry	-	0
092-2012	Autumn	Dry	-	0
316-2012	Spring	Wet	25mm, 2 days before	1
364-2012	Summer	Wet	26mm, 4 days before	0.1
126-2013	Autumn	Wet	42mm, 3 days before	1

Table 2.1: Training scenes and their characteristics in order to consider most of conditions in the season.

2.2.1 Ground-truth data set

A recurrent problem in the classification process is the imbalanced data set used in the training, i.e., one class is underrepresented compared with other classes which can generate problems in the classifier learning (Cieslak and Chawla, 2008), in addition, the classifier could erroneously ignore these underrepresented classes treating them as noise (Galar et al., 2012).

In our case, the training data set was defined in order to generate a uniform distribution between all classes, and then they were equally represented. Table 2.2 shows the area distribution for each class for all training data set (abbreviated names will be detailed in the next paragraph). Considering this, it can be assumed that training data set is balanced, so it is not necessary to use a specific method to work with imbalanced data set (Cieslak and Chawla, 2008; Galar et al., 2012).

Training data set was generated by supervised ROIs delineation, using different false color combination as a reference to identify the different classes. These ROIs were delineated considering small areas to achieve pure information of each class. Classes were defined considering that the main objective was the identification of objects that have similar conditions to anchor pixels, i.e., objects with full vegetation coverage and high vigor (cold pixel), and objects of bare agricultural soil (hot pixel). To accomplish this, initial classes were identified to then separate the classes of interest (cold and hot objects) using contextual rules (in a post classification process). The classes are shown in the Table 2.2: Vegetation with high vigor (VC_{HV}), Vegetation with low vigor (VC_{LV}), Forest and shrub, Urban, Water bodies, Stubble, Mixture between soil and vegetation ($Mixture_{S-V}$),

[1] Fraction of water evaporation from soil in function to reference evapotranspiration. Estimated through a water balance using soil and weather information, following (Allen et al., 1998).

and Bare soil. In the post classification (Chapter 3), the classes of interest for anchor objects were homogeneous VC_{HV} and Bare soil located away from Water bodies (to avoid Bare soil that be part of banks of a river) and Urban (to avoid non agricultural Bare soil and VC_{HV} classes) classes.

Class	**Percentage**
VC_{HV}	16%
VC_{LV}	13%
Forest and shrub	20%
Urban	10%
Water	7%
Stubble	11%
$Mixture_{S-V}$	12%
Bare soil	11%

Table 2.2: Percentage of area for each class in relation to total training data.

Using the same steps as training data set, validation data sets were generated over each scene, but considering to delineate entire covers of the same class to evaluate classification process. An example of two validation data sets is shown in the Figure 2.1 for scenes 2011-361 and 2012-092.

2.2.2 Segmentation

Segmentation process involves the generation of multiples groups of similar pixels in the neighborhood for an entire image. This is an essential first process in GEOBIA approaches since the most important and meaningful information is not represented by single pixels but by objects (or segments) and by their relation (Blaschke, 2003). This process was performed by the *simple linear iterative clustering* (SLIC) algorithm categorized as a *superpixel* method. Superpixel method and SLIC algorithm are described in the Chapter B, for this reason only parameters about the implementation will be presented.

Two inputs to the SLIC algorithm were evaluated. Due the high correlation between ET and NDVI (Normalized Difference Vegetation Index), this index was selected as one input to be evaluated ($SLIC_{ndvi}$). While, on the other hand, a set of bands of Landsat image was selected ($SLIC_{bands}$). These bands correspond to the surface reflectivity for blue, green, red, near infrared, shortwave infrared-1, shortwave infrared-2 bands and surface temperature in Kelvin degrees.

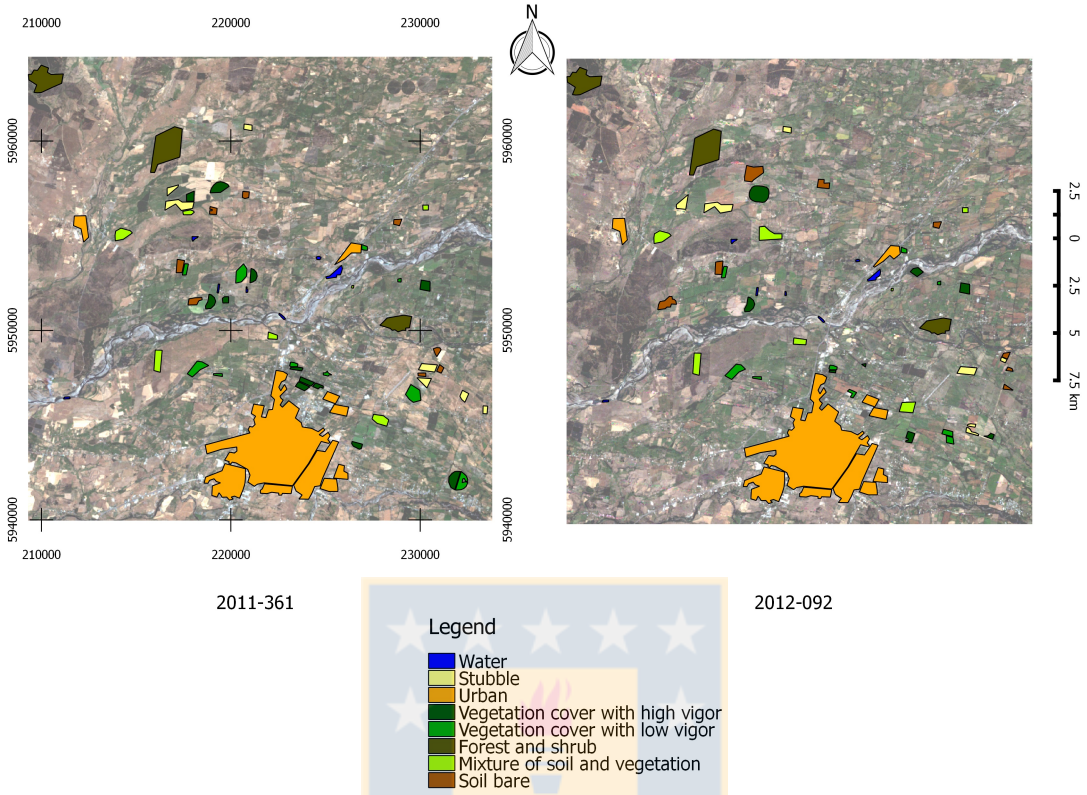

Figure 2.1: Validation data set overlapped to RGB composition (red-green-blue bands) of the scenes 2011-361 and 2012-092. Coordinates system showed is WGS 84 / UTM zone 19S.

Evaluation of both inputs used in SLIC is done considering results of the classification through of out-of-bag (OOB) error estimated by RF. OOB will be explained in the following section.

In this initial segmentation, in order to train the classifier, a fine scale for the SLIC was selected. Segmentation at fine scale means that objects are smaller and purer than a coarser scale, allowing that the classifier can extract more segments from the training ROIs, increasing the samples for the training data set. A fine scale of around 9 pixels was selected for the segmentation process, this means that each segment has an area close to 1 ha, being a sufficient extension for small farmland representation.

2.2.3 Classifier

As was mentioned above, ensembles have been very popular in the last decades since generate more accurate results that an individual classifier. One of these ensemble methods is the bagging. It which is a combination of individual tree classifiers, each one of them trained through of replicas randomly selected of the original training data set. These replicas are close to 37% of the total original data set and are selected using the algorithm called bootstrap aggregation, introduced by Breiman (1996). This process leave out about 37% of the samples ($1/\boldsymbol{e}$) allowing to use them later to estimate a classification error called out-of-bag (OOB). This OOB error is useful when a classifier evaluation has to be carried out without a validation data set (Chan and Paelinckx, 2008).

This algorithm has the advantage of reducing the variance component of the output error. In Breiman (2001), a new ensemble classifier called Random Forest was proposed, which is similar to bagging except that each tree grows using a random subset of predictors or features. This procedure keeps a low bias and generates a robust classifier considering the noise in training data set (Breiman, 2001; Prasad et al., 2006).

RF was selected in this dissertation due training data are extracted from segments that belonging to manually delineated polygons, these can have noisy data or erroneously training classes.

Random forest algorithm extracts information from a set of ground-truth ROIs, considering all segments that are completely and partially inside them. Some details about characteristics and conditions about these scenes used as training data set are shown in Table 2.1. Each scene generates a model for the specific conditions (annual season and humidity).

To implement these classifiers to new scenes, both season and humidity conditions are considered, i.e., all new scenes that are captured in *spring* are classified using 316-2012 or 364-2012, selecting one of them depending if the new scene has a wet or dry humidity condition. In order to estimate the humidity condition of the new scene, a water balance model is carried out in the scene using soil information and data from a weather station (Allen et al., 1998). Then, the fraction of evaporation from soil in function of reference evapotranspiration ($ETrF_{soil}$) is calculated. A threshold value is considered to separate a wet from a dry condition, i.e. with a $ETrF_{soil}$ less than 0.05 the scene is considered in dry condition, while with $ETrF_{soil}$ greater than 0.05 the scene is considered in wet condition.

Information used in RF is composed by different maps generated from the original

Landsat bands, which are useful for separating classes. These maps are: surface reflectivity for blue, green, red, near infrared (NIR), shortwave infrared-1 (SIR1) and shortwave infrared-2 (SIR2) bands; surface temperature in Kelvin degrees, surface albedo, NDVI, Soil-adjusted vegetation index (SAVI), 3 components of Tasseled Cap transformation (Brightness, Greenness and Wetness) (Huang et al., 2002), Water index (Xu, 2006) and Entropy (Gonzalez et al., 2004). In an image, this index is calculated in the neighborhood of a specific pixel, generating a textural map for all pixels. In this step, a neighborhood of 31x31 pixels was used for entropy estimation.

Due to the different ranges for each map, these were scaled to a specific range for each map. The metrics extracted from the segments are mean, median, standard deviation and mode, for all maps described above.

Training process was done using segments at the finest scale in each ROIs, i.e., considering an oversegmented image. However, the implementation of the classifiers on new scenes considers segments at optimal scale. This can be explained since the segmentation at optimal scale provides a more comprehensive segments, generated considering the intra-variability and inter-heterogeneity in the analysis of parents-children relation (Chapter B). This hierarchical approach to image segmentation allows generating less or equal number of segments than fine scale segmentation, used in training, with a meaningful consistency between homogeneity and neighborhood separability. In this hierarchical analysis, number of segments associated with each scale were generated using a dyadic succession from 1 to 50 ha, getting 7 scales with number of segments ranging from 65536 to 1024 for finest and coarsest scale, respectively (Figure 2.2). Information in detail about optimal scale segmentation can be observed in the Chapter B.

2.3 Results and discussion

As it was mentioned in the section 2.2, two inputs for the SLIC algorithm were evaluated. Figures 2.3 and 2.4 shows the OOB errors for the SLIC_{ndvi} and SLIC_{bands} inputs in all scenes. These results showed that the OOB errors are similar in both cases. Moreover, the error stabilization is accomplished around 300 trees in all scenes and inputs. Because this similarity the following results will be generated using SLIC_{ndvi} as an input in the segmentation process, this input also allows to decrease the time execution of the implementation.

Figures 2.5, 2.6 and 2.7 show the importance of all features used in the classification

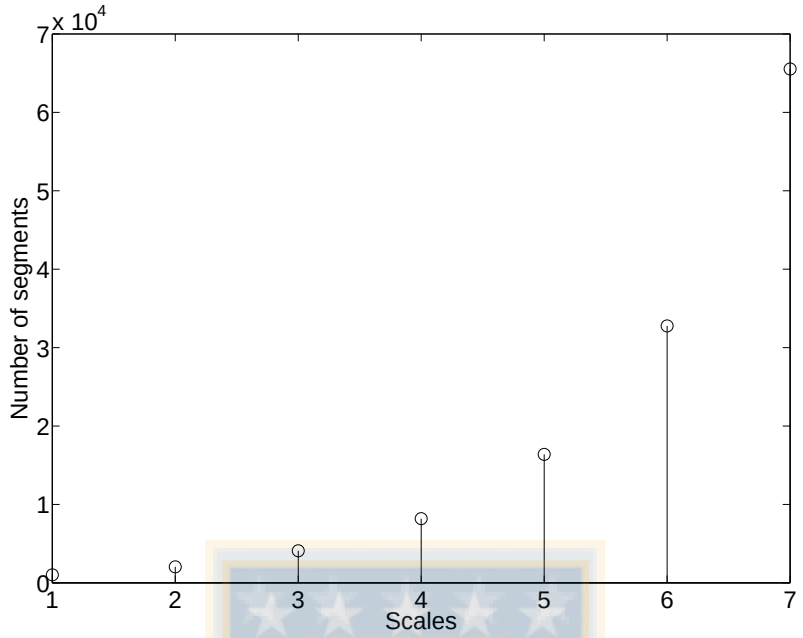

Figure 2.2: Scales and number of segments generated to perform the segmentation at optimal scale.

process, estimated using OOB data generated by RF from training data set. In all scenes, the main features were blue, near infrared, surface temperature, NDVI, Water index, greenness, and entropy bands, using the *mean* metric. Almost of other metrics had low importance, specially the standard deviation.

Figures 2.8, 2.9 and 2.10 shows the classification maps generated using the trained RF's. The urban class is clearly detected, not only in the main city but also in small villages. This result is due to the Entropy descriptor that has high values in zones with high variability, generated by the combination of buildings, street and small vegetated areas (Shackelford and Davis, 2003). The river is also detected, even a small river close to the main city. Some bodies of water were correctly detected, like small irrigation reservoirs. However, some bodies of water were erroneously identified in some forested areas. These two classes, Urban and Water, are very important for validation due that anchor objects should not be neighbors to these classes.

Confusion matrix was uses to evaluate and visualize the performance of classification process. Confusion matrix for all training scenes are shown in Tables 2.3, 2.4, 2.5, 2.6,

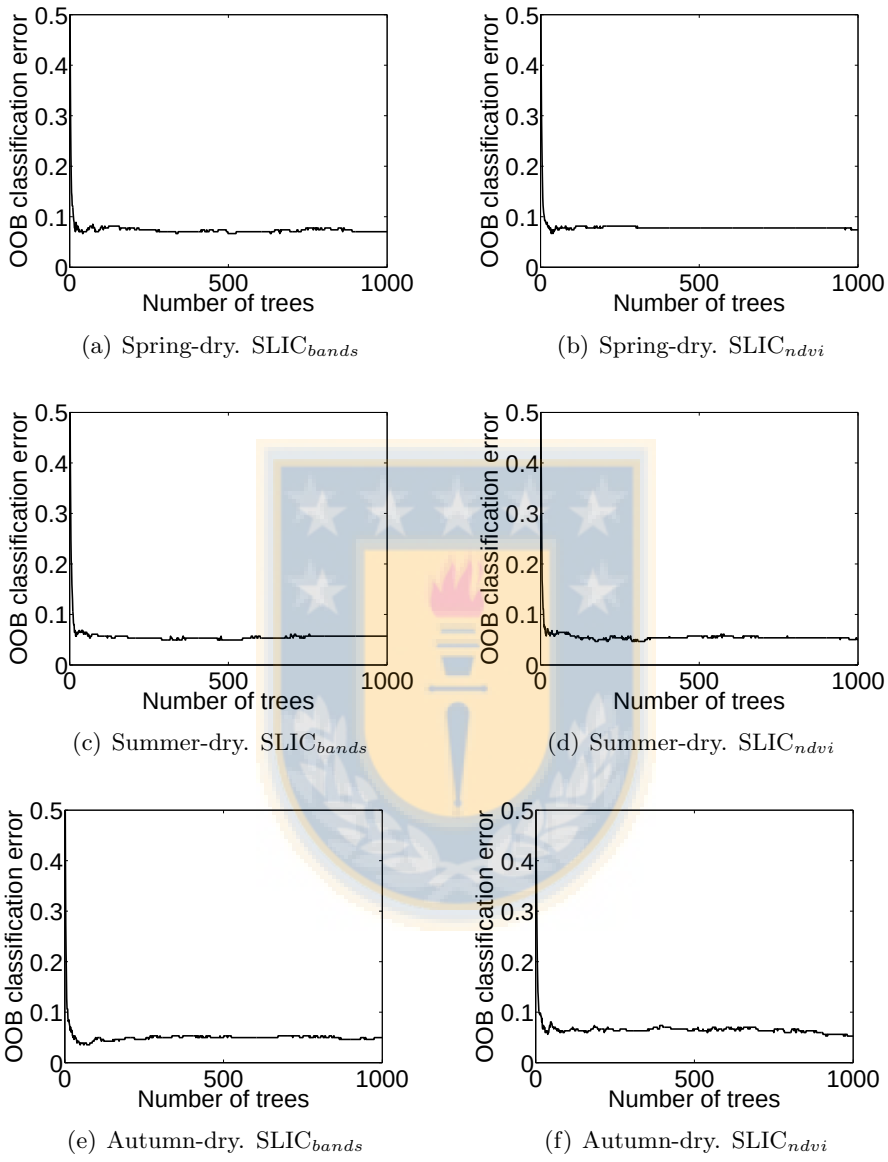

(a) Spring-dry. SLIC$_{bands}$

(b) Spring-dry. SLIC$_{ndvi}$

(c) Summer-dry. SLIC$_{bands}$

(d) Summer-dry. SLIC$_{ndvi}$

(e) Autumn-dry. SLIC$_{bands}$

(f) Autumn-dry. SLIC$_{ndvi}$

Figure 2.3: OOB error for two inputs evaluated in the SLIC algorithm for the three seasons and dry conditions.

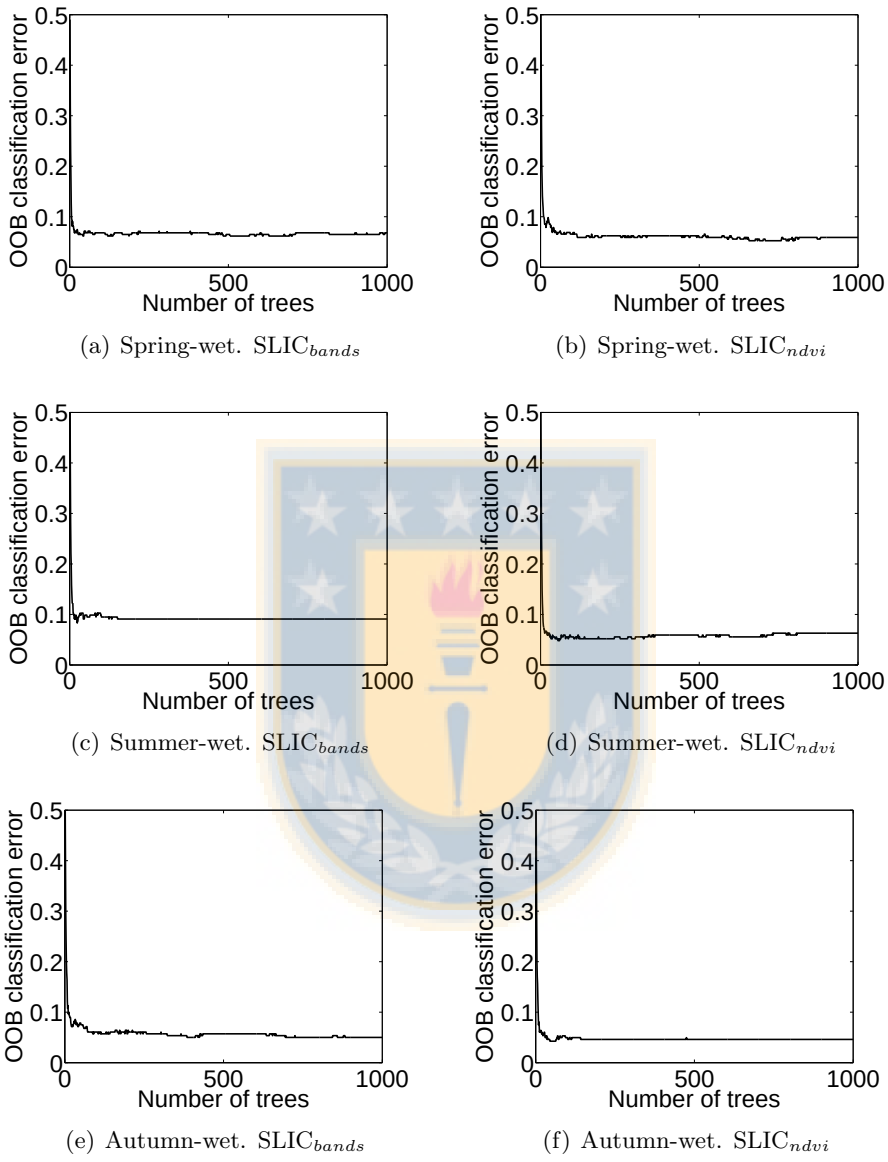

(a) Spring-wet. SLIC$_{bands}$ (b) Spring-wet. SLIC$_{ndvi}$

(c) Summer-wet. SLIC$_{bands}$ (d) Summer-wet. SLIC$_{ndvi}$

(e) Autumn-wet. SLIC$_{bands}$ (f) Autumn-wet. SLIC$_{ndvi}$

Figure 2.4: OOB error for two inputs evaluated in the SLIC algorithm for the three seasons and wet conditions.

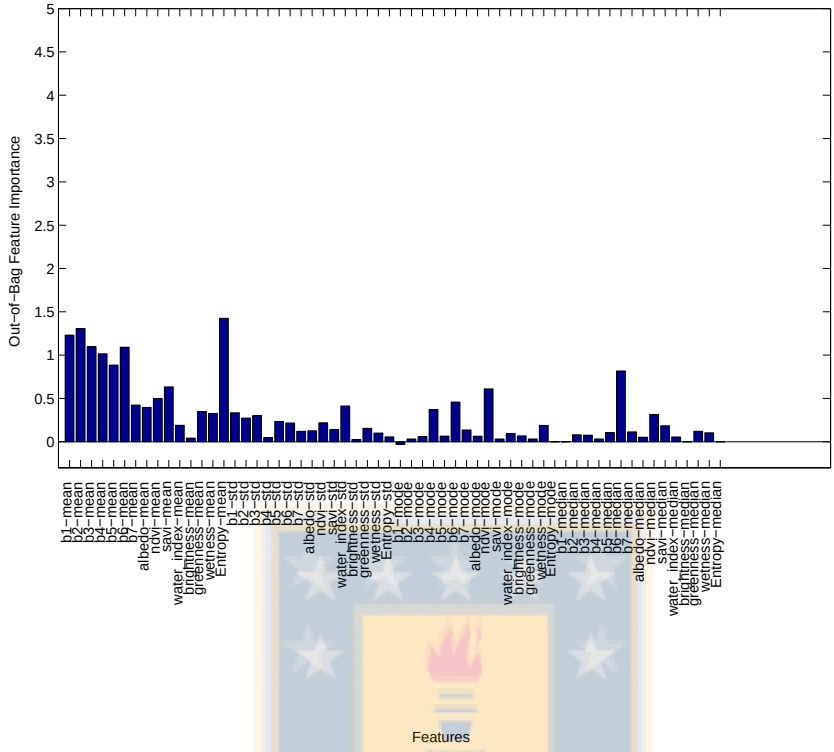

(a) OOB for Spring-dry

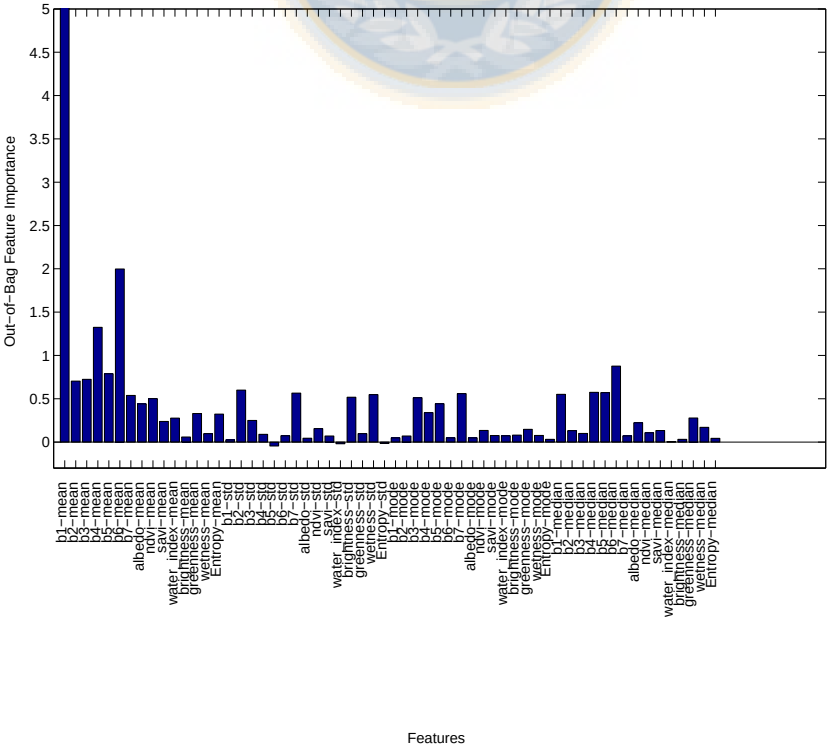

(b) OOB for Spring-wet

Figure 2.5: OOB Feature importance for Spring scenes.

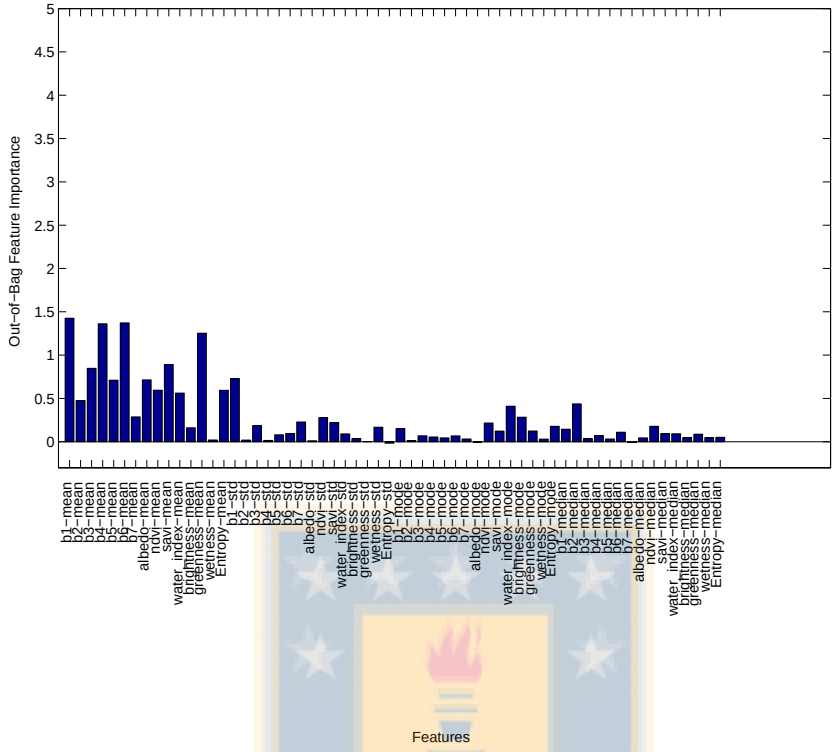

(a) OOB for Summer-dry

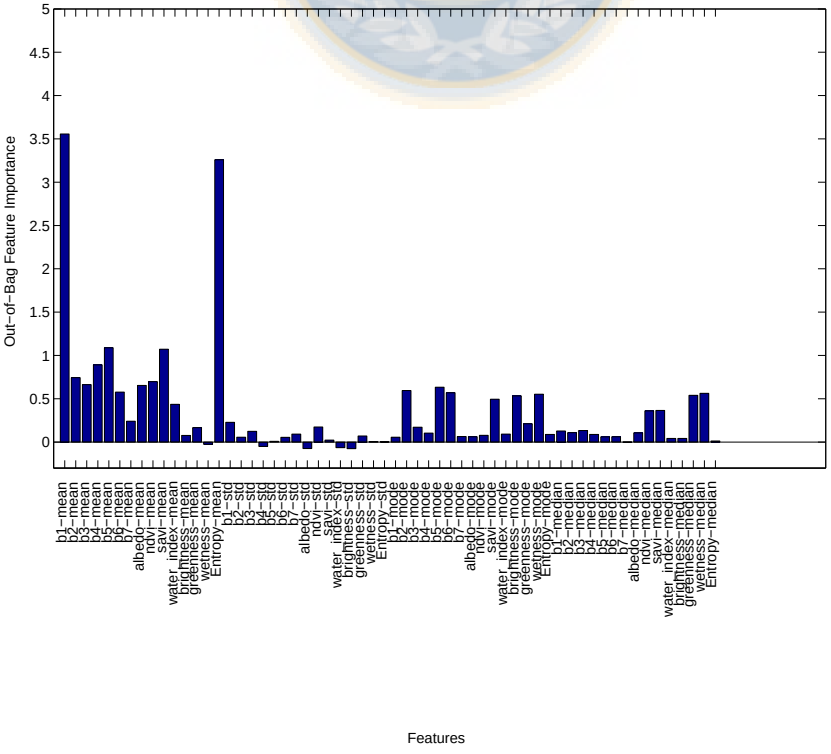

(b) OOB for Summer-wet

Figure 2.6: OOB Feature importance for Summer scenes.

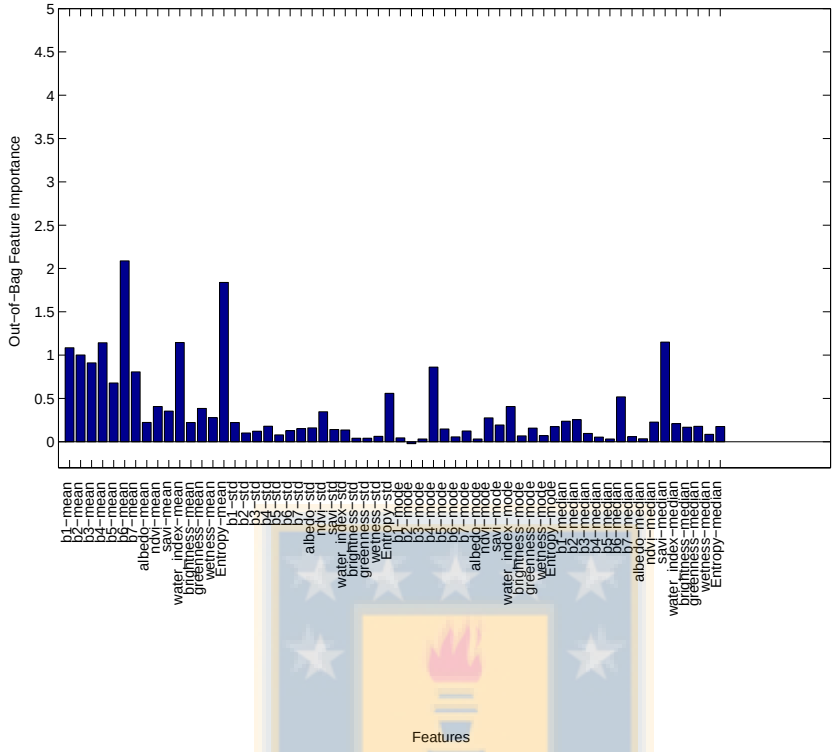

(a) OOB for Autumn-dry

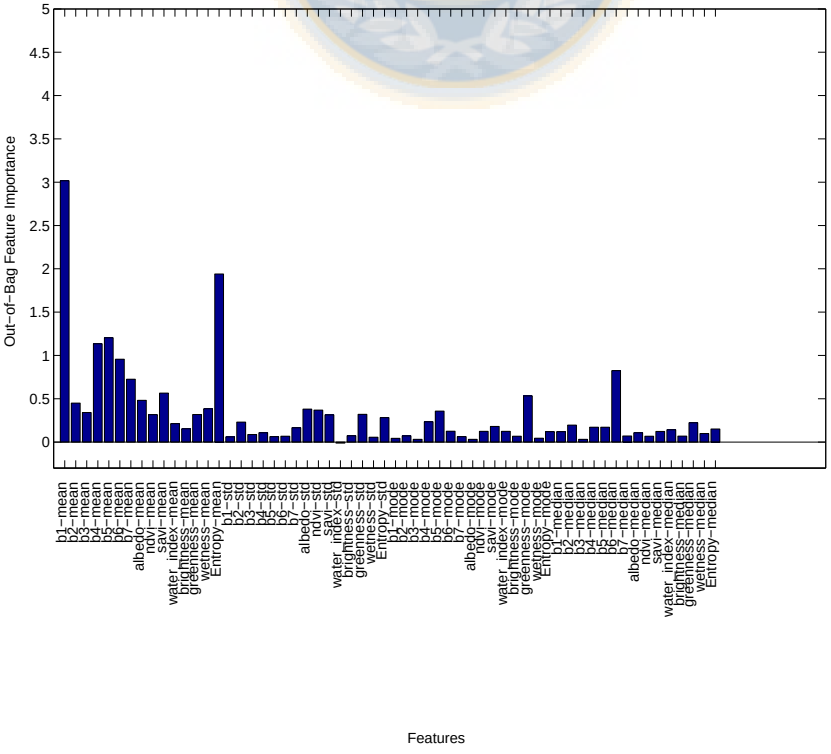

(b) OOB for Autumn-wet

Figure 2.7: OOB Feature importance for Autumn scenes.

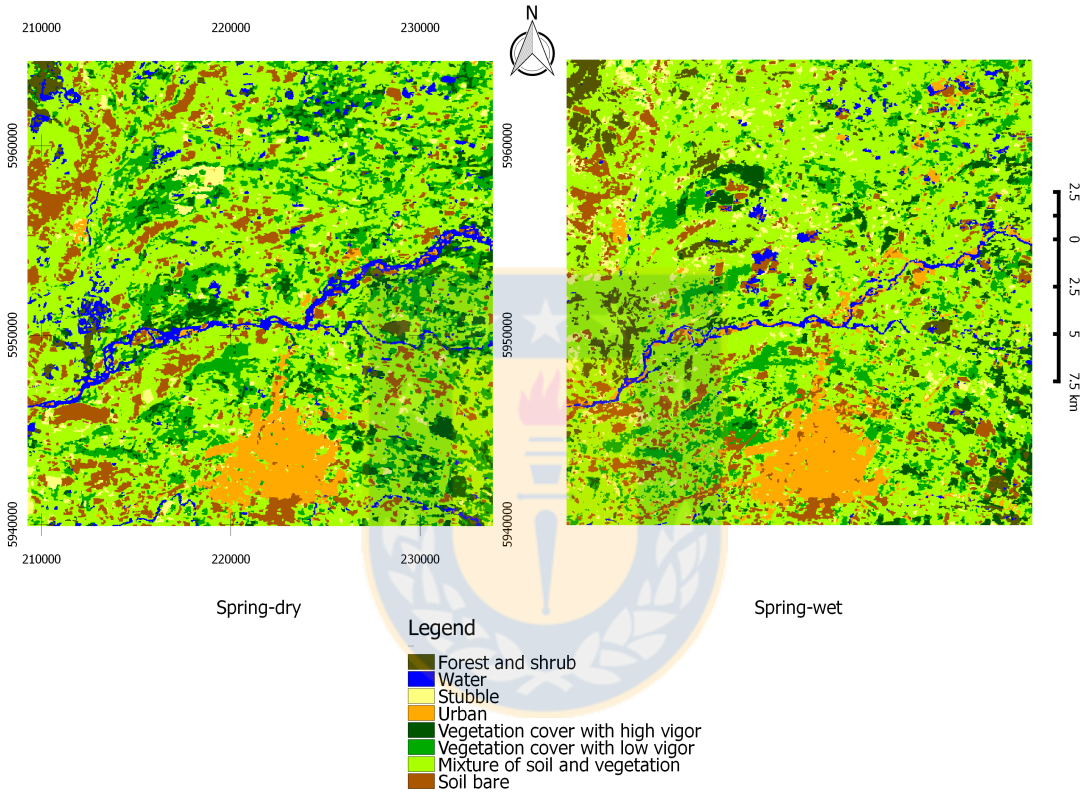

Figure 2.8: Classification maps for training scenes for Spring season.

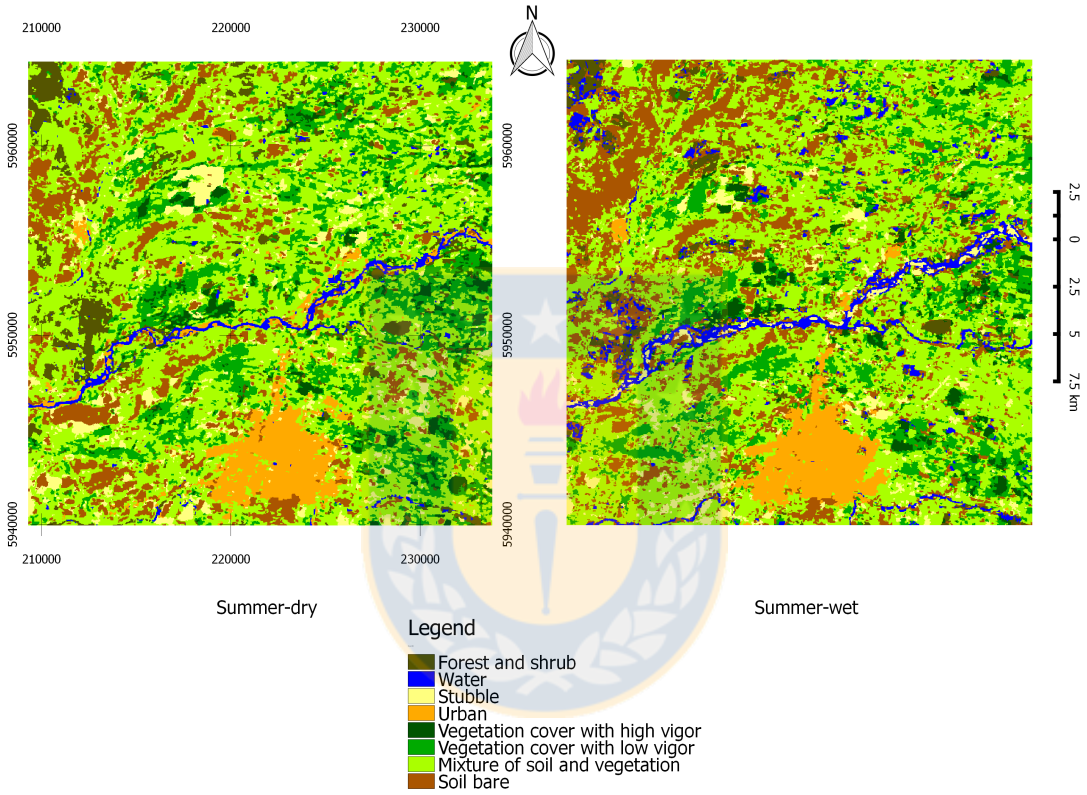

Figure 2.9: Classification maps for training scenes for Summer season.

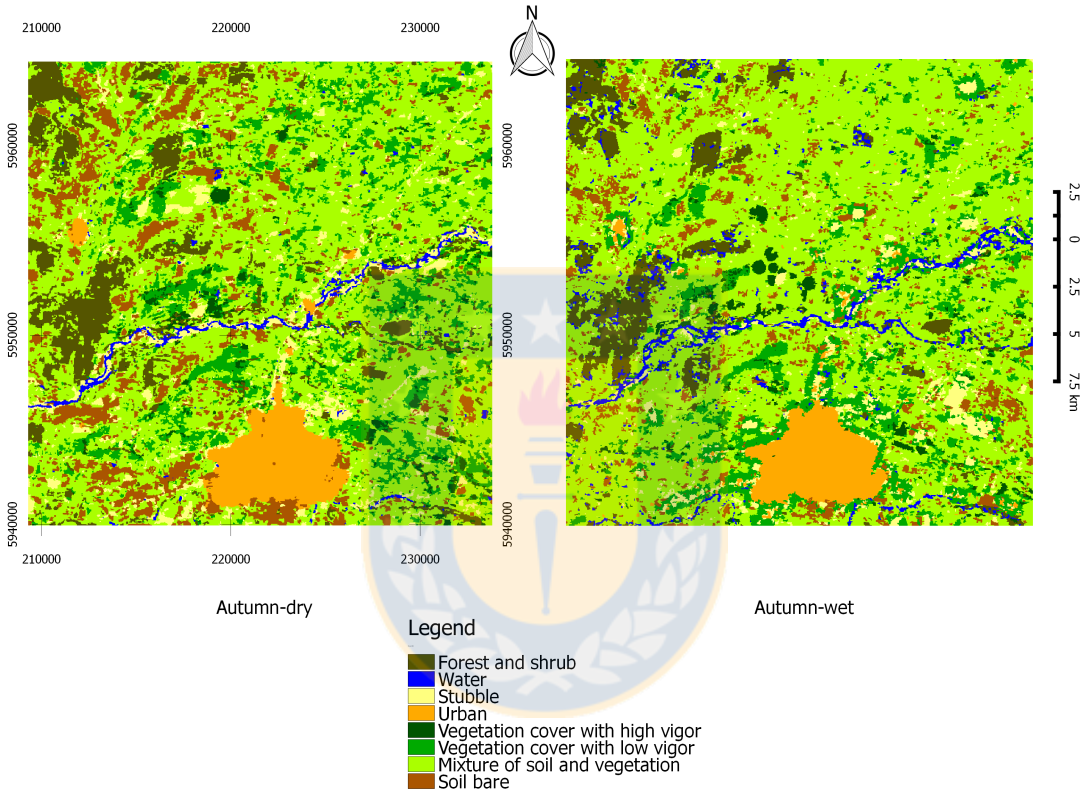

Figure 2.10: Classification maps for training scenes for Autumn season.

2.7 and 2.6. It can be observed that ensembles tend to misclassify between Forest and shrub, VC_{HV} and VC_{LV}; and between Bare soil with Urban and $Mixture_{S-V}$. In addition, $Mixture_{S-V}$ is misclassified by all rest of classes. Also is observed that VC_{HV} is detected in some covers of Water class because similar low temperatures are found in both classes. In addition, this misclassification can be explained since all validation ROIs for water class are very small, then these small ROIs of water can be integrated in VC_{HV} class that are located around a river or reservoirs. About the classes that will be candidates to anchor objects in the post classification process, VC_{HV} have main errors when is erroneously classified by VC_{LV}, but using simple conditions this error can be solved in a post classification process (e.g., considering temperature). Bare soil have a good accuracy, having small misclassification with Urban and $Mixture_{S-V}$ classes. Even though all Urban ROIs were not detected, the advantage is that this class was not misclassified with other classes.

Through the comparison of generated classes with validation ROIs delineated manually by a user, overall accuracies for all scenes ranged between 83% and 90%.

Table 2.3: Confusion matrix for scene 2011-345

	Forest and shrub	Water	Stubble	Urban	VC_{HV}	VC_{LV}	$Mixture_{S-V}$	Bare soil	%
Forest and shrub	**94,72**	0,00	0,00	0,00	4,80	0,47	0,00	0,00	100,00
Water	0,03	**89,17**	0,18	2,62	1,15	5,37	1,49	0,00	100,00
Stubble	0,00	0,00	**77,41**	0,00	0,90	1,51	0,00	20,18	100,00
Urban	0,00	0,00	0,00	**86,91**	0,00	13,09	0,00	0,00	100,00
VC_{HV}	21,00	0,00	0,59	0,00	**68,53**	9,87	0,00	0,00	100,00
VC_{LV}	0,00	0,00	0,00	2,03	5,08	**92,55**	0,34	0,00	100,00
$Mixture_{S-V}$	0,00	0,00	0,10	1,91	29,73	6,21	**62,05**	0,00	100,00
Bare soil	8,44	0,00	14,66	0,00	2,93	26,85	0,00	**47,13**	100,00
%	124,19	89,17	92,93	93,47	113,13	155,92	63,87	67,31	**82,78**

Table 2.4: Confusion matrix for scene 2011-361

	Forest and shrub	Water	Stubble	Urban	VC_{HV}	VC_{LV}	$Mixture_{S-V}$	Bare soil	%
Forest and shrub	**89,89**	0,00	0,00	0,00	8,98	0,75	0,19	0,19	100,00
Water	0,00	**91,08**	0,18	2,28	0,06	4,70	1,68	0,02	100,00
Stubble	0,00	0,21	**76,07**	0,00	0,21	6,20	0,43	16,88	100,00
Urban	0,00	1,83	0,00	**81,75**	0,00	10,17	6,25	0,00	100,00
VC_{HV}	13,85	0,00	0,00	0,00	**62,81**	22,33	0,22	0,79	100,00
VC_{LV}	0,00	0,00	0,00	0,12	1,09	**98,36**	0,43	0,00	100,00
$Mixture_{S-V}$	0,00	0,00	0,00	0,17	3,86	4,15	**91,82**	0,00	100,00
Bare soil	0,00	0,00	0,15	0,06	2,41	35,56	0,00	**61,83**	100,00
%	103,74	93,12	76,40	84,38	79,44	182,20	101,02	79,71	**85,69**

Table 2.5: Confusion matrix for scene 2012-092

	Forest and shrub	Water	Stubble	Urban	VC_{HV}	VC_{LV}	$Mixture_{S-V}$	Bare soil	%
Forest and shrub	**64,04**	0,00	0,00	0,00	8,38	16,55	0,26	10,78	100,00
Water	0,00	**92,18**	0,27	0,70	0,03	1,10	5,71	0,00	100,00
Stubble	0,00	0,00	**67,01**	0,00	0,77	4,35	17,14	10,74	100,00
Urban	0,00	0,00	8,12	**73,48**	0,00	16,29	1,00	1,10	100,00
VC_{HV}	0,08	0,00	0,00	0,00	**77,79**	21,39	0,74	0,00	100,00
VC_{LV}	0,00	0,00	0,00	4,22	0,58	**88,72**	0,00	6,48	100,00
$Mixture_{S-V}$	0,00	0,00	0,00	0,97	0,06	24,64	**74,34**	0,00	100,00
Bare soil	0,07	0,00	0,00	0,02	0,00	6,55	0,00	**93,36**	100,00
%	64,20	92,18	75,40	79,39	87,60	179,59	99,17	122,47	**88,63**

Table 2.6: Confusion matrix for scene 2012-316

	Forest and shrub	Water	Stubble	Urban	VC_{HV}	VC_{LV}	$Mixture_{S-V}$	Bare soil	%
Forest and shrub	**83,44**	0,00	0,00	0,00	5,49	11,07	0,00	0,00	100,00
Water	0,00	**91,54**	0,00	4,49	0,21	2,91	0,85	0,00	100,00
Stubble	0,00	0,00	**79,35**	0,00	0,00	16,30	0,00	4,35	100,00
Urban	0,00	0,00	3,19	**82,20**	0,00	14,60	0,00	0,00	100,00
VC_{HV}	2,39	0,00	0,00	0,00	**82,91**	14,45	0,08	0,16	100,00
VC_{LV}	0,00	0,12	0,00	1,15	11,63	**81,25**	5,85	0,00	100,00
$Mixture_{S-V}$	0,00	0,00	0,00	0,00	0,16	25,83	**74,02**	0,00	100,00
Bare soil	1,06	0,11	3,14	0,00	0,00	8,17	0,00	**87,52**	100,00
%	86,88	91,78	85,68	87,83	100,41	174,59	80,80	92,03	**89,02**

Table 2.7: Confusion matrix for scene 2012-364

	Forest and shrub	Water	Stubble	Urban	VC_{HV}	VC_{LV}	$Mixture_{S-V}$	Bare soil	%
Forest and shrub	**83,16**	0,00	0,20	0,00	11,68	4,35	0,00	0,61	100,00
Water	0,00	**93,25**	0,04	1,00	0,15	2,54	3,00	0,01	100,00
Stubble	0,00	0,00	**83,33**	5,41	0,00	7,66	0,00	3,60	100,00
Urban	0,45	0,00	0,09	**69,75**	1,18	15,49	13,04	0,00	100,00
VC_{HV}	0,00	0,00	0,00	0,40	**86,15**	13,45	0,00	0,00	100,00
VC_{LV}	0,00	0,00	0,00	2,79	2,63	**94,58**	0,00	0,00	100,00
$Mixture_{S-V}$	0,00	0,00	0,00	0,71	0,47	22,13	**76,69**	0,00	100,00
Bare soil	0,56	0,00	9,62	3,91	0,06	2,37	0,00	**83,49**	100,00
%	84,18	93,25	93,28	83,95	102,32	162,56	92,74	87,71	**90,10**

Table 2.8: Confusion matrix for scene 2013-126

	Forest and shrub	Water	Stubble	Urban	VC_{HV}	VC_{LV}	$Mixture_{S-V}$	Bare soil	%
Forest and shrub	**71,07**	0,00	0,14	0,00	23,77	4,75	0,00	0,27	100,00
Water	0,00	**90,36**	0,07	0,06	3,34	0,19	5,98	0,00	100,00
Stubble	0,00	0,00	**67,82**	0,00	0,00	7,92	0,00	24,26	100,00
Urban	0,00	0,00	0,30	**71,39**	0,20	28,11	0,00	0,00	100,00
VC_{HV}	1,39	0,00	0,00	0,00	**90,10**	8,51	0,00	0,00	100,00
VC_{LV}	0,00	0,00	6,75	3,09	1,60	**69,11**	2,97	16,48	100,00
$Mixture_{S-V}$	0,00	0,00	0,00	0,00	4,94	1,90	**93,16**	0,00	100,00
Bare soil	0,22	0,00	3,15	0,06	0,00	3,77	0,00	**92,81**	100,00
%	72,68	90,36	78,23	74,59	123,94	124,27	102,11	133,81	**88,65**

2.4 Conclusions

A set of classifiers based on RF were developed and implemented. These classifiers were trained considering 3 seasons (spring, summer and autumn) and 2 humidity conditions for each season (wet and dry) using different Landsat images. Classifier selection for a new scene was based considering humidity condition estimated through a water balance using ground data. Classifiers were trained using an oversegmented image generated via SLIC algorithm. Afterwards, classifiers were implemented over segments at optimal scale generated with an adaptation of SLIC aiming to have comprehensible segments with a meaningful consistency between homogeneity and neighborhood separability.

Different data set were used as input (NDVI and a set of bands) to SLIC algorithm, showing similar results when OOB errors were compared in both data sets. As a validation of segmentation process generally is complicated because in some cases requires delineated segments to validate, the use OOB error is a feasible and easy option because the classification with generated segments is evaluated. Due similar results between both data sets, NDVI was used to generate the results and the following steps in the thesis.

Features used in the classifiers were mean, standard deviation, mode and median from a set of original Landsat bands and different indexes. OOB feature importance showed that metric mean for blue, near infrared, surface temperature, NDVI, Water index, greenness, and entropy bands had the main influence over the classification. This results suggests that in our case the other metrics have not a clear relation with the classes and these metrics can be not considered in a similar application.

Classification accuracies were over 83% in all scenes, while main misclassifications (considering classes that then can be selected as anchor objects) occurred when Bare soil

was misclassified by Urban and Mixture$_{S-V}$ classes, and when VC$_{HV}$ was misclassified by Water. However, these errors can be solved using some conditions in the post classification process.

These results shows that this methodology can be used in similar implementations of image classification, in which a temporal range of images composed by different conditions (humidity and seasonal) are considered.

Chapter 3

Generation of ET maps through GEOBIA approach

3.1 Introduction

In this Chapter the main proposed methodology of the present Thesis is described, which consists in the generation of ET maps based on the GEOBIA approach following the conceptual diagram showed in Figure 1 in Part IV of this Thesis.

The need for a robust selection of anchor pixels in the METRIC model has motivated some methodologies to accomplish this goal. Morton (2013) and Allen et al. (2013) proposed different approaches to minimize the error occurrence produced by the users and to improve ET estimation. Despite this, these approaches still require some human intervention and some calibrations for new landscapes, which was demonstrated in Chapter 1 with a low robustness in the ET estimation regarding different areas to identify anchor pixels, even when these areas have similar land covers. Moreover, even in the same ROI some anchor pixels generate very different ET estimation.

Classification generated via GEOBIA approach presents advantages compared with traditional pixel based approach because GEOBIA provides more information from object shape and contextual association that can be used to re-classify a preliminary class (Johansen et al., 2010). This contextual information can be generated considering spatial and temporal relationship, in the first case the neighborhood of segments are analyzed, while in the second one the contextual information is also extracted from scenes captured in different time but in the same location and it is used mainly in video processing (Sun et al., 2009).

Previous Chapter carried out training process of the classifiers based in spectral features of segments in order to generate 8 classes, which in the present Chapter will be used to find the anchor objects considering additional contextual rules. This implementation will be carried out in new scenes for the same training site, such as in a different study site.

3.2 Materials and methods

As it was mentioned in Chapter 2, multiple classifiers were trained from different scenes considering seasonal and humidity conditions, and will be applied to new scenes considering both season and humidity attributes.

3.2.1 Preprocessing

As in the Training process, the bands have to be preprocessed in order to generate a standard set of at surface reflectance used as input to the classifier.

The selected gap filling methodology is the G-F$_{local}$, which is implemented using the at top of atmosphere reflectance estimated following steps found in Allen et al. (2010).

Implementation process is carried out over segments at optimal scale aiming to generate objects with a meaningful consistency between homogeneity and neighborhood separability, and generate fewer segments to reduce the computational load. Scales and number of segments for each one is shown in Figure 2.2. Details about optimal scale segmentation are found in Chapter B.

Data set used in segmentation and classification processes are the same than those explained in Chapter 2, i.e. NDVI for segmentation process and for classification process: surface reflectivity for blue, green, red, NIR, SIR1 and SIR2 bands; surface temperature in Kelvin degrees, surface albedo, NDVI, SAVI, Tasseled Cap transformation, Water index and Entropy. With the exception of that the metrics are extracted from segments at optimal scale instead of being at finest scale.

3.2.2 Implementation process

Output in the first classification corresponds to 8 classes, which are: Vegetation cover with high vigor (VC$_{HV}$), Vegetation cover with low vigor (VC$_{LV}$), Forest and shrub, Urban, Water bodies, Stubble, Mixture between soil and vegetation (Mixture$_{S-V}$), and Bare soil. From these classes, anchor objects have to be selected considering that cold object has to be a crop coverage without water stress, while hot object has to be agricultural soil. Since these conditions, cold and hot objects will be selected from VC$_{HV}$ and Bare soil classes, respectively. Anchor objects identification consists in two steps: contextual analysis and application of statistic filters.

Contextual analysis

This analysis allows to avoid anchor objects that can be erroneously selected from an urban or from banks of river coverages. In addition, object size is considered for two reasons, to avoid the selection of small objects in order to select more extensive and homogeneous coverages of soil bare or VC$_{HV}$, and to avoid an object to be rejected if a very small neighbor is urban or water class, supposing that some small misclassification can be generated. Also,

DEM (Digital Elevation Map) is used to reject objects that are located on mountainous zones, filtering all objects that have a slope greater than 10 degrees. All rules related with this analysis are shown in the Algorithm 1.

Algorithm 1 Anchor objects identification

Input: Object O with a preliminary class
Output: Object O with a final class (Cold or Hot candidate; Other class)
{*All considered Neighbors must be greater than O*}
if O is VC_{HV} **then**
  if Neighborhood is Urban or Water **or** Size is less than 100 pixels **or** Slope is greater than 10 degrees **then**
    O=Other class
  else
    O=Cold Object Candidate
  end if
else if O is Bare soil **then**
  if Neighborhood is Urban or Water **or** Size is less than 100 pixels **or** Slope is greater than 10 degrees **then**
    O=Other class
  else
    O=Hot Object Candidate
  end if
else
  O=Other class
end if

Filtering

In order to select the final anchor objects, statistical filtering was done considering the extreme temperature in the selection of both anchor objects, similar concept followed by Allen et al. (2013) in the automation of anchor pixels selection. In this sense, the coolest and hottest objects were selected as final candidates to anchor objects. In Allen et al. (2013) a primary filter of the top 5% of NDVI in an agricultural region of interest achieve identify almost of vegetative coverage, then, a new filter of pixels in the bottom 20% of temperature is implemented to find the final candidates to cold pixel. In our case, the first filter is unnecessary since RF classifier achieves the high vigor crops identification. Since this and aiming to implement similar criteria for the filtering to Allen et al. (2013), the implemented filtering in the present research are:

- Cold Object Candidate in the bottom 20% of temperature
- Hot Object Candidate in the top 20% of temperature

In addition, to select the final cold and hot object, homogeneity characteristics are considered. To accomplish this goal, cold and hot objects that have the least standard deviation in the temperature attribute are selected as final anchor objects.

3.2.3 METRIC model with GEOBIA approach

Main algorithms of METRIC model are detailed in Chapter D in the Appendix. In addition, as it was detailed in section IV, two METRIC implementations are carried out in this research, the first one is done over original pixels maps of Landsat images ($\text{METRIC}_{Geobia-pixels}$), while the second implementation is done over segments ($\text{METRIC}_{Geobia-segments}$) generated using the optimal scale segmentation. In both implementations, anchor objects selected are used in METRIC model, making it possible to compare both results and to find differences attributable to segmentation process.

Implementation of $\text{METRIC}_{Geobia-pixels}$ is simpler because, in comparison with classical METRIC, only change the consideration of attributes from anchor objects instead anchor pixels. Implementation of $\text{METRIC}_{Geobia-segments}$ is more complex, because an assignation for each intermediate parameters must be done for all segments in the image. In this sense, the mean is considered for attribute assignation for all input bands.

3.2.4 Validation process

Validation is done considering to accomplish the proposed hypothesis, i.e., to validate the homogeneity of the ET segments, and validate the robustness of the proposed methodology considering the anchor objects selection.

Validation of ET segments homogeneity is accomplished considering ET pixels generated by $\text{METRIC}_{Geobia-pixels}$, that belong to segments generated by $\text{METRIC}_{Geobia-segments}$. This analysis provides an indicator of how homogeneous the segments are considering ET values generated with same parameters of METRIC model.

Robustness validation is perfofmed comparing the response of fraction of reference evapotranspiration (ET_rF) in function to different candidates of anchor objects, similar approach used in Chapter 1 in order to analyze the sensitivity of the original METRIC model ($\text{METRIC}_{Original}$). This validation method allows to compare both implementations

of METRIC model: selecting anchor pixels with classical rules, and METRIC model with GEOBIA approach.

In addition, a validation of ET_rF magnitudes is done comparing estimated ($METRIC_{Geobia-pixels}$) versus measured ET_rF (henceforth called $ET_rF_{measured}$). In this regard, segments that are inside of measurement station footprints are averaged to be able to obtain a correct comparison between estimated and measured. $ET_rF_{measured}$ is estimated considering the ET (measured by the Eddy Covariance and Surface Renewall systems installed in each study site) and calculated ETr using meteorological data, i.e., $ET_rF_{measured}=ET/ETr$.

3.2.5 Study Site

Results were generated for different seasons in two study sites, the first site is the same that was used in the training process but considering all scenes in the seasons 2011-2012 and 2012-2013 (henceforth called *Site a*). While the second site is the same considered in Chapter A, which have an Eddy Covariance station installed in a Cherry crop (henceforth called *Site b*). In that Chapter, more details about crop, location, management and climatic characteristics of this site can be found.

3.3 Results

3.3.1 Robustness validation

As it was detailed in Chapter 2, the first step to implementing the methodology is a hierarchical segmentation at optimal scale, considering NDVI as dataset for segmentation algorithm. Then, classification using the Random Forest classifiers is implemented, moreover, using a contextual analysis all segments that have same class and are neighbor, are joint in a new segment. Next, the rules to identify the anchor objects from classes VC_{HV} and Bare soil are implemented.

As anchor object candidates come from specific land covers, then, it is possible to analyze their temporal evolution. Figure 3.1 shows temporal evolution of anchor objects identified for all scenes in the *Site a*. These temporal evolutions are: total area, number of objects and mean size of each object. A logical increasing of the area in cold anchor objects is observed in period of full crop status, near January in this site (Summer), due to optimal environmental and irrigation condition for the crops. Following this idea, area

of cold anchor objects decreases when Autumn season is coming due to environmental conditions and harvest period.

Figure 3.2 shows the variation in the ET_rF generated through $METRIC_{Geobia-pixels}$ using different anchor objects identified in the image. These results can be compared directly with those showed in Chapter 1 for 2012-092 and 2012-364 scenes. Those results showed approximated variations ranging from 0.6 to 1.15, and from 0.6 to 0.95, for 2012-092 and 2012-364 respectively. Otherwise, results in Figure 3.2 show variations from 0.85 to 1.1 for scene 2012-092, and from 0.7 to 0.9 for scene 2012-364. A reduction of the variation of ET_rF values was detected when anchor objects were used. Moreover, 0.05 was the average standard deviation for ET_rF in all scenes showed in Figure 3.2, with a maximum of 0.075, indicating that this minimal variation is consistent in all scenes.

Similar behavior of ET_rF is observed in Figure 3.3 for *Site b*, but in this site it is not possible to compare the robustness because this site is different than the one used in the sensitive analysis. Despite this, it can also be seen a low variation of ET_rF in each scene, with an average standard deviation of 0.04.

3.3.2 Validation with ground measurements

Table 3.1 shows the comparison of estimated and measured ET_rF for both study sites and the scenes where both, measured and estimated data, were available. Estimated ET_rF was extracted from $METRIC_{Geobia-pixels}$, because this experiment generates pixel maps as well as $METRIC_{Original}$ implementation. Moreover, ET_rF from $METRIC_{Original}$ is shown, aiming to have a comparison with $METRIC_{Geobia-pixels}$. This comparison allows to evaluating only anchor objects selection, without incorporating the influence that the objects generation could induce.

Results in Table 3.1 show that in *Site a* the RMSE is slightly greater in $METRIC_{Geobia-pixels}$ than $METRIC_{Original}$. But, in contrast, the MSE (mean signed error) for $METRIC_{Geobia-pixels}$ is less than in $METRIC_{Original}$. This indicates that while $METRIC_{Geobia-pixels}$ have estimated points that overestimate and underestimate ET_rF, all together are closer than estimated using $METRIC_{Original}$. On the other hand, *Site b* shows better results using $METRIC_{Original}$ than $METRIC_{Geobia-pixels}$. In addition, in both implementations a consistent overestimation is shown. This overestimation can be explained because original implementation of METRIC model in orchards generates an overestimation due mainly to the surface roughness estimation, which is done considering empirical equation developed to annual crops.

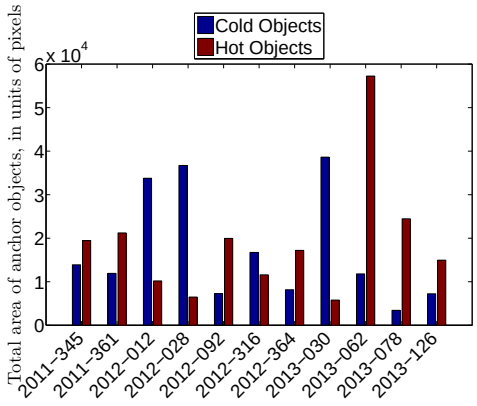

(a)

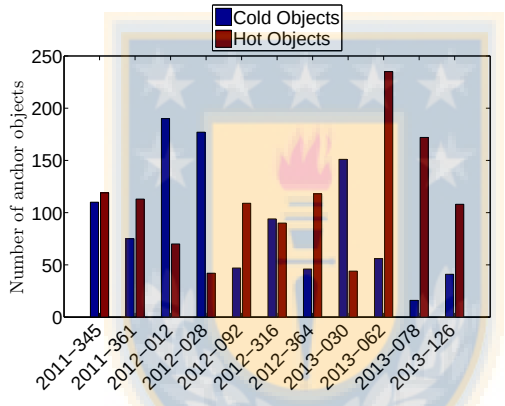

(b)

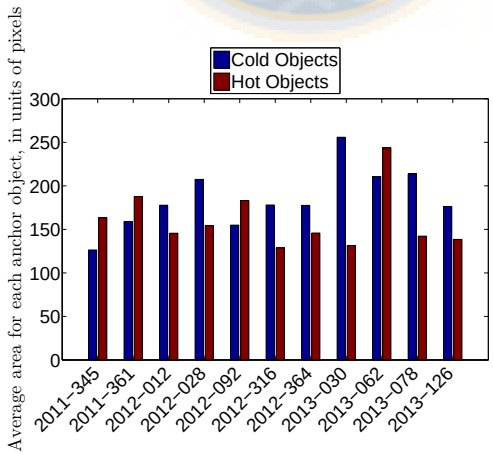

(c)

Figure 3.1: Spatial evolution of anchor objects identified in each scene for *Site a*. 1 pixel corresponds to 900 m^2.

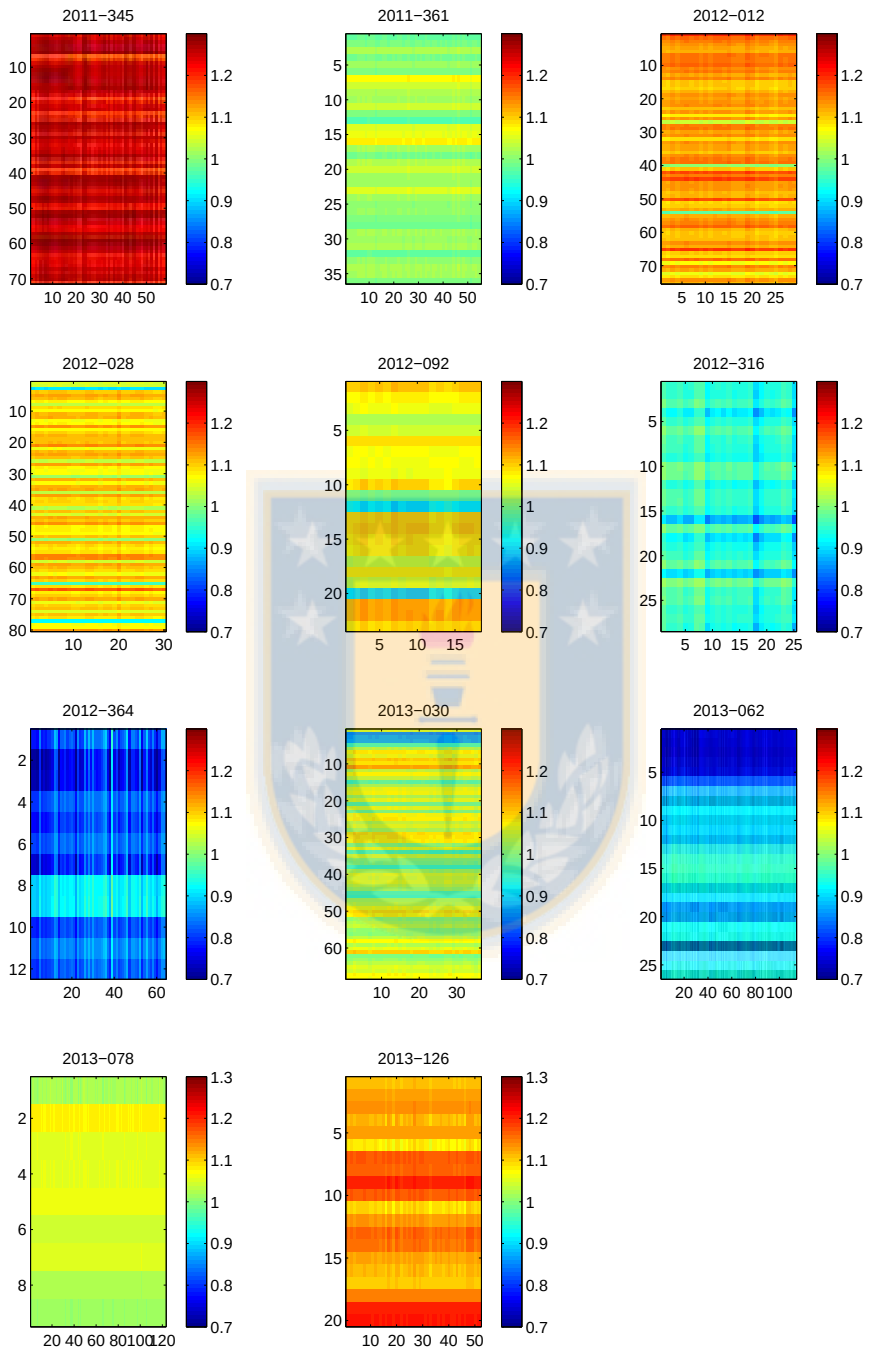

Figure 3.2: Variation in ET_rF generated by all anchor objects identified by the proposed methodology in all scenes of *Site a*. Variations in columns represent hot anchor objects, while variations in rows represent cold anchor objects.

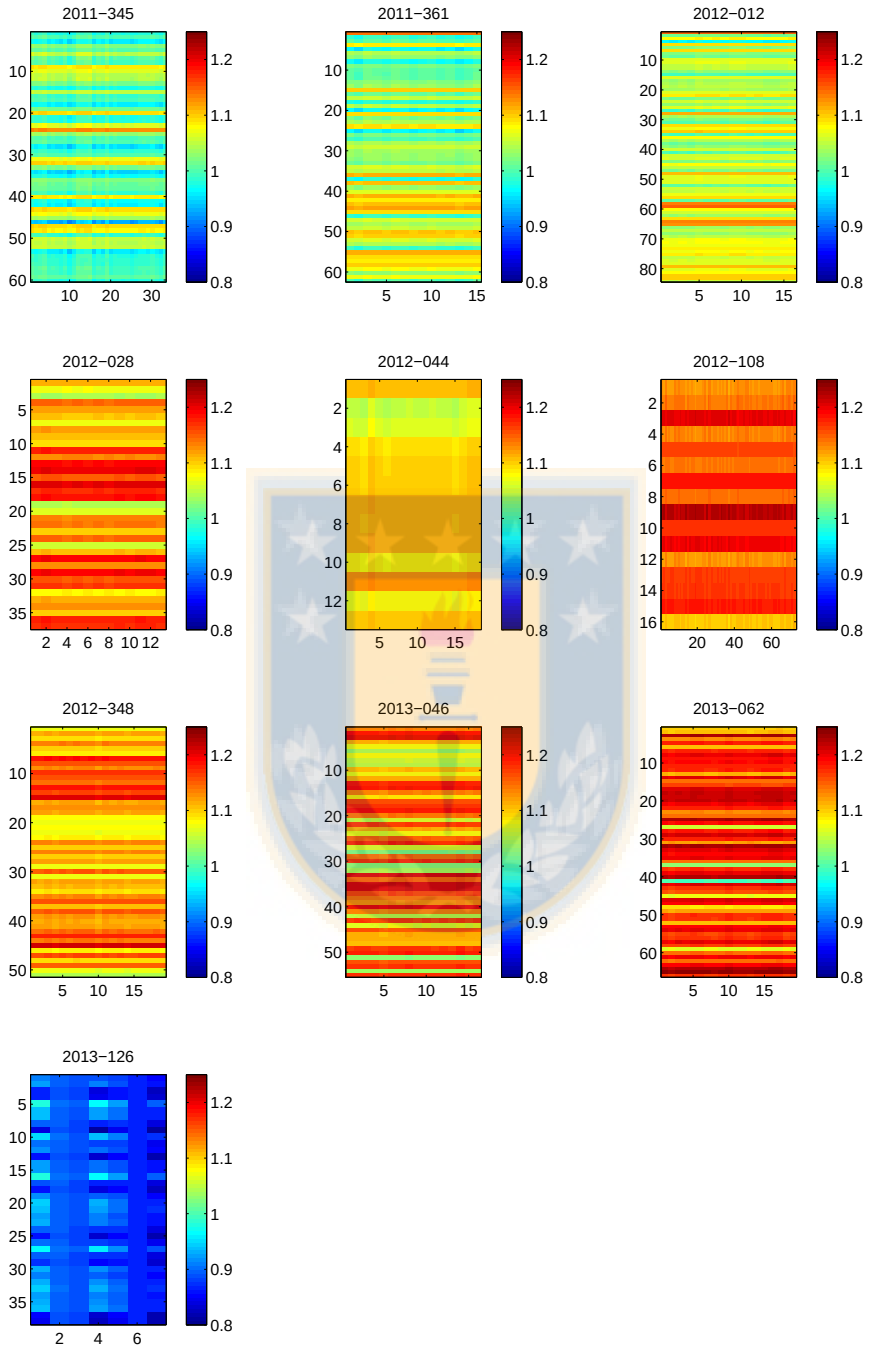

Figure 3.3: Variation in ET_rF generated by all anchor objects identified by the proposed methodology in all scenes of *Site b*. Variations in columns represent hot anchor objects, while variations in rows represent cold anchor objects.

	Site a			Site b		
	$ET_rF_{measured}$	$METRIC_{Geobia-pixels}$	$METRIC_{Original}$	$ET_rF_{measured}$	$METRIC_{Geobia-pixels}$	$METRIC_{Original}$
2011-345				0,67	1,07	0,84
2011-361	1,16	1,05	0,93	0,67	1,10	0,76
2012-12	0,99	1,12	0,93	0,67	1,14	0,95
2012-28	1,05	1,11	0,97	0,71	1,20	1,04
2012-44				0,66	1,11	0,91
2012-92	0,95	1,09	0,89			
2012-108				0,47	1,13	1,05
2012-348				0,84	1,14	0,97
2012-364	1,01	0,68	0,87			
2013-30	1,00	1,06	0,90			
2013-46				0,83	1,17	0,98
2013-62				0,71	1,22	1,06
2013-78	0,86	1,04	0,79			
2013-126				0,67	0,86	0,85
RMSE		0,17	0,12		0,45	0,30
MSE		0,02	-0,11		0,42	0,25

Table 3.1: Comparison between measured crop coefficient ($ET_rF_{measured}$) and estimated ET_rF using $METRIC_{Geobia-pixels}$ and $METRIC_{Original}$ approach in both study sites for all images.

3.3.3 Homogeneity validation

Previous sections addressed the improvement in robustness and validation with measurements of METRIC model using the proposed GEOBIA approach in the selection of anchor objects. In this section the homogeneity of ET objects is validated comparing pixel values from $METRIC_{Geobia-pixels}$ with values of ET segments generated through $METRIC_{Geobia-segments}$.

Table 3.2 shows the analysis for objects with classes *Vegetation with high vigor* and *Vegetation with low vigor*, including the standard deviation of ET pixels generated by $METRIC_{Geobia-pixels}$ belonging to objects generated with $METRIC_{Geobia-segments}$ (STD_{intra}), and the absolute difference of ET between each objects and their neighbors ($|Diff_{neighbors}|$). STD_{intra} for all objects was 0.35 mm day^{-1} for all scenes, which is a good result considering that all objects of these classes were included in this analysis. In addition, $|Diff_{neighbors}|$ averaged for all scenes and sites was 0.77 mm day^{-1} and the magnitude had a relation with the season analyzed, i.e., that in summer $|Diff_{neighbors}|$ tends to be greater than other seasons due that in summer there are many irrigated coverages with high ET unlike their neighbors of natural landscape with water restriction.

Maps of ET for all scenes in *Site a* and *Site b* are shown in Figures 3.4 and 3.5, respectively. In these maps can be observed the seasonal change in ET, presenting

	Site a		Site b	
	STD_{intra} (mm day^{-1})	$\lvert Diff_{neighbors}\rvert$ (mm day^{-1})	STD_{intra} (mm day^{-1})	$\lvert Diff_{neighbors}\rvert$ (mm day^{-1})
2011-345	0.519	0.919	0.326	0.703
2011-361	0.275	0.571	0.426	0.913
2012-12	0.450	0.845	0.408	0.874
2012-28	0.371	0.709	0.249	0.518
2012-44			0.344	0.626
2012-92	0.365	0.536		
2012-108			0.194	0.346
2012-316	0.189	0.253		
2012-348			0.297	0.614
2012-364	0.393	0.571		
2013-30	0.429	0.792		
2013-46			0.249	0.514
2013-62	0.372	0.651	0.227	0.469
2013-78	0.335	0.564		
2013-126	0.135	0.160	0.073	0.135

Table 3.2: Homogeneity analysis of ET segments for all scenes and both study sites analyzed.

the highest ET in January. In the Table 3.2 is observed that in *Site a* the minimum $|Diff_{neighbors}|$ are on scenes 2012-316 and 2013-126. This can be observed more clearly in the Figure 3.4 where in both scenes there are a similar ET over all coverages in the image. Both scenes correspond to beginning and ending of summer, where differences in the soil water condition between irrigated crops and natural landscapes are minimal, for this reason $|Diff_{neighbors}|$ is low. Similar analysis can be done for *Site b*.

3.4 Conclusions

GEOBIA approach to estimate ET using the METRIC model were proposed, implemented and validated. The proposed methodology use anchor objects selected considering segmentation and classification processes, followed by contextual and statistical criteria.

The main goal of the proposed methodology was to increase the robustness of METRIC respect to the selection of anchor objects (classically called anchor pixels).

Robustness to select anchor objects was improved by the decreasing of the variability of ET_rF for candidates to anchor objects in comparison with anchor pixel candidates, which was validated analyzing two scenes. This validation considers that anchor pixels were identified in 4 sectors in the image, while anchor objects were identified in entire image, being an advantages for the proposed methodology because is not necessary to delineate

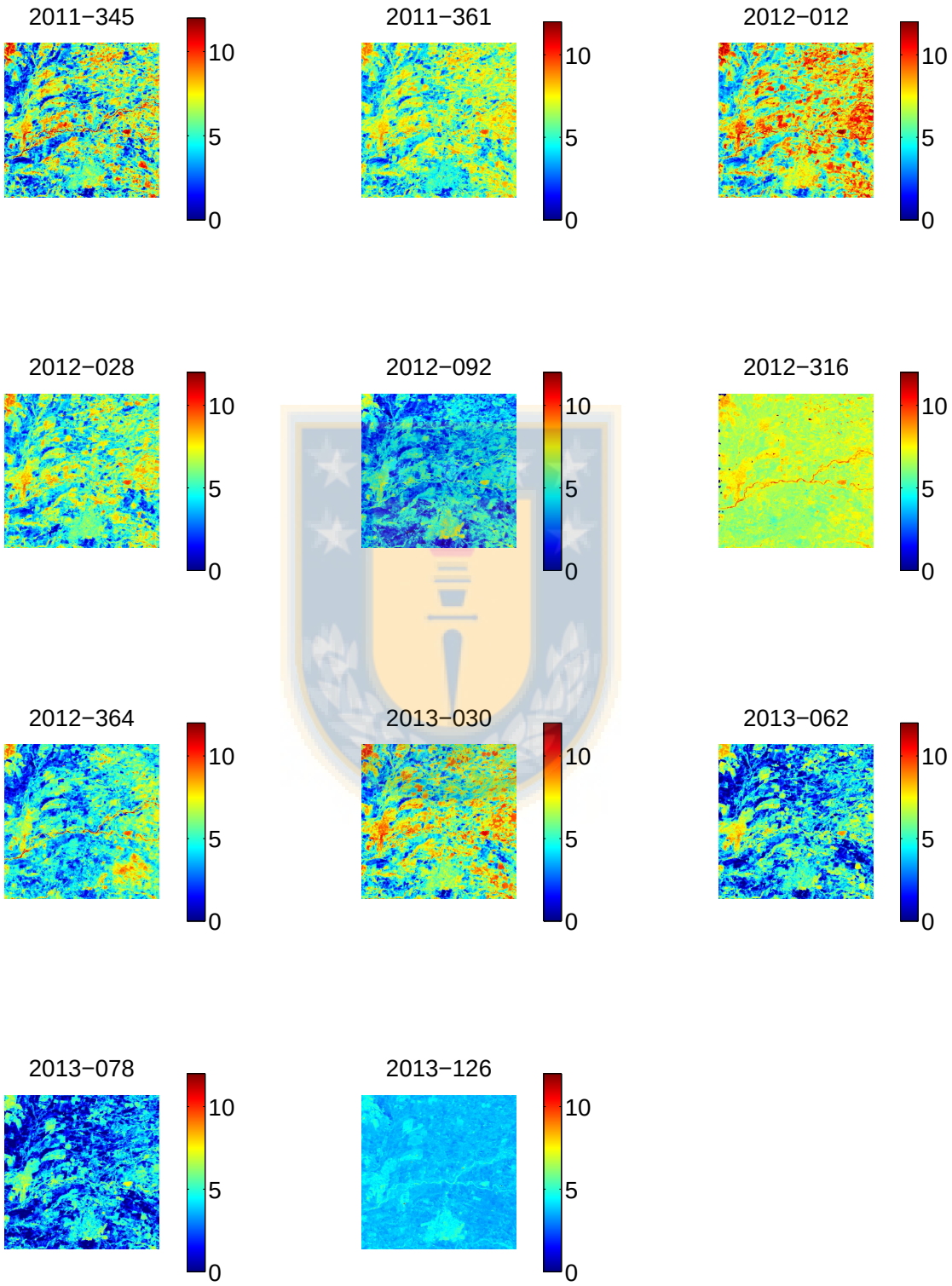

Figure 3.4: Maps of daily ET (mm day^{-1}) generated for *Site a* using METRIC$_{Geobia-segments}$ methodology.

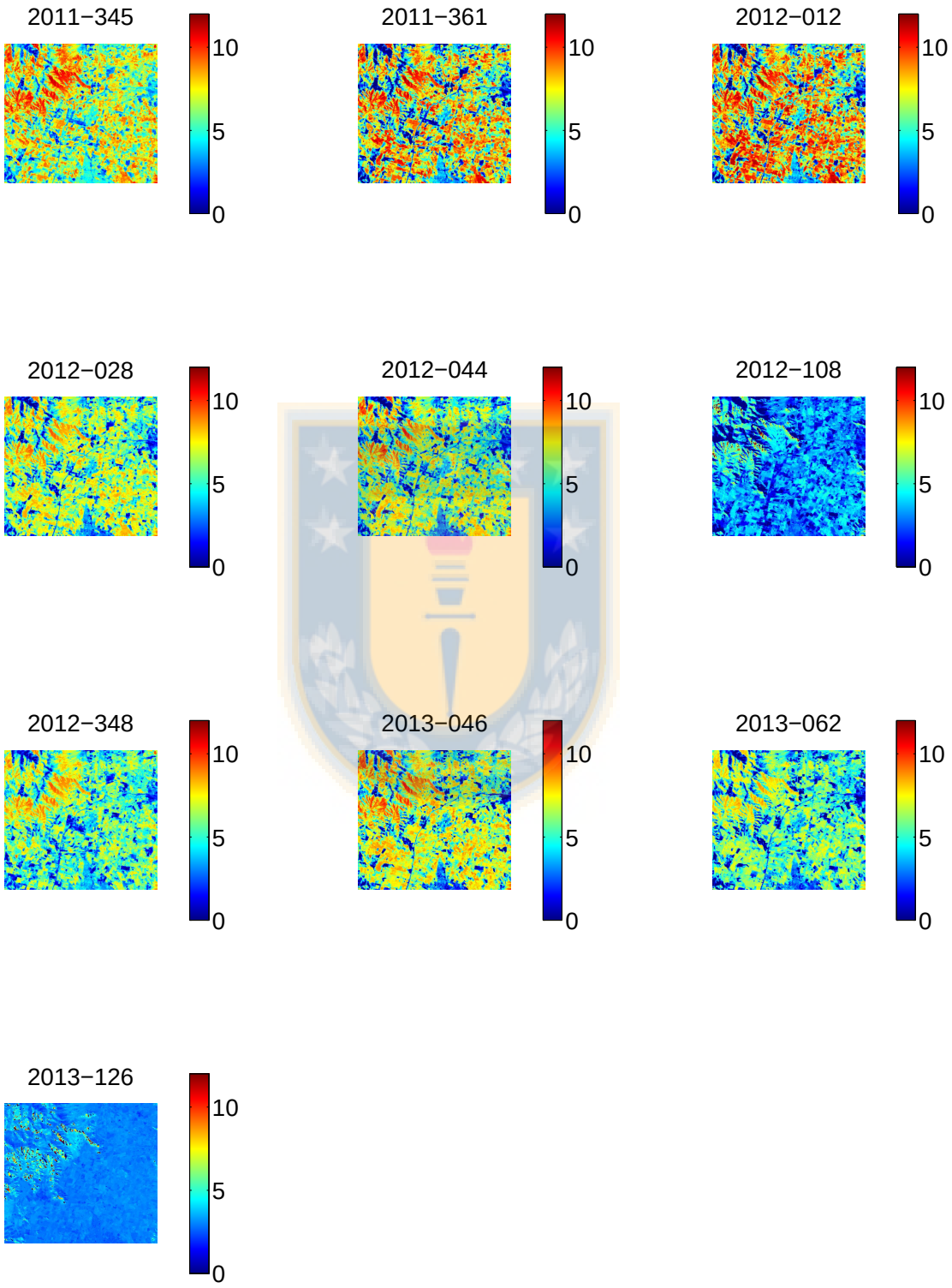

Figure 3.5: Maps of daily ET (mm day^{-1}) generated for *Site b* using METRIC$_{Geobia-segments}$ methodology.

region of interest where find these objects.

In addition, although the robustness of the methodology was validate only in two scenes, in remaining analyzed scenes the standard deviation of ET_rF for all objects candidates was low.

Homogeneity analysis for ET objects for classes *Vegetation with high vigor* and *Vegetation with low vigor* showed a low standard deviation which indicated that segmentation process generated meaningful and consistent segments, in a spatial and spectral sense. Furthermore, inter variability of object was calculated using the absolute difference of ET between each segments and their neighbors, which was 0.6 mm day^{-1} in average for all scenes and sites. These both results indicate that ET objects are homogeneous and correctly separated from one another.

Despite this, it is important to mention that validation of ET_rF with measured data showed that the error of the proposed methodology was slightly higher to original implementation of METRIC model.

The improvement in the robustness of anchor objects selection contributes to avoid human dependency and to implement models that can be reproduced in different scenarios without considering great changes. Following this idea, it is important to mention that the classifiers used in this work can be implemented in images with similar landscapes used in training process.

Part VI

General conclusions

GEOBIA approach allowed to improve the robustness in the selection of anchor objects, decreasing the variation in the model response in function of all candidates to anchor objects identified in the image. Using the proposed methodology is not necessary to delineate regions of interest where to find anchor parameters. In addition, trained classifiers were used in a different study site to where they were trained, which is an improvement because allows to estimate ET maps in different sites without supervision.

This improvement was possible through: an oversegmentation process for training and segmentation in optimal scale for ET objects generation; classification process using random forest that considered phenological and meteorological information allowing to separate classes of interest for anchor objects selection; and geometrical, contextual and statistical information that were used to final selection of anchor objects from all candidates.

Homogeneity analysis showed that in ET objects with classes *Vegetation with high vigor* and *Vegetation with low vigor* the standard deviation was 0.34 mm day^{-1} while the averaged absolute value of the difference of each generated ET objects and their neighbors was 0.6 mm day^{-1} for all scenes and sites analyzed, suggesting that all ET objects are homogeneous and correctly separated from one another.

However, it has to be mentioned that the proposed approach showed an error slightly greater than original implementation of METRIC model. This disadvantage can be addressed considering additional experiments, e.g., to use different segment descriptors, such as median or mode, in the segments characterization.

In this sense, future lines of this research can be oriented to improve the object description, using different metrics such as those mentioned, moreover to use new maps to consider additional information to improve the object characterization. On the other hand, it is possible to explore other physical or nonphysical parameters that can be used to refine the selection of final anchor objects (e.g., albedo, net radiation, indexes from images, etc.), and to consider spatial, temporal and hierarchical (relations between objects at different scales) characteristics in order to extract information that is potentially available in the images.

Appendices

Appendix A

. Local parameterization of METRIC model in Cherry and Sugar beet crops (sent to *Chilean Journal of Agricultural Research*)

Local parameterization of METRIC model in Cherry and Sugar beet crops

The format of the publication has been adapted to the Thesis format.

Authors: David Fonseca-Luengo, Luis Octavio Lagos and Mario Lillo-Saavedra.

A.1 Abstract

The use of remote sensing data for estimating crop evapotranspiration (ET) has been implemented and validated in numerous regions around the world. One of the models used to generate ET maps is METRIC (Mapping EvapoTranspiration at high Resolution using Internalized Calibration), that considers a surface energy balance (SEB) to estimate the latent heat flux. Until now, the majority of crops analyzed with METRIC model has been annual crops with homogeneous and full canopy coverage, same crops for which the model has been developed. The main objective of this study is to analyze the local surface roughness parameterization of METRIC model over 2 different crops (Cherry and Sugar beet) with measurements, using Landsat-7 ETM+ images during seasons 2011-2012 and 2012-2013. Results were validated comparing ET estimated and measured from Eddy Covariance and Surface Renewal systems. The implementation of the parameterization decreased the RMSE (Root mean square error) from 1.31 to 1.13 mm day^{-1} in Cherry crop, while in Sugar beet crop the RMSE slightly increased from 0.74 to 0.84 mm day^{-1}. In addition, MSE (Mean signed error) decreased from 1.22 to 0.86 mm day^{-1} in Cherry crop, and 0.07 to 0.06 mm day^{-1} in Sugar beet crop. Results indicate that the local roughness parameterization improve the estimation of ET on partially covered crops (such as tree crops).

Keywords: Local parameterization, METRIC, Remote sensing and surface energy balance.

A.2 Introduction

Through remote sensing techniques several models to estimate crop evapotranspiration (ET) have been developed. Normally, physically-based and empirical approaches and

their combination have been considered including input data from visible, near infrared and thermal infrared spectral bands. Among the physical-empirical models based on the surface energy balance (SEB) approach, SEBI (Surface energy balance index) (Meneti and Choudhary, 1993), TSM (Two-source model) (Kustas and Norman, 1999) and ETMA (Evapotranspiration mapping algorithm) (Loheide and Gorelick, 2005) can be mentioned. There are other models that use the reflectance-based crop coefficient method to estimate ET; these models are simpler to implement but they need to consider the water stress status and specific calibration for each crop type (Gowda et al., 2008).

One of the latest models widely utilized is the METRIC model (Allen et al., 2007), based almost entirely on the SEBAL model (Surface Energy Balance Algorithm for Land) developed by Bastiaanssen et al. (1998a,b). Both models perform ET estimation of a crop solving the surface energy balance using multispectral satellite images in the optical, near infrared and thermal ranges. In the original implementation, SEBAL and METRIC models requires supervision and the selection of model parameters (named anchor pixels) by the operator. This supervision generates a dependence of the model and it could be a source for human error in the generation of results. In order to decrease this dependency and the associated human error possibilities, in Allen et al. (2013) an automation of the METRIC model based on statistics was developed. This is also intended to be helpful to the use of the model by inexperienced operators in the selection of anchor pixels.

ET estimation by SEBAL and METRIC models has been widely validated in several agro-climatic conditions in countries such as Spain, Turkey, India, Sri Lanka, China, Mali and United States among others (Hemakumara et al., 2003; Bastiaanssen et al., 2005; Zwart and Leclert, 2010). SEBAL and METRIC models have been used to estimate ET to irrigation scheduling (Santos et al., 2008, 2010; Droogers et al., 2010; Kamble et al., 2013), the generation of crop coefficients (Singh et al., 2012; Tasumi et al., 2005; Singh and Irmak, 2009), and the development of strategies for the assessment of irrigation performance at a basin scale (Awan et al., 2011; Burkhalter et al., 2013). However, these applications have been mainly carried out in full coverage crops. These full coverage crops were for which somes equation of SEBAL and METRIC models were initially developed, and then a full validation in partially covered crops such as orchards it is needed (Poças et al., 2014).

A validation in partially covered crops has been mentioned in Poças et al. (2014), Pôças et al. (2013) and Santos et al. (2012). In these works the implementation of the METRIC model in olive crops was analyzed, adjusting the length of roughness (z_{om}) to the actual crop conditions based on the crop density and Perrier roughness function (Perrier,

1982), that integrate information from the leaf area index and canopy architecture. The implementation of this new approach for the length of roughness estimation improved the ET estimations with METRIC, which in Santos et al. (2012) resulted in a decrease of the RMSE (Root mean square error) from 1.12 to 0.25 mm day^{-1}.

The main objective of this study was to analyze the parameterization of surface roughness in Cherry and Sugar beet crops using the METRIC model. This was done aiming to highlight the possible improvements in ET estimation considering measured parameters. Results were compared with ET measurements from an Eddy Covariance and a Surface Renewal systems.

A.3 Materials and methods

A.3.1 Study sites

Two study sites were considered, where Site 1 and Site 2 correspond to Cherry and Sugar beet crops respectively:

Site 1: This site is located in the coordinates 34° 6' 43" S and 70° 41' 9" W, the total area of the farm is 63 ha, while the area of the study site is 6 ha. The crop corresponds to Bing variety Cherries planted in 2003, with a plantation frame of 4 m between rows and 3 m between plants, with a rows orientation from northeast to southwest, a canopy height of 5 m and a drip irrigation system using 2 drippers per plant of 4 L h^{-1} each one. This zone has a Mediterranean climate, with prolonged dry season and an annual rainfall of 370 mm, the annual mean temperature is 13.9 °C (Novoa et al., 1989). The soil corresponds to an OHiggins series, which is an alluvial soil composed by a mixture between loam and clay. In depth the soil texture changes from loam to sandy clay loam until 110 cm (Ciren, 1996).

Site 2: This site is located in the coordinates 36° 32' 11"S and 72° 8' 25" W. It corresponds to an annual sugar beet crop, which is changed annually between Sandrina, Magnolia and Donella varieties. The plantation frame is 0.5 m between rows and 0.07 m between plants, with a center pivot irrigation system with I-Wob emitters. The total area of the farm is 450 ha, and the area of crop covered for the center pivot (study site) is 17 ha. The climate is warm temperate, the annual mean temperature is 14°C, with short dry season and annual rainfall that varies from 1,000 to 1,300 mm (Novoa et al., 1989). The soil corresponds to a Macal Poniente series, which is Inceptisol soil. This soil is formed by recent alluvial sediments with contribution of volcanic ash, located close to Ñuble river.

This soil has a well drained deep sandy loam texture (Ciren, 1999; García et al., 2005).

A.3.2 Instrumentation

Site 1: The Eddy Covariance system consists of a tridimensional sonic anemometer (CSAT3Campbell Scientific, Logan, UT, USA); a $CO2/H2O$ open-path gas analyzer (model EC150, Campbell Scientific, Logan, UT, USA) mounted at 1.5 m above the canopy; humidity and air temperature sensors (HMP45C Campbell Scientific, Logan, UT, USA); a net radiometer placed at 1.5 m above the canopy (Kipp & Zonen model NR-Litle 2, Delft, NLD); a pyranometer (Li-Cor LI200X, Campbell Scientific, Logan, UTUSA); two soil heat flux measurement plates placed above the row of crop (Hukseflux model HFP01SC Campbell Scientific, Logan, UT, USA); soil moisture using Em5b Analog Data Logger (Decagon Devices, Pullman, WA, USA) and 4 10HS sensors at different depths (Decagon Devices, Pullman, WA); thermocouples for measuring soil temperature (TCAV, Campbell Scientific, Logan, UT, USA); and a pluviometer(Texas Electronics TE525, Campbell Scientific, Logan, UT, USA).

Site 2: The Surface Renewal (SR) system consists of a net radiometer sensor mounted at 1.5 m above the canopy (Kipp & Zonen model NR-Litle 2, Delft, NLD net radiometer); a pyranometer (Li-Cor LI200X, Campbell Scientific, Logan, UTUSA); two plates for soil heat flux measurement (Hukseflux model HFP01SC Campbell Scientific, Logan, UT, USA); thermocouples for soil temperature (TCAV, Campbell Scientific, Logan, UT, USA), a 3-D sonic anemometer (Model 81000, RM Young Company, USA), measurements of temperature and air humidity (HMP45C Campbell Scientific, Logan, UT, USA); high-frequency temperature using two fine-wire 76.2 μm diameter FW3 thermocouples (Campbell Scientific, Inc., Logan, UT), pluviometry (Texas Electronics TE525, Campbell Scientific, Logan, UT, USA), and measurements of soil moisture using Em5b Analog Data Logger (Decagon Devices, Pullman, WA, USA) and 4 10HS sensors sensors at different depths (Decagon Devices, Pullman, WA).

The data measured by the EC and SR systems were collected every half hour. Sonic temperature corrections were performed to EC(Webb et al., 1980; Allen et al., 2011). In addition, corrections due to rotation were also performed to the EC and SR systems (Wilczak et al., 2001). Correction in EC was performed using the Bowen ratio (Twine et al., 2000) because has been described that the error in the closure can reach 30%, i.e. the energy used in sensible and latent heat flux can be lower up to 30% respect to the available energy ($Rn - G$) (Twine et al., 2000; Allen et al., 2011; Foken, 2008). This error

can be attributed to the stored energy in the canopy, horizontal advection, energy used in photosynthesis, change in the heat storage in the limit layer below the instrumentation, problems in the frequency response of the sensors and error in the Rn or G (Allen et al., 2011).

Regarding to the area of influence of the measurements in both systems, footprint analysis was calculated in each site using the method developed in Hsieh et al. (2000). Results showed that 90% of the fluxes were coming from less than around 100 m of distance in the Site 1, and less than around 280 m in the Site 2 (more detail in the *Validation* Section). In both sites the fluxes comes from southwest direction, in our case these assure that almost of the fluxes comes from the surface of interest in both sites.

A.3.3 Satellite images

Images were captured by the ETM+ sensor on board of Landsat-7 satellite. Agricultural seasons 2011-2012 and 2012-2013, corresponding to the *path/row* 233/84 (Site 1) and 233/85 (Site 2) were used. Images were downloaded from the USGS Glovis official site (http://glovis.usgs.gov), with 1T preprocessing level of standard field correction. Days (DOY, day of year) and season of image capture are presented in Table A.1.

Due to the failure in the "scan line corrector" (SLC) mechanism of the Landsat-7 EMT+ sensor on May 31, 2003, the imagery requires the implementation of a preprocessing consisting in the gap filling process of pixels without information. In order to achieve this, the method proposed by Scaramuzza et al. (2004) (later published in Storey et al. (2005)) was implemented. In this sense, only in the scenes DOY 92 for Site 1 and DOY 46 for Site 2, the pixels located in the field stations EC and SR were filled.

A.3.4 Meteorological data

The METRIC model requires satellite imagery and environmental parameters (wind speed, solar radiation, air temperature and relative humidity) necessary to calculate alfalfa based reference evapotranspiration (ETr) using the Penman-Monteith equation recommended by the American Society of Civil Engineers, ASCE (Walter et al., 2005). The recommendation to use weather station data is to consider station located in an agricultural area with weather conditions similar to the analyzed scene, and near (within 50 km) the anchor pixels. For Site 1 environmental parameters were obtained from a meteorological stations network administrated by the INIA (Agricultural Research Institute depending from the Chilean

Study site	Season	DOY
Site 1	2011-2012	345, 361, 12, 28, 44, 92, 108
	2012-2013	348, 46, 62, 126
Site 2	2011-2012	361, 12, 28, 92
	2012-2013	364, 30, 46 62, 78

Table A.1: Landsat-7 ETM+ satellite images used in this study. DOY, day of the year.

Ministry of Agriculture) website http://agromet.inia.cl/. Environmental parameters for Site 2 were collected from a weather station located in the Faculty of Agricultural Engineering of the Universidad de Concepción, Chillán Campus. In both sites the weather stations are located within 50 km from each study site.

A.3.5 Preprocessing

As initial step, all bands of satellite images were automatically cut with the use of an interest area mask for each study site. Then, Landsat-7 ETM+ images were transformed into radiance, to reflectance at the top of the atmosphere and finally to surface reflectance with atmospheric correction based in Tasumi et al. (2008) and Allen et al. (2007). Subsequently a gap filling process was implemented using a local regression method from adjacent scenes (Storey et al., 2005). Furthermore, the thermal band was resampled to spatial resolution of multispectral bands to maintain a consistence in the analysis process.

A.3.6 ET estimation model

METRIC model estimates crop ET as a residual of the surface energy balance. It is mainly based on SEBAL model (Surface Energy Balance Algorithm for Land) developed by Bastiaanssen et al. (1998a,b). In SEBAL, to estimate sensible heat fluxes, a relationship between the difference of temperature (dT) (at different heights) and surface temperature (T_s) for two extreme conditions pixels, named as anchor pixels (hot and cold pixels), was proposed.

Using the relation from Equation A.1 it is possible to obtain the dT of each pixel for the whole image. Coefficients a and b are obtained from anchor pixels using an iterative process, proposed in Bastiaanssen et al. (1998a) and modified in Allen et al. (2007). Subsequently, dT is used to estimate sensible heat flux for each pixel. Instantaneous latent heat fluxes are estimated from the surface energy balance model (Equation A.2). Using Equation A.3 the Fraction of the ET estimated and reference ET is estimated (ET_rF), that in general sense is similar to the wydely used crop coefficient (Kc), but with the difference that ET_rF can include local behavior and conditions of the crop. ET_r is the reference ET calculated from station data in the instant of image capture, and ET_{inst} is the instantaneous ET estimated from METRIC model. Finally, using the Equation A.4 it is possible to estimate the daily ET (ET_d) through of ET_rF and reference ET for daily period (ET_{r-d}).

$$dT = b + a * T_s \tag{A.1}$$

$$LE = Rn - G - H \tag{A.2}$$

$$ET_rF = \frac{ET_{inst}}{ET_r} \tag{A.3}$$

$$ET_d = ET_rF * ET_{r-d} \tag{A.4}$$

A.3.7 Automatic selection of anchor pixels

The automatic selection of anchor pixels was implemented based on the method proposed by Allen et al. (2013), except that previous knowledge of the study zone for the selection of zones of interest were used instead of land use maps.

Two groups of cold and hot pixels candidates are generated. These groups are sorted depending on the quality of these pixels to be selected as anchor pixels, according to Allen et al. (2013).

In the current methodology, a test of each pair of anchor pixels candidates is implemented setting 20 iterations per default in the process proposed by Bastiaanssen et al. (1998a) to obtain a and b coefficients. The next criteria were developed by personal experiences aiming to select the correct anchor pixels, considering to pass to the next pair

of candidates: if the standard deviation of b (from iteration 15 to 20) was higher than 5; or the difference between the value of the current a and the previous a (previous iteration) was higher than 10 (from 6 to 20 iteration). If these criteria do not occur, then the actual pair of pixels is selected as anchor pixels.

In addition, soil water balance with field data was used to estimate the fraction of water evaporation from the soil ($ETrF_{soil}$). This procedure adjust the evaporation from the hot pixel depending on the soil moisture condition, that consequently influence to a and b parameters of METRIC model.

Finally, all process (image preprocessing, input parameters, automatic selection of anchor pixels, and ET maps generation) were coding in MATLAB software, allowing improve the generation time results and facilitate the experiments implementation.

A.3.8 Estimation of the z_{om} parameter

In SEBAL and METRIC models, z_{om} is calculated from the leaf area index (LAI), Equation A.5 and Equation A.6. These equations were developed in Tasumi (2003) and Allen et al. (2007) for annual irrigated crops from the Kimberly, Idaho, USA. In crops of partial coverage such as orchard, Equation A.6 tends to underestimate the value of crop height (h), which underestimates z_{om} and increase the aerodynamic resistance for sensible heat flux. This process generates a decrease in the sensible heat flux and an overestimation of the latent heat flux (Santos et al., 2012).

$$z_{om} = 0.12 * h \tag{A.5}$$

$$h = 0.15 * LAI \tag{A.6}$$

In order to estimate correct z_{om} values, data extracted from EC and SR stations and the Equation A.7 were used (Rooney, 2001). From Equation A.7 it is possible to estimate z_{om} for stable condition in function of the friction speed (u^*), the von Karman's constant (k) and the wind speed (u_x) measured at the aerodynamic measurement height z_x; where $z_x = z_m - d$, with z_x being the measurement height above the soil surface and d is the zero-plane displacement which is considered 2/3 of canopy height (Foken, 2008).

$$u_x = \frac{u^* * \ln(\frac{z_x}{z_{om}})}{k} \tag{A.7}$$

A.3.9 Validation

Validation was carried out comparing ET estimated by METRIC model versus ET measured by the EC and SR systems. Results of ET estimated were extracted from ET maps as the weighted ET from a mask generated using the footprint analysis (Hsieh et al., 2000). In this sense, three sectors with respective contribution weights considering the results of footprint analysis for around the 90% of the fluxes (Figure A.1). This methodology aims to avoid discrepancies between spatial representativeness of remote sensing products with ground flux measurements (Gelybó et al., 2013; Folhes et al., 2009; Li et al., 2008). Information about each sector of footprint for both sites is shown in Table A.2. Differences in both footprints can be explained by surface roughness, measurement height and wind speed/stability conditions of each site (Hsieh et al., 2000; Li et al., 2008).

This validation method is valid for parameters related with latent energy flux, i.e. evapotranspiration (such as energy flux or water) and ET_rF. Other parameters generated through METRIC model were analyzed using a 3x3 window centered on EC or SR pixel location.

Study site	**Sector**	**weight** (%)	**Distance (m)**
Site 1	A	70	21
	B	18	64
	C	5	106
		Total=93%	
Site 2	A	68	64
	B	16	150
	C	7	277
		Total=91%	

Table A.2: Details of footprint illustrations showed in Figure A.1 that were used in the validation process.

A.4 Results and discussion

A.4.1 Automatic process

The general process was automated, that include the gap filling process and follow the recommendation of Allen et al. (2013) to select anchor pixels. According to this, one ET map of 817x818 pixels was generated in 1.5 min (Processor: Intel Core i7 950 with 4 cores

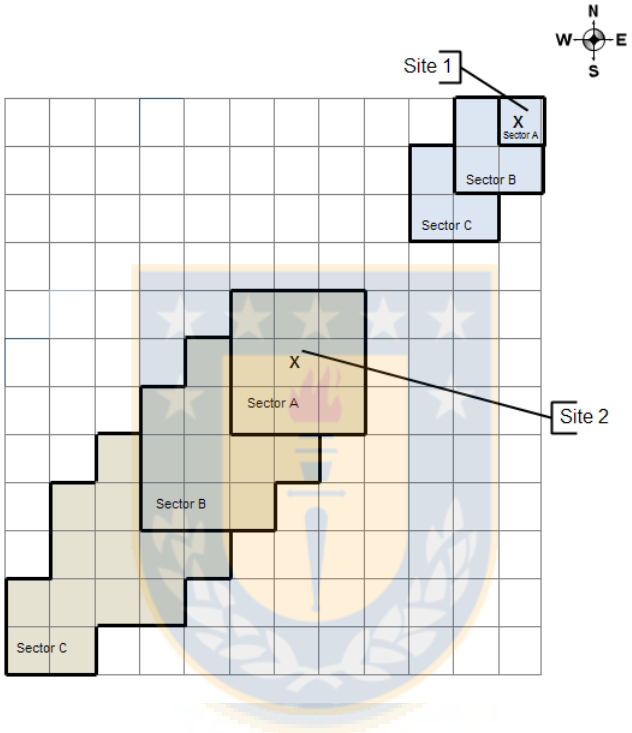

Figure A.1: Illustration that represents both footprints for study sites, these were used to validate ET estimations with EC and SR measurements. The X letter represents the locations of EC and SR systems. Each cell corresponds one pixel of Landsat image, i.e. 30x30 m.

at 3.07GHz; RAM: 8 GB; Operating System: Windows 7 Ultimate). This automation avoids the dependency to operators decreasing possible human errors.

About the stability of a and b parameters, Figures A.2 and A.3 shows the stability for sites 1 and 2, respectively. In both cases the parameters achieve the stability around iteration 7. This indicates that this automation accomplishes a correct pixel selection considering the stability.

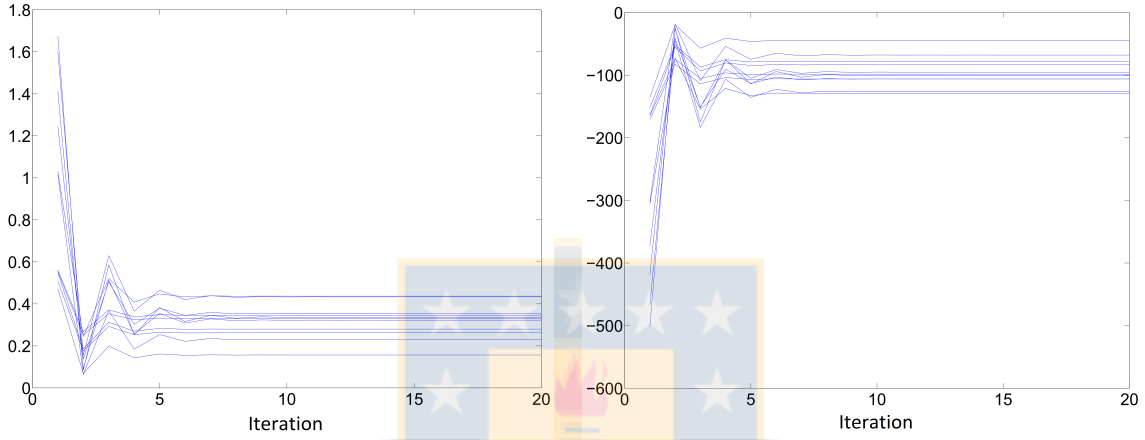

(a) Parameter a (b) Parameter b

Figure A.2: Stability of parameters a and b for Site 1.

A.4.2 Quality of the ET measurements

In order to ensure the quality of measurements of EC systems, the energy balance closure was performed. Previous to the Bowen ratio correction, the closure between available energy (NR-G) versus the energy used in latent and sensible heat flux generated a linear regression with slope and R^2 of 0.68 and 0.89, respectively. After of Bowen ratio correction, the energy balance closure has a slope and R^2 of 0.72 and 0.63. In comparison with literature, this results of the energy balance closure are good, since in literature it has been documented that even after the EC corrections, errors can be higher than 30% (Wilson et al., 2002; Twine et al., 2000; Foken, 2008).

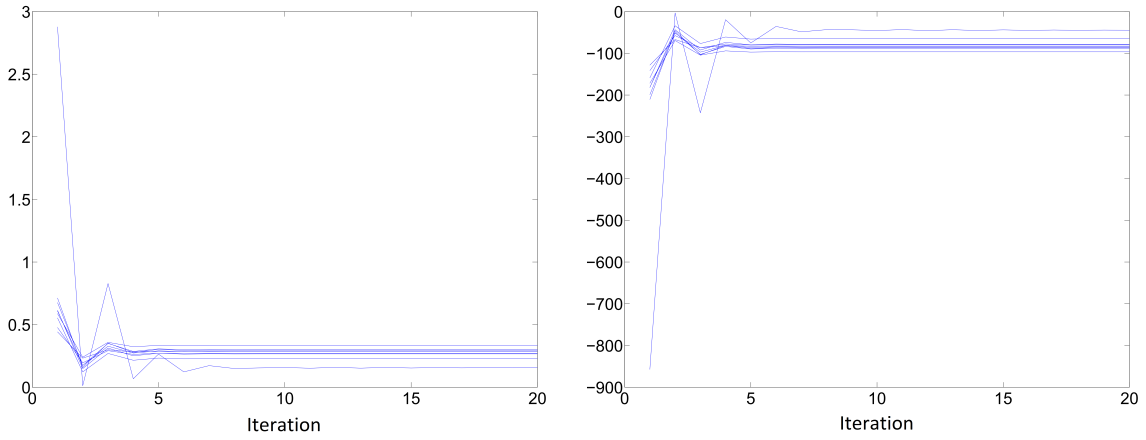

(a) Parameter a (b) Parameter b

Figure A.3: Stability of parameters a and b for Site 2.

A.4.3 Water balance in the soil

In Figure A.4 and Figure A.5 can be observed $ETrF_{soil}$ and precipitation values for sites 1 and 2, respectively. Circles correspond to capture dates of the satellite images. In sites 1 and 2, three scenes were captured after an important rain event. This indicates that there is available soil moisture to be evaporated, then $ETrF_{soil}$ is different from zero ($ETrF_{soil}$ equal to 1). These days correspond to DOY 126 for both sites.

A.4.4 Parameterization of METRIC model using z_{om}

In Table A.3 values of the roughness parameter, z_{om}-METRIC, are shown. These values were estimated by the model recommended by Tasumi (2003) and Allen et al. (2007) (Equation A.5 and Equation A.6). The z_{om}-field was calculated with field data through Equation A.7. In addition, z_{om} and the $\Delta error^1$ in ETd are shown.

Through the use of z_{om}-field in the Site 1 the RMSE decreased from 1.31 to 1.13 mm day^{-1}; whereas in Site 2 the RMSE slightly increased from 0.74 to 0.84 mm day^{-1}. Using the MSE[2] (Mean signed error), the results showed a decrease of MSE in both sites, from 1.22 to 0.86 mm day^{-1} in Cherry crop, and 0.07 to 0.06 mm day^{-1} in Sugar beet crop. These results indicate that model overestimation decreased.

Regarding the $\Delta error$, negative values indicate a major error using z_{om}-field, while

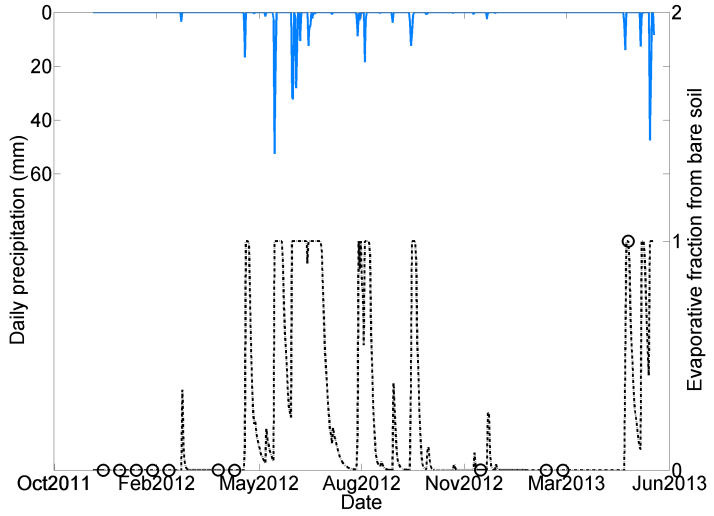

Figure A.4: Temporary series of $ETrF_{soil}$ (black dotted line), precipitation (blue solid line) measured from the monitoring station and capture dates of the satellite images (circles) for Site 1.

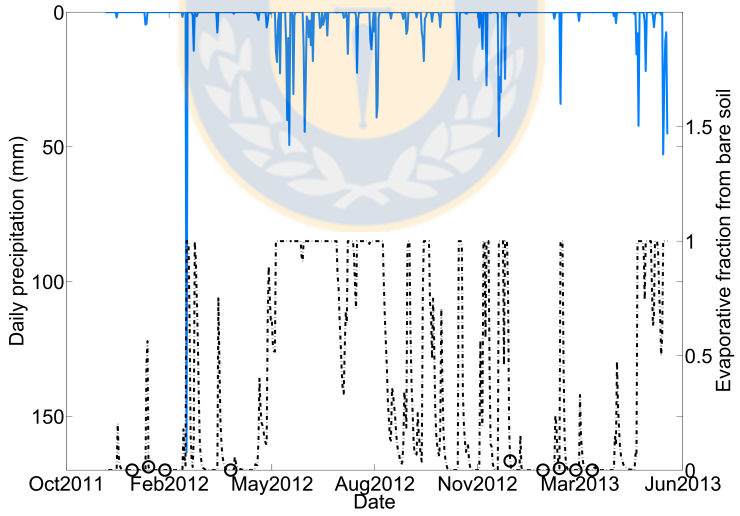

Figure A.5: Temporary series of $ETrF_{soil}$ (black dotted line), precipitation (blue solid line) measured from the monitoring station and capture dates of the satellite images (circles) for Site 2.

positive values indicate a major error using z_{om}-METRIC. It can be observed that for Site 1 in only two scenes the error through z_{om}-field was higher than using z_{om}-METRIC (Table A.3). These results indicate an improvement in the ET estimations for Site 1 by using the roughness estimated in the field, which reinforces the need of parameterize the models that compose METRIC to the conditions of partially covered crops, such as tree crops. In addition, it is observed that in Site 1 in all cases, z_{om}-field exceeded the values of the z_{om}-METRIC.

In the Site 2, almost of the z_{om}-field values are similar to those of z_{om}-METRIC. Nevertheless, unlike Site 1, the use of z_{om}-field tends to increase the error of ET estimation in the Site 2.

Estimation accuracy for sites 1 and 2 increased and decreased, respectively, which can be explained due that models proposed by Tasumi (2003) and Allen et al. (2007) were developed for fully covered annual crops, similar to Site 2, thus the use of z_{om}-field can improve the results in the Site 1 and not necessarily in the Site 2.

In the DOY 46 of Site 2 it was not possible to estimate the z_{om}-field due to a failure in the system. Hence, the z_{om}-field value was maintained but not considered in the statistic analysis.

Figure A.6 shows the comparison between ET estimations through METRIC (z_{om}-field) and ET measurements from EC and SR systems in both study sites, this comparison generate a RMSE of 1.01 mm day^{-1}. Separate analysis by crop shows that Site 1 has a slope of 1.15, and R^2 of 0.82. On the other hand, Site 2 has a slope of 1.00, and R^2 of 0.77. These results are similar to the shown in Poças et al. (2014) for an olive crop, R^2 and slope equal to 0.85 and 1.11, respectively.

In the Table A.4, results using z_{om}-field for parameters a, b and AE for each site are shown. The DOY=126 in the Site 1 present atypical values of a and b in comparison with the other scenes, this behavior is due in this scene the $ETrF_{soil}$ is equal to 1, producing a minimal difference of dT according to surface temperature.

[1] $\Delta error$ corresponding to the absolute value of estimated minus measured ETd using z_{om}-METRIC, minus the absolute value of estimated minus measured ETd using z_{om}-field. ($|ETd_{est} - ETd_{mea}|_{z_{om}-METRIC}$ - $|ETd_{est} - ETd_{mea}|_{z_{om}-field}$)

[2] MSE is the average of the Absolute Error (AE) of each scenes.

[3] z_{om}-METRIC is used due to a failure in extraction of z_{om}-field from the system.

[4] AE correspond to Absolute Error of ET, i.e., estimated minus measured ET

[5] Bold DOY correspond to day with ETr_{soil}=1.

DOY	Site 1			Site 2		
	z_{om}-METRIC (m)	z_{om}-field (m)	$\Delta error$ (mm day^{-1})	z_{om}-METRIC (m)	z_{om}-field (m)	$\Delta error$ (mm day^{-1})
345	0.042	1.037	0.880			
361	0.037	0.926	-0.314	0.088	0.161	0.002
12	0.040	1.628	-0.371	0.087	0.076	-0.039
28	0.033	1.351	0.445	0.088	0.496	0.000
44	0.026	1.451	0.562			
92	0.020	1.270	0.248	0.068	0.085	0.015
108	0.022	1.025	0.202			
348	0.056	0.739	0.469			
364				0.094	0.071	-0.181
30				0.093	0.095	-0.034
46	0.046	0.491	0.173	0.079	0.079[3]	-
62	0.044	0.865	0.025	0.072	0.002	-0.608
78				0.050	0.542	-0.449
126	0.002	0.755	0.196			
mean	0.033	1.049	0.229	0.080	0.191	-0.144

Table A.3: z_{om} and $\Delta error$ values estimated from field data (z_{om}-field) and through empirical original function of the METRIC (z_{om}-METRIC).

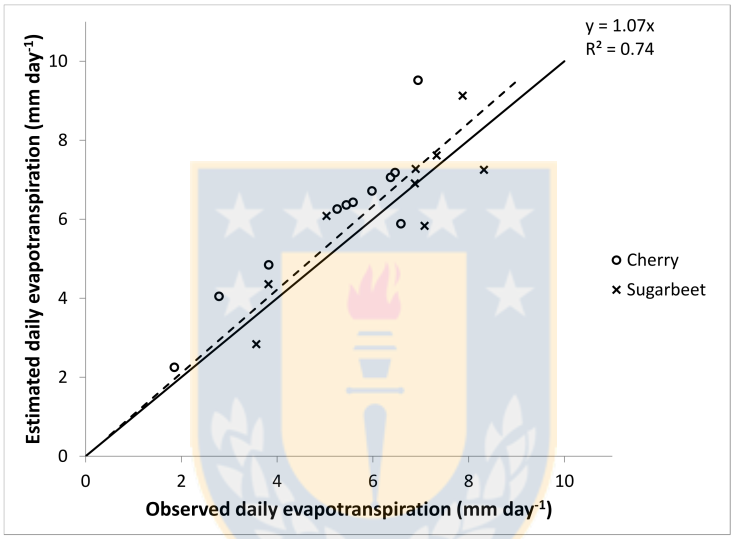

Figure A.6: Goodness of fit of estimated ET_d respect to measurements of EC and SR. Solid line corresponds to 1:1 line.

DOY	Site 1			Site 2		
	a	b	AE [4] $(mm\ day^{-1})$	a	b	$AE\ (mm\ day^{-1})$
345	0.28	-83.51	0.84			
361	0.26	-78.02	-0.70	0.16	-44.81	-1.07
12	0.35	-106.09	2.58	0.27	-79.69	1.25
28	0.32	-95.16	0.69	0.27	-78.30	0.03
44	0.33	-96.37	1.01			
92	0.44	-129.52	1.02	0.29	-82.64	0.54
108	0.43	-126.36	1.26			
348	0.23	-67.84	0.74			
364				0.33	-96.48	0.28
30				0.29	-84.88	0.38
46	0.34	-100.22	0.72	0.30	-86.82	-1.25
62	0.36	-106.09	0.92	0.30	-88.23	1.05
78				0.23	-64.73	-0.73
126 [5]	0.16	-44.84	0.40			
mean	0.32	-94.18		0.27	-78.51	

Table A.4: Results of a and b obtained from anchor pixels in both sites.

A.4.5 Surface energy balance components

Figure A.7 and Figure A.8 shows the comparison between measured and estimated net radiation (NR), soil heat flux (G), sensible heat flux (H) and latent heat flux (LE) for Site 1 and 2, respectively. Was observed that peak of G had a temporal lag of 3 hours respect to NR in both sites, which was considered to extract the measured G for the comparison (Foken et al., 2006). In both sites the LE and NR components have the better linear adjusts, while H and G do not show some relation between estimated and measured. Although the error in G and H estimation, the effect over LE is not so important due the magnitude of G and H fluxes. LE of Site 2 presented better adjust than Site 1 (with slope/R^2 of 0.84/0.80 and 1.23/0.46, respectively), this is ratified with the results previously showed about the better estimation of ET_d in the Site 2 with full cover crop. Singh and Irmak (2011) proposed an improvement to METRIC model, where surface energy balance components were compared with measures from Bowen ratio system, where the NR and LE showed a linear adjust with slope/R^2 of 1.09/0.90 and 1.50/0.70, respectively, showing similar to our results.

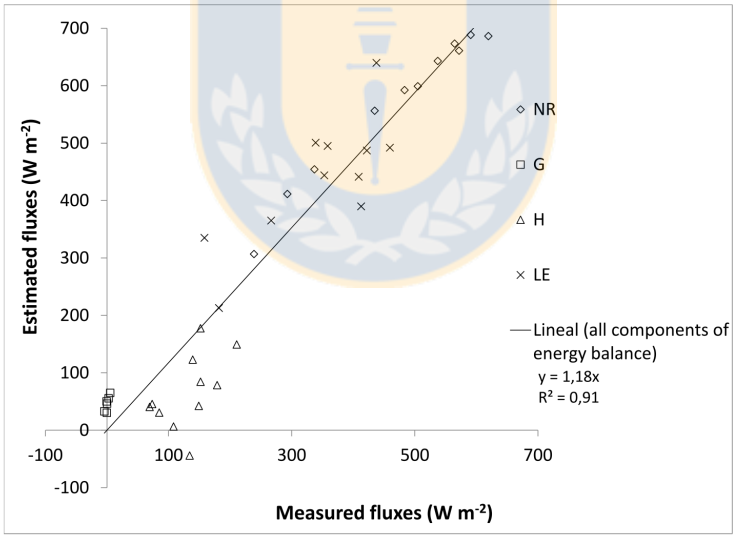

Figure A.7: Comparison of surface energy balance components measured and estimated for the Site 1.

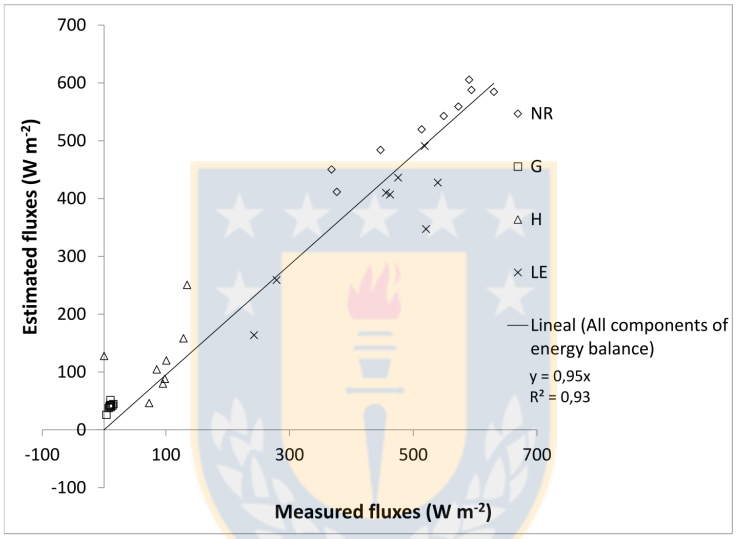

Figure A.8: Comparison of surface energy balance components measured and estimated for the Site 2.

A.5 Conclusions

The parameterization of surface roughness in partially covered crop using ground data allowed decreasing the RMSE from 1.31 to 1.13 mm day^{-1}, due that the mean of z_{om}-field was 1.049, whereas the mean of z_{om}-METRIC was 0.033 meters. In the case of full covered crop the effect of the parameterization was slightly negative, with a increase of RMSE from 0.74 to 0.84 mm day^{-1}, mainly because the METRIC model was developed for fully covered annual crop and, theoretically, it does not need roughness parameterization.

These results motivate to improve the ET estimation using a better estimation of z_{om} for partially covered crops, without the use of measurement from ground systems (Eddy Covariance, Surface Renewal or other systems). One option may be to develop empirical equations of z_{om} according to some vegetation index for partially covered crops.

A.6 Acknowledgments

The author (David Fonseca-Luengo) thanks to the National Commission for Scientific and Technological Research (CONICYT) for support the accomplishment of the Doctoral Thesis.

Authors also thanks to grants FONDEF D09I1069, FONDECYT 11100083, FONDAP 15130015, BMBF-CONICYT 231-2010 and ITECMA2 Laboratory (Faculty of Agricultural Engineering, Universidad de Concepción, Chillán, Chile.), in which the current research has been framed.

Appendix B

. Optimal scale in a hierarchical segmentation method for satellite images (published in *Lecture Notes in Computer Science*)

The format of the publication has been adapted to the Thesis format.

Journal: Lecture Notes in Computer Science (LNCS).

Authors: David Fonseca-Luengo, Angel García-Pedrero, Mario Lillo-Saavedra, Roberto Costumero, Ernestina Menasalvas and Consuelo Gonzalo-Martín.

Faculty of Agricultural Engineering, Universidad de Concepción.
Vicente Méndez 595, Chillán, Chile.
Tel.: +56-42-2208888
Email:davidfonseca@udec.cl

Centro de Tecnología Biomédica at Universidad Politécnica de Madrid.
Campus Montegancedo, 28223 Pozuelo de Alarcón, Madrid, Spain.

B.1 Abstract

Even though images with high and very high spatial resolution exhibit higher levels of detailed features, traditional image processing algorithms based on single pixel analysis are often not capable of extracting all their information. To solve this limitation, object-based image analysis approaches (OBIA) have been proposed in recent years.

One of the most important steps in the OBIA approach is the segmentation process; whose aim is grouping neighboring pixels according to some homogeneity criteria. Different segmentations will allow extracting different information from the same image in multiples scales. Thus, the major challenge is to determine the adequate scale segmentation that allows to characterize different objects or phenomena, in a single image.

In this work, an adaptation of SLIC algorithm to perform a hierarchical segmentation of the image is proposed. An evaluation method consisting of an objective function that considers the intra-variability and inter-heterogeneity of the object is implemented to select the optimal size of each region in the image. The preliminary results show that the proposed algorithm is capable to detect objects at different scale and represent in a single image, allowing a better comprehension of the land-cover, their objects and phenomena.

Keywords:Remote sensing, hierarchical segmentation, multi-scale and high resolution

images.

B.2 Introduction

High resolution images are an important part of the big volume of information generated in almost every domain: health, Earth observation, biology, to name a few. Two main image analysis approaches can be found in the literature. On the one hand, pixel-based approaches interpret images as a set of disconnected pixels, employing only spectral information. On the other hand, images in OBIA (Object Based Image Analysis) paradigm are interpreted as a set of homogeneous areas in the scene (segments), which are considered the minimal unit instead the pixels Benz et al. (2004). The main advantages of the OBIA approach are: i) its capacity of extracting information such as shape, size, texture and contextual relationship from the objects and ii) reducing the computational requirements Homeyer A (2010). Even though in the last years more of the OBIA approaches have been developed in the area of Remote Sensing and Geographical Information Systems Blaschke (2010); Hay and Castilla (2008), applications in other areas like medicine Chitiboi et al. (2013) or neurosciences Lucchi et al. (2012) can also be found.

The OBIA approach consists of two main processes: an initial segmentation for generating segments by grouping neighboring pixels according to some homogeneity criteria, such as color, texture, among others. And a second step, a classification process in which each segment is assigned to a class depending on its features Vieira et al. (2012). Numerous researches have shown that the segmentation process is a critical step in the OBIA approach. This is due to the fact that the results of the classification step strongly depend on the initial segmentation Gao and Mas (2008); Yan et al. (2006).

Nowadays it is fully accepted that natural processes are scale dependent, and most of them are hierarchically structured. Therefore an appropriate understanding of these processes and interactions among them requires the determination of optimal scales Levin (1992). Different segmentations will allow extracting different information from the same image in multiple scales Burnett and Blaschke (2003). Some studies have designed methodologies for estimating a single optimal scale of segmentation for the scene Espindola et al. (2006); Kim et al. (2009). Other studies have implemented a multi-scale approach Zhou and Troy (2009); Trias-Sanz et al. (2008) to address this problem, but in this case the selection of the segmentation scales typically is based on an extensive knowledge of the study site Johnson and Xie (2011). In our approach, image segmentation is carried

out by an adaptation of SLIC algorithm to deal with objects that are scale dependent and hierarchically related in a scene. On the other hand, in our case the selection of the optimal scale segmentation is performed by evaluating the intra-variability and inter-heterogeneity of the regions defined by the coarsest scale in contrast to the evaluation method presented in Johnson and Xie (2011) where the complete scene is used for evaluation.

B.3 Materials and Methods

B.3.1 Data Set

The satellite image was collected on January 18th, 2013 by Pléiades Satellite, in the central irrigated valley of Chile (36° 31' 54" S; 72° 08' 03" O). The area of the scene has 420 hectares and corresponds to 1024×1024 pixels in the multispectral image. The acquired image has a spatial resolution of 2 meters and corresponds to ORTHO-BASIC products, characterized by a basic radiometric normalization (for detector's calibration) and geometric correction (WGS84/UTM 18S projection).

In this work Blue, Green, Red and Near Infrared bands were used to segmentation process. Furthermore, these 4 bands were used in the calculation of the metrics to determine the optimal scale for each parent superpixel.

B.3.2 Methodology

The methodology we propose, inspired by the one presented in Johnson and Xie (2011), is composed of two main processing modules: i) image segmentation, and ii) segmentation evaluation. Though it differs from that one, both in the algorithm used for image segmentation and in the evaluation process followed. In what follows we detail the components of our approach.

Image segmentation.

Simple Linear Iterative Clustering (SLIC) Achanta et al. (2012) is a segmentation procedure based on the well-known *k-means* clustering algorithm to group image pixels into disjoint regions called superpixels. Superpixels are generated according to two criteria: i) color similarity and ii) spatial proximity. Moreover, a weighted distance that combines color and spatial proximity allows the control of the size and compactness of the superpixels Achanta et al. (2012). Two parameters: i) k the desired number of superpixels, and ii) c

the compactness factor have to be settled to run SLIC. Larger values of c results in more compact superpixels as the importance of spatial proximity is emphasized.

A detailed description of the SLIC algorithm working in CIELAB space can be found in Achanta et al. (2012), in this work also the authors demonstrate that the computational complexity of SLIC is linear on the number of pixels in the image.

Superpixels generated by SLIC reduce the influence of noise, preserve most of the edges of the images, and are approximated in size and shape. However, SLIC is not able to generate a hierarchical segmentation. Our approach fills this gap by proposing an adaptation of SLIC that makes the generation of a hierarchical multi-scale segmentation possible.

Based on the fact that in SLIC low values of k results in a coarser segmentation in comparison to finer segmentations obtained increasing the values of k, we propose to generate segmentations at different scales by varying the superpixels size and then combining resulting segmentations.

To establish the different segmentation scales, a vector $K = [k_1, k_2, \ldots, k_n]$ containing different values for the size of the superpixels in ascending order is defined. Each value of the vector corresponds to a different scale (i). Consequently, segments corresponding to a segmentation performed according to k_i will be larger than those of the segmentation according to k_{i+1}. A segment A^i in scale i is considered as the parent of a segment B^{i+1} in scale $i+1$, if the area of B^{i+1} can be entirely covered by segment A^i. The relationship parent-children among segments is shown in Figure B.1. In order to ensure that the resulting segmentation process is hierarchical, segments in scale k_{i+1} are partitioned by segments in scale k_i, obtaining a new segmentation that generally contains a higher number of segments than in the segmentation achieved in scale k_{i+1}. To adjust the number of superpixels in scale $i+1$ to its original number of superpixels, smaller size segment are joined to the most similar neighboring segment belonging to the same parent. We use euclidean distance in the spectral space (color) to define the similarity between neighboring segments.

Evaluation.

The evaluation process that we propose is based on the one proposed in Johnson and Xie (2011) but adapting that one to deal with the hierarchical image segmentation process that has been followed. Thus, in our case we evaluate for each parent segment at the first scale those segments related to it instead of evaluating all the scene as in Johnson and Xie

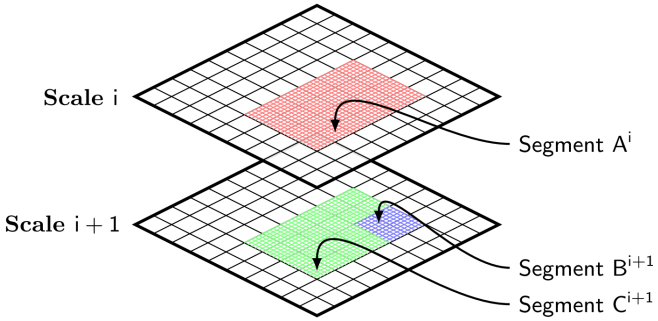

Figure B.1: Segment A^i is considered the parent of segments B^{i+1} and C^{i+1}, as both segments can be covered entirely by segment A^i. Each square of the grid represents an image pixel.

(2011).

The main advantage of this scheme is that it provides different optimal scales for different image regions, against the results showed in Johnson and Xie (2011), where an optimal scale for the whole image is provided. This fact is especially relevant in images where the variability inter-regions is high, as it is the case of natural land-covers in satellite images. A general overview of the evaluation scheme is shown in Figure B.2.

In order to evaluate the segmentation, the following inter and intra-segments quality measures are used:

- the global Moran's index is used to measure the inter-heterogeneity between segments;
- the weighted variance is used for intra-segment homogeneity.

The global Moran's index measures the correlation among segments. It is used to evaluate the similarity of a segment with its neighborhood and is calculated as follows:

$$MI^p = \frac{n \sum_{i=1}^{n} \sum_{j=1}^{n} w_{ij}(y_i^p - \hat{y}^p)(y_j^p - \hat{y}^p)}{\sum_{i=1}^{n}(y_i^p - \hat{y}^p)^2 \left(\sum_{i \neq j} \sum w_{ij}\right)} \tag{B.1}$$

where:

- w is an adjacency matrix among neighbor regions that are relatives of the segment p at scale 1, therefore w_{ij} is equal to 1 if regions i and j are adjacent, otherwise, $w_{ij} = 0$.

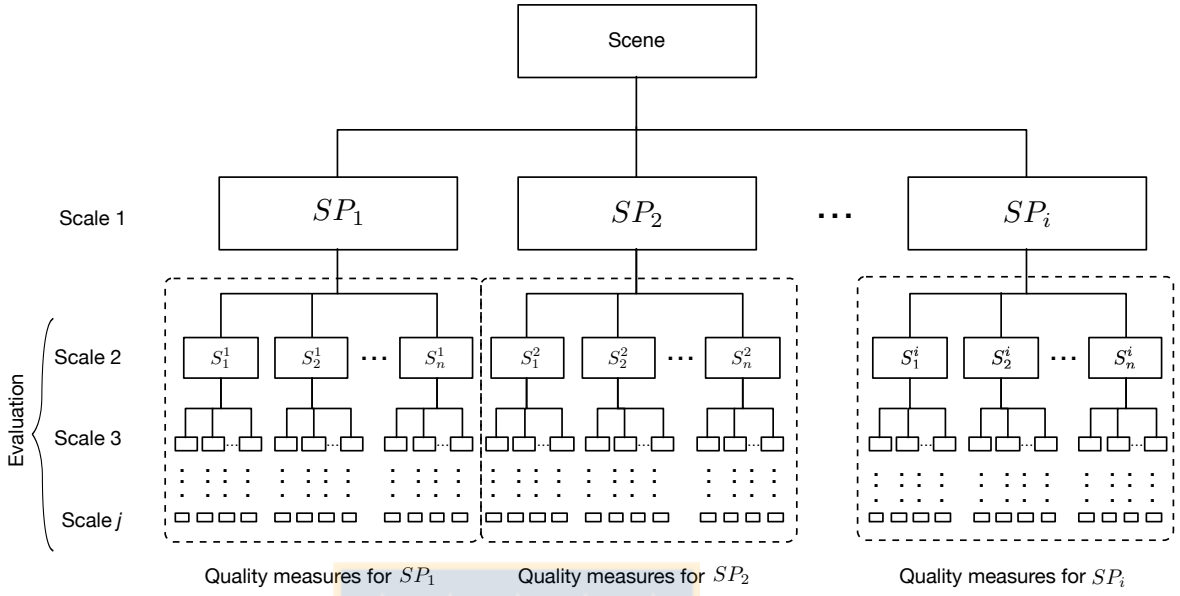

Figure B.2: General overview of the Evaluation process.

- y_i is the spectral average of region i.
- n is the total number of regions at the analysis scale that are related to segment p.

In order to calculate the similarity at a particular scale level only those regions belonging to a certain parent segment p at scale 1 are considered.

The Global Moran's index ranges from the value -1, that corresponds to the perfect dispersion, to 1, that indicates a complete correlation. The 0 value corresponds to a random correlation.

The weighted variance is used for intra-segment quality measure, and is calculated as follows:

$$wVar^p = \frac{\sum_{i=1}^{n} a_i^p v_i^p}{\sum_{i=1}^{n} a_i^p} \tag{B.2}$$

where v_i is the variance pixel that compound the segment i and a_i corresponds to the size of segment i. Values of variance closed to zero indicates homogeneity of a segment. Note that, when calculating this measure bigger size segments have a higher effect in the evaluation than those of a smaller size.

In this paper, the best scale is defined as one the value of the objective function F_i^p is closer to zero, being F_i^p calculated by adding the normalized (range 0-1) of intra and inter-segments measures.

The objective function is calculated as:

$$F_i^p = wVar_i^p + MI_i^p \tag{B.3}$$

where p represents the region of the parent at the scale 1 to which the segments at the evaluation scale i are related.

B.3.3 Experiments

Two experiments were carried out. In the first one, the number of superpixels associated with each scale was generated with a linear spacing. In the second one, the number of superpixels of each scale was generated with a dyadic spacing (2^n). The number of scales used in both experiments was 7, varying from 64 to 4096 superpixels.

B.4 Results and discussion

A color composition of the analyzed multispectral scene is shown in Figure B.3(a). Figures B.3(b) and B.3(c) display the segmented images for the experiments where the scales were generated by a linear and dyadic spacing, respectively. Figures B.3(d) and B.3(e) depict the optimal scales for each parent superpixel (superpixel at the first scale). It can be observed that the number of segments generated by the linear spacing (Figures B.3(b) and B.3(d)) is higher than for the dyadic case (Figures B.3(c) and B.3(e)). This difference is due to the fact that linear spacing generates a higher number of superpixels in the intermediate scales, producing an abrupt change from coarsest to finest scale, and generating an over-segmentation in some homogeneous areas like the irrigation pivots. This is a problem when the results are used as information to improve the agricultural management.

B.5 Conclusions

In this work, a new methodology for optimal scale determination of a hierarchical segmentation method for satellite images has been proposed. An objective function, that

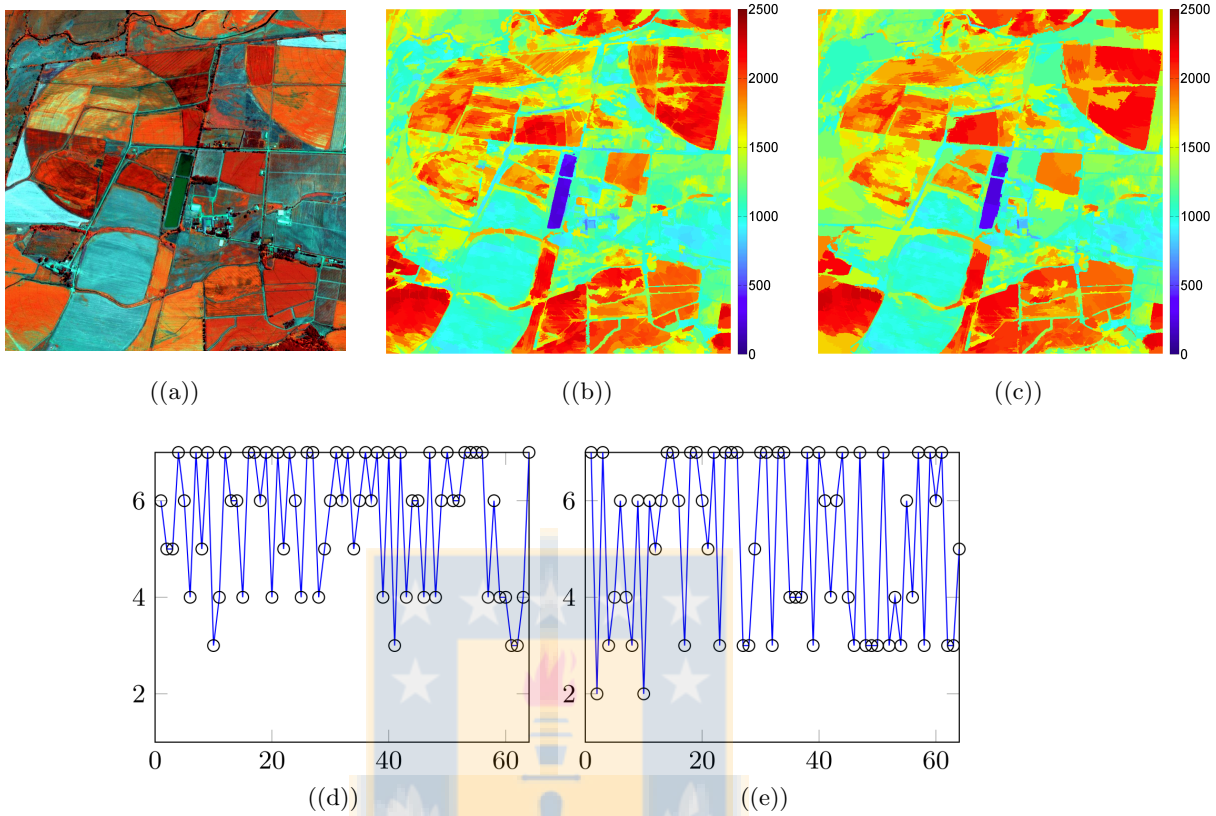

Figure B.3: (a) Color composition (Near Infrared-Green-Blue) of the analyzed scene. (b) and (c) Segmented images for the lineal and the dyadic succession of scales. (d) and (e) the corresponding optimal scales for each parent superpixel.

combines weighted variance and global Moran's index, was used to select the selection of the optimal scale. The main outreach of this proposal is that it provides different optimal scales for different image regions, against the results showed in Espindola et al. (2006), where an optimal scale for the whole image is provided. This fact is especially relevant in images where the variability inter-regions is high, as it is the case of natural land covers in satellite images.

The proposed method allows users to benefit from detecting objects in a image at different scales. This allow a better comprehension of the land-cover, their objects and phenomena.

Finally, given the flexibility of the proposed methodology, is possible to apply in almost

every domain where multi-scale images analysis are required (e.g. health, astronomy, biology).

B.6 Acknowledgements

A. García-Pedrero (grant 216146) and D. Fonseca-Luengo acknowledge the support for the realization of their doctoral thesis to the Mexican National Council of Science and Technology (CONACyT) and the National Commission for Scientific and Technological Research (CONICYT), respectively.

This work has been funded by the Centro de Recursos Hídricos para la Agricultura y la Minería (CONICYT/FONDAP/1513001).

Appendix C

. Gap filling for Landsat-7 ETM+ images

C.1 Introduction

The gap filling process is implemented due to a failure in the "scan line corrector" (SLC) mechanism of the Landsat-7 EMT+ sensor occurred on May 31, 2003. This failure generates pixels without information in some sector of the image affecting around 22% of all pixels (Ju and Roy, 2008). In order to predict the value of each null pixel, some methodologies have been proposed based mainly on three approaches: (1) direct prediction based on the pixel neighborhood, depending only of the image to be filled; (2) prediction based on other temporal Landsat images, which depend of the availability of temporally adjacent images; (3) prediction from other sensors, that depend on spectral and spatial compatibility and capture conditions (Zeng et al., 2013).

One of the first gap filling methodologies was proposed by Scaramuzza et al. (2004) (later published in Storey et al. (2005)). This methodology is based in a linear regression between 2 images of the same scene and near in the temporal space, considering a spatial window around of the pixel to be filled. This methodology is a simple and effective solution to the gaps, but some errors have been detected in some heterogeneous scenes with abrupt changes in the spectral response (Zeng et al., 2013).

There are some methodologies that have the same goal, for example in Chen et al. (2011) was proposed a methodology that implements a similar conceptual process that of Scaramuzza et al. (2004) except that only pixels with spectral response similar to the pixel to be filled are considered in the prediction. According to (Chen et al., 2011) this methodology generates slightly better results that methodology presented in Scaramuzza et al. (2004).

In this research three methodologies were evaluated, which implement the filling of gaps using the prediction based on temporally adjacent images. These methodologies corresponds to the proposed by Scaramuzza et al. (2004) (G-F$_{local}$), Chen et al. (2011) (G-F$_{NSPI}$ based in the method named *Neighborhood Similar Pixel Interpolator*) and a third methodology proposed in this research, which is similar to G-F$_{local}$ but implementing a simple classification by threshold to generate the linear regression (G-F$_{class}$).

C.2 Materials and methods

The general methodology consists in the implementation of different gap filling methods on a scene with artificial gaps, i.e., in a scene without gaps several lines with zero-values are

superposed on the scene. This technique allows the validation of the gap filling methods comparing with the real values in the scene.

C.2.1 Methodologies

The detail of the methodologies implemented in this research are:

1. G-F$_{local}$ implements a local linear regression between the scene to be filled and a scene close in the temporal space. The assumption of this methodology is that there exists a temporal correlation between the pixels behavior in these two scenes. In Storey et al. (2005) three matching methods between the scenes were evaluated: Global linear, global nonlinear, and local linear. The results showed that the best reconstruction of pixels was with the local linear method, with a mean RMS (Root mean squared error) of 6, in unit of digital number (DN), for bands: 1, 2, 3, 4, 5 and 7. However, the three methods have problems in the prediction in presence of clouds. In the present research, the local linear regression was implemented using an initial window of 12x12 pixels, that is extended iteratively with 2 pixels if less that 5 pixels for the regression are found.

2. The methodology G-F$_{NSPI}$ implements a similar technique that G-F$_{local}$ following the same assumption that the neighboring pixels have similar spectral characteristics and temporal pattern changes (Chen et al., 2011). In G-F$_{NSPI}$ an additional step is implemented to select only the similar pixels in the neighborhood to generate the regression. This step is made using the root mean square deviation (RMSD) between all bands in the windows of neighborhood, so that if the RMSD is less than a threshold, the pixel is similar to the pixels to be filled. The threshold is determined by the standard deviation of the image considering an empirical number of classes in the image. In this methodology an initial windows of 20x20 pixels was predefined, and the increase of window size was implemented following the proposed by Chen et al. (2011). Additionally, a weight to similar pixel is proposed in Chen et al. (2011), trying to give more contribution to the pixels that are more similar than the pixel to be filled. Finally, in the Equation C.1 the value (radiance or reflectance) of the predicted pixel for each band (b) is estimated using the multiplication between the weight (W) and the value of the similar pixels (N) in the scene of the pixel to be filled (T). For more detail of this methodology, please refer to Chen et al. (2011).

$$Pixel'_{T,b} = \sum_{j=1}^{N} W_j * Pixel_{similar,T,b} \quad \text{(C.1)}$$

3. The proposed methodology (G-F$_{class}$) has the same approach than that G-F$_{local}$ but a classification of neighboring pixels is implemented before to the linear regression model. The classification allows to select only similar pixels to generate the regression, similar to the goal of G-F$_{NSPI}$. The classification generates 5 land covers based on a thresholding of the Normalized Difference Vegetation Index (NDVI): Crops (0.7≤NDVI≤1), Vegetal$_1$ (0.5≤NDVI<0.7), Vegetal$_2$ (0.3≤NDVI<0.5), Soil (0≤NDVI<0.3) and Water (NDVI≤0). All following processes are the same than those in G-F$_{local}$.

C.2.2 Study site and images

The evaluation of the methodologies described is implemented on a scene located on the coordinates 32°20'00" S and 70°53'00" O, in the path/row: 233/83. The study site is located in the center of the Landsat since an image without gaps is necessary to implement the evaluation process.

The study site corresponds to a small scene with crops in different phenological stages, bare soil and hills. Figure C.1 shows the scenes of the study site in the false color composition IGB (Infrared-Green-Blue). In the Figure C.1, some pivot irrigation systems can be observed, which have high dynamic changes in temporal and spatial scale (considering the neighborhood of pixel that are not pivot) which make difficult the behavior modeling of the pixels by the methodologies.

Two masks of artificial lines of gap pixels are extracted from two consecutive (in temporal space) similar Landsat scenes but in other location, therefore the gaps have the original characteristics of form, length and orientation. The different artificial lines masks are overlapping in the scene to be filled and the scene close in the temporal space in order to represent a real gap condition.

The scene to be filled corresponds to November 25, 2011; and the scene used to extract information for prediction is from December 11, 2011. The evaluated bands in this research are: blue, green, red, near infrared, shortwave infrared-1, thermal infrared and shortwave infrared-2 (corresponding to 1, 2, 3, 4, 5, 6 and 7 bands in Landsat-7 ETM+ order). All images were transformed to surface reflectance using the equations detailed in Allen et al.

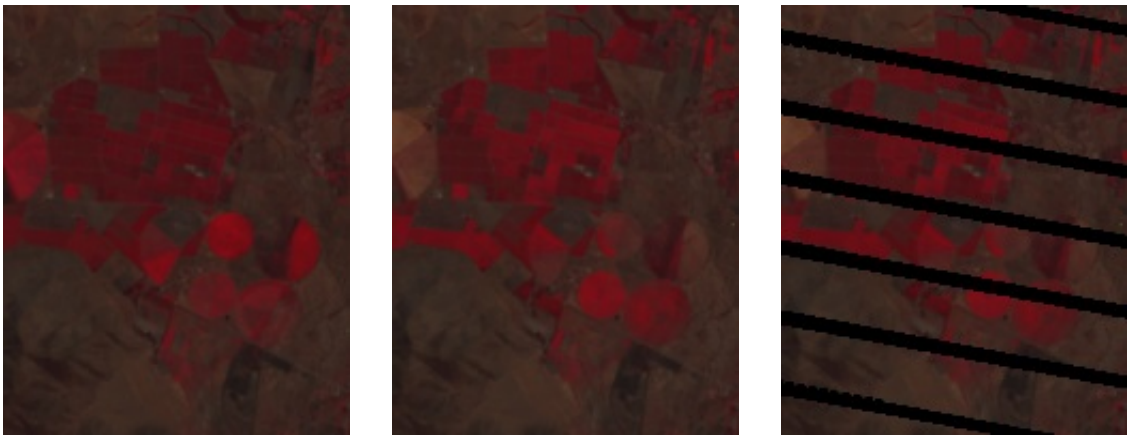

(a) Scene used to filling pixels (b) Scene to be filled (c) (b) with artificial lines of gap

Figure C.1: Scenes used in the evaluation. The intense red color represent a vigorous vegetative cover.

(2010).

C.3 Results

Figure C.2 shows the different results in prediction of pixels without information. It can be observed that there are not great differences between the results and the original image, despite that there are differences in the stage of the crop in some irrigation pivots.

For more detail on the results, in Table C.1 the normalized RMSE can be observed for each band (in Landsat-7 ETM+ order) and methodology used. The G-F$_{local}$ methodology generates the lowest error incidence in the pixel prediction, although all methodologies have low RMSE.

Methodology	B1	B2	B3	B4	B5	B6	B7	Mean RMSE
G-F$_{local}$	3,1	3,2	3,2	4,6	4,9	4,8	4,4	4,1
G-F$_{NSPI}$	3,8	3,8	3,9	6,3	6,3	6,5	5,6	5,2
G-F$_{class}$	3,4	3,7	3,6	4,8	6,4	5,5	5,0	4,6

Table C.1: Normalized RMSE (%) in each band filled by the different methodologies.

(a) Original scene to be filled

(b) Filling using G-F$_{local}$ (c) Filling using G-F$_{NSPI}$ (d) Filling using G-F$_{class}$

Figure C.2: IGB composition of the filled scene using the different methodologies.

In Figures C.3, C.4 y C.5 the 1:1 scatter plots can be observed between the original and predicted pixel values of each band and methodology. The most notorious difference is that found between the estimation by G-F$_{NSPI}$ for the band 6 and the other methodologies. G-F$_{NSPI}$ underestimates the thermal values in a small range at medium temperature (around 310° K), maybe this can be produced because G-F$_{NSPI}$ finds the similar pixel in the neighborhood using all bands, but the response of thermal band can be not related to multispectral bands.

C.4 Conclusions

Analyzing the results showed, it can be observed that the best methodology in the prediction of pixel values is G-F$_{local}$. This contradicts the result of Chen et al. (2011), because in that research G-F$_{NSPI}$ presented best result that G-F$_{local}$. This contradiction can be explained by the fact that in Chen et al. (2011) the parameters required in the methodology were estimated for the scene used, however in the present research some parameters were used directly.

About the G-F$_{class}$ methodology, this can improve the result if some better classification process or inclusive segmentation process is implemented.

Finally, according to our results, G-F$_{local}$ methodology is the best option to predict pixel without values for Landsat 7-ETM+ images. This is due to the best results in the prediction, the null requirements of parameters in the implementation (this is useful to implement over other scenes with different landscapes) and the runtime of execution (that not was shown in this research but can be mentioned).

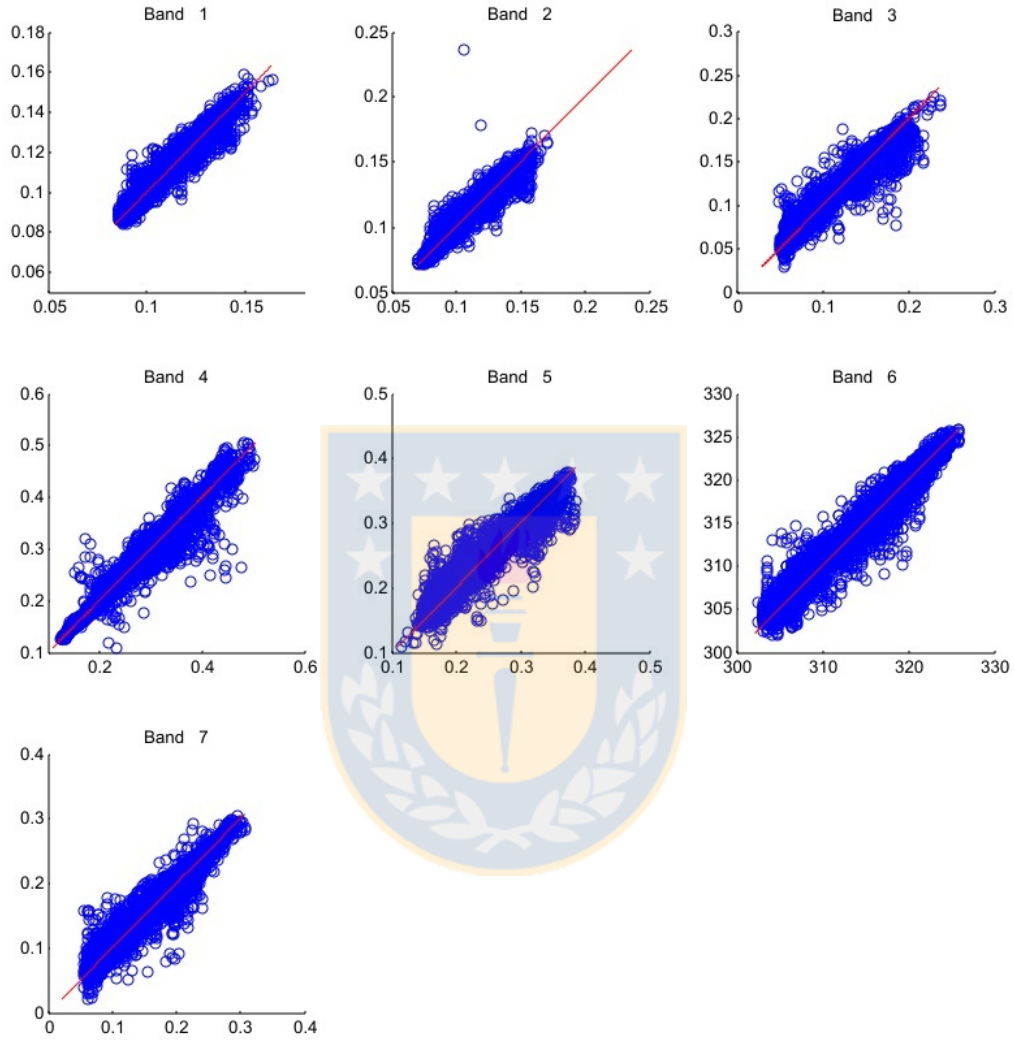

Figure C.3: Scatter plots of original (x axis) versus predicted (y axis) values by G-F$_{local}$ methodology for each band. Unit for 1, 2, 3, 4, 5 and 7 bands is reflectance at top of atmosphere, while the unit for band 6 is Kelvin degrees.

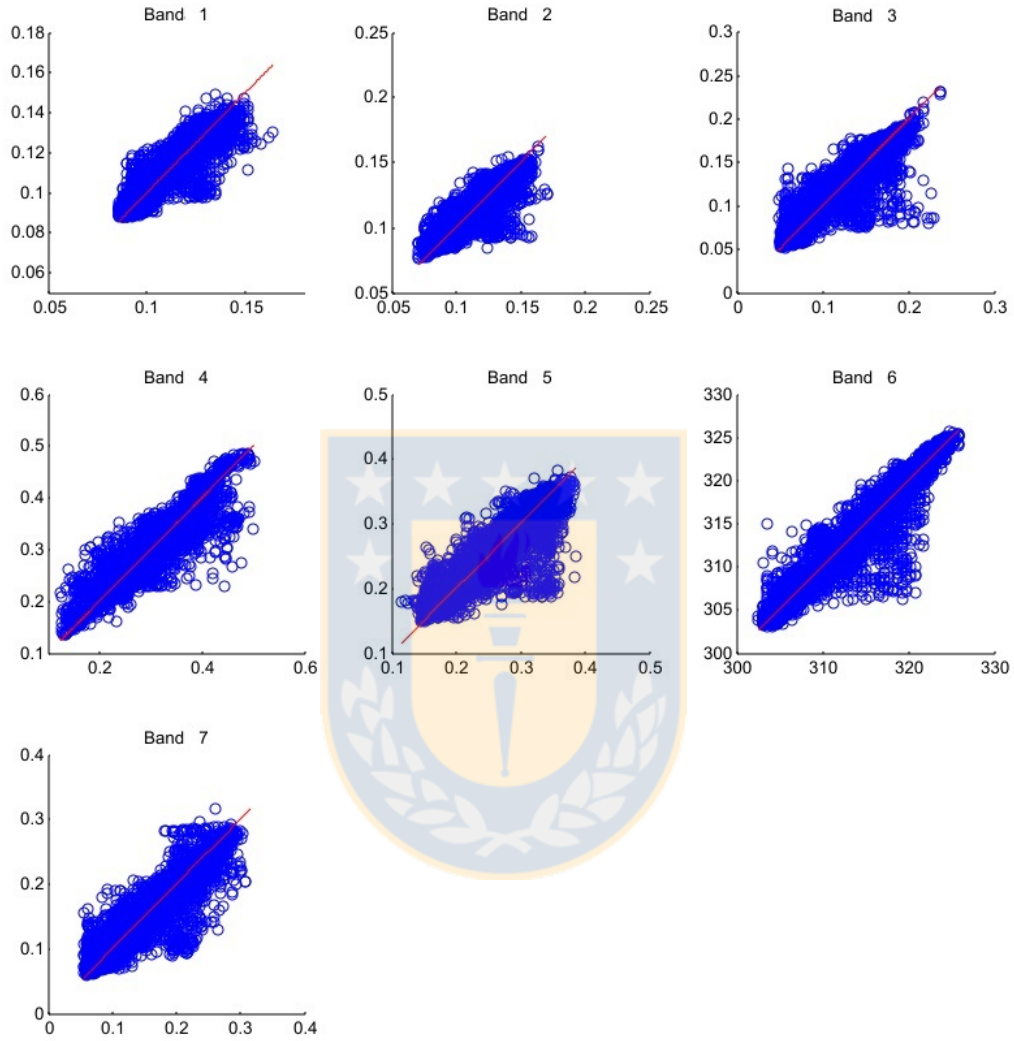

Figure C.4: Scatter plots of original (x axis) versus predicted (y axis) value by G-F$_{NSPI}$ methodology for each band. Unit for 1, 2, 3, 4, 5 and 7 bands is reflectance at top of atmosphere, while the unit for band 6 is Kelvin degrees.

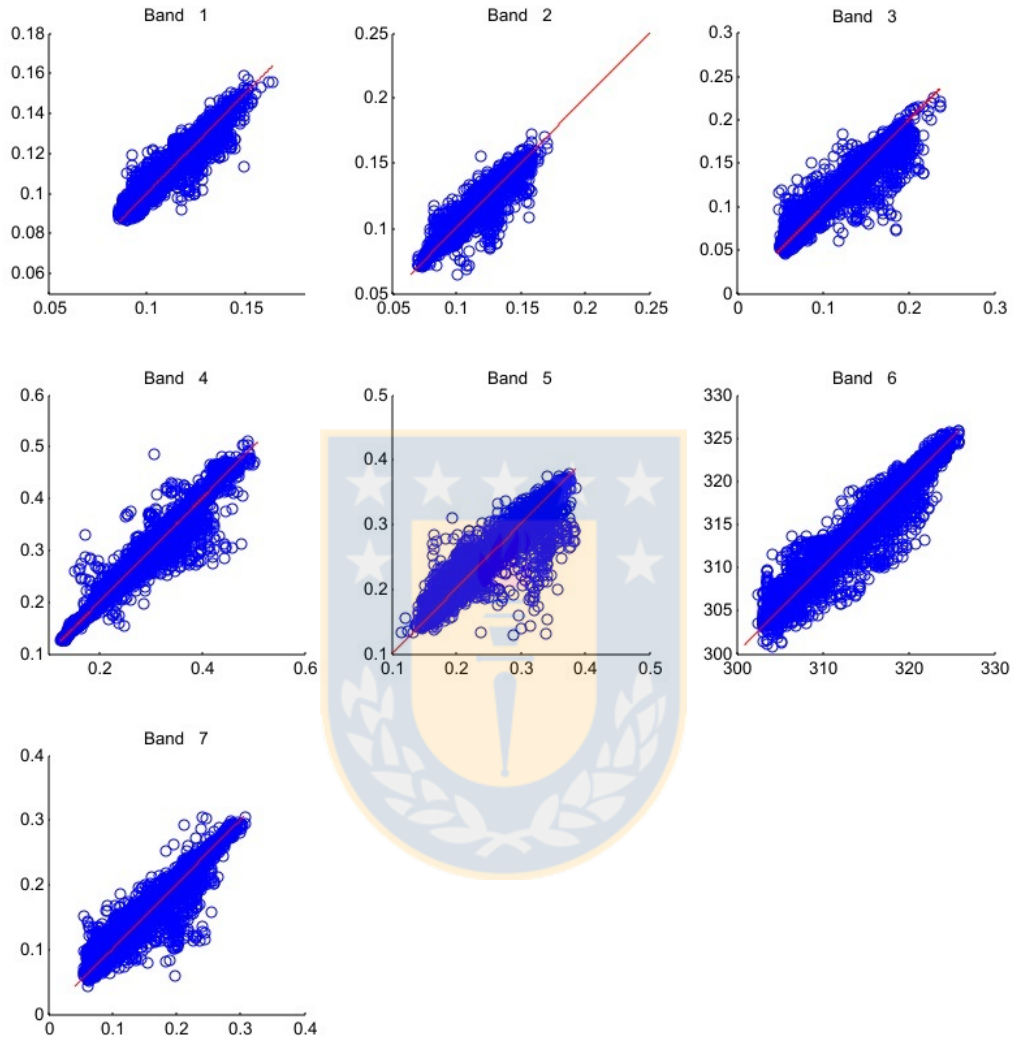

Figure C.5: Scatter plots of original (x axis) versus predicted (y axis) value by G-F$_{class}$ methodology for each band. Unit for 1, 2, 3, 4, 5 and 7 bands is reflectance at top of atmosphere, while the unit for band 6 is Kelvin degrees.

Appendix D

. METRIC model

D.1 Modelo METRIC

METRIC model uses satellite images and some data from meteorological stations to estimate ET as residual of the surface energy balance, where the latent heat flux is in function of net radiation, soil heat flux and sensible heat flux. The major advantage of METRIC is the calibration with the reference ET (ET_r) to estimate the sensible heat flux, which improves the ET estimation.

Data required by METRIC are: satellite image that includes the thermal band and information about image capture, and data from a meteorological station to estimate the ET_r in the instant of image capture using the standardized ASCE-EWRI Penman-Monteith procedure.

The surface energy balance is shown in the equation D.1, where LE ($\frac{W}{m^2}$) is the latent heat flux, Rn ($\frac{W}{m^2}$) is the net radiation, G ($\frac{W}{m^2}$) is the soil heat flux and H ($\frac{W}{m^2}$) is the sensible heat flux.

$$LE = Rn - G - H \tag{D.1}$$

Rn, albedo and the surface temperature, are estimate using satellite image information. To estimate the net radiation, the energy fluxes at the surface (equation D.2) are balanced. Where α is the albedo, Rs_{in} is the incoming solar radiation ($\frac{W}{m^2}$), Rl_{in} is the incoming long wave radiation ($\frac{W}{m^2}$), Rl_{out} is the outgoing long wave radiation ($\frac{W}{m^2}$) and ϵ_o is the surface thermal emissivity of broad band.

$$Rn = (1 - \alpha) * Rs_{in} + Rl_{in} - Rl_{out} - (1 - \epsilon_o) * Rl_{in} \tag{D.2}$$

Rs_{in} is estimated in function of the date, time and relative humidity in the time of image capture (equation D.3). Where Gsc is the solar constant (1367 $\frac{W}{m^2}$), θ is the angle of solar incidence, τ_{sw} is the atmospheric transmissivity of broad band.

$$Rs_{in} = \frac{Gsc * \cos\theta * \tau_{sw}}{d^2} \tag{D.3}$$

The outgoing long wave radiation (Rl_{out}) is estimated with the Stefan-Boltzmann equation (equation D.4). Where σ is the Stefan-Boltzmann constant ($5.67 * 10^{-8} \frac{W}{m^{2} * ^{\circ} K^{-4}}$), and T_s is the surface temperature in Kelvin degree.

$$Rl_{out} = \epsilon_0 * \sigma * T_s^4 \tag{D.4}$$

The surface temperature (T_s), in Kelvin degrees, is calculated with the equation D.5 developed by Markham and Barker (1986), which is a modification of Plank's equation. Where $k1$ ($^\circ K$) and $k2$ ($\frac{W}{m^2*\mu m*st}$) are constants for each sensor, Rc ($\frac{W}{m^2*\mu m*st}$) is the thermal radiance corrected by the effects of the atmosphere. ϵ_{NB} is the surface thermal emissivity in the narrow band (10.4 a 12.5 μm). ϵ_{NB} is calculated with an empiric model developed by Tasumi et al. (2003c).

$$T_s = \frac{k2}{\ln\left(\frac{\epsilon_{NB}*k1}{Rc}\right)+1} \tag{D.5}$$

Rc is obtained with equation D.6, based in Wukelic et al. (1989). Where L_6 is the thermal radiance ($\frac{W}{m^2*\mu m*st}$), Rp ($\frac{W}{m^2*\mu m*st}$) is the radiance emitted in the path from the surface to sensor; τ_{NB} is the air transmissivity in the narrow band and R_sky ($\frac{W}{m^2*\mu m*st}$) is the incoming thermal radiance from a clear sky in the narrow band.

$$Rc = \frac{L_6 - Rp}{\tau_{NB}} - (1-\epsilon_{NB}) * R_{sky} \tag{D.6}$$

Correction of L_6 is necessary due that in the path of the surface to the atmosphere there is a process that absorbs and reflects radiation. In addition, thermal radiation is emitted by the atmosphere in sensor direction, causing that the sensor erroneously captures this radiation together surface radiation. Rp and τ_{NB} need an atmospheric radiation transfer simulation model. In Allen et al. (2007), values of $Rp = 0.91$, $\tau_{NB} = 0.866$ and $R_{sky} = 1.32$ for clear sky conditions were suggested.

Incoming long wave radiation (Rl_{in}) is estimated with equation D.7, which is based in Stefan-Boltzmann equation. In equation refeq24, ϵ_a is the effective atmospheric emissivity and T_a is the near-surface temperature.

ϵ_a is estimated with an empiric equation developed in Bastiaanssen (1995) and the coefficients estimated in Allen et al. (2000) over alfalfa in Idaho (equation D.8). In the most of the METRIC applications, T_s is used like T_a.

$$Rl_{in} = \epsilon_a * \sigma * T_a^4 \tag{D.7}$$

$$\epsilon_a = 0.85 * (-\ln(\tau_{sw}))^{0.09} \tag{D.8}$$

Soil heat flux (G) is estimated with an empirical model developed by Bastiaanssen

(2000), that represents values for noonday (equation D.9). In which $NDVI$ (Normalized Difference Vegetation Index) is a vegetation index that shows the status of vegetation vigor (equation D.10). In the equation D.9 the value of surface temperature is Celsius degrees.

$$G/Rn = T_s * (0.0038 + 0.0074 * \alpha) * (1 - 0.98 * NDVI^4) \tag{D.9}$$

$$NDVI = \frac{\rho_{t,IFRC} - \rho_{t,R}}{\rho_{t,IFRC} + \rho_{t,R}} \tag{D.10}$$

H ($\frac{W}{m^2}$) is determined from the equation of heat transport (equation D.11), where the difference of temperature between the surface and air (dT), and aerodynamic resistance to heat transport (r_{ah}) present a major complication in the estimation. These complications are due that dT requires the surface and air temperatures for all pixels in the image; and the estimation of r_{ah} require to know the friction velocity (u^*) of each pixel. In the equation D.11 the parameter c_p corresponds to the specific heat of air, $1004\frac{J}{kg*^\circ K}$).

$$H = \frac{\rho * c_p * dT}{r_{ah}} \tag{D.11}$$

To estimate of r_{ah} requires an extrapolation of wind speed to an height where it can be assumed constant (200 $meters$), and an iterative correction process of stability based on the equations of Monin-Obhukov Allen (1996).

Two pixels with specific characteristics must be identified to implement the linear relationship described in Bastiaanssen (1995), Wang et al. (1995), Franks and Beven (1999) and Jacob et al. (2002). This relationship allows to obtain dT from the previously calculated surface temperature, using the equation D.12, where b corresponding to the intercept of the relationship with the axes of dT, while a is the slope of the relationship.

$$dT = b + a * T_s \tag{D.12}$$

The selected pixels are identified as hot and cold pixel. While the cold pixel corresponds to a pixel with a full vegetal cover and without water restrictions, while hot pixel corresponds to a pixel covered by agricultural bare soil without some irrigation. Using the relationship in equation D.12 can be estimated dT for the entire image with the coefficients a and b obtained from the hot and cold pixels. The values of a and b are estimated with the equations D.13 and D.14 respectively, where the subscripts *hot* and *cold* refer to the pixel values of the hot and cold pixel, respectively.

$$a = \frac{dT_{hot} - dT_{cold}}{T_{s-hot} - T_{s-cold}} \tag{D.13}$$

$$b = dT_{hot} - a * T_{s-hot} \tag{D.14}$$

$dT_{hot-cold}$ are estimated using the equation D.11, this equation requires values of $H_{hot-cold}$, $r_{ahhot-cold}$ and $\rho_{hot-cold}$. H_{hot} is estimated using the surface energy balance showed in equation D.1, assuming that hot pixel corresponds to a soil cover without vegetation and soil moisture, with LE equal or close to $0\frac{W}{m^2}$. Thus the balance is: $H_{hot} = Rn_{hot} - G_{hot}$. H_{cold} is estimated using the same procedure described above, except that the LE is assumed to be a 5 % higher than LE of meteorological station, i.e., the ET of cold pixel is 5 % higher than ET_r (considering alfalfa as reference crop) (Tasumi, 2003; Tasumi et al., 2005).

In summary, with the first iterative process that only consider the hot and cold pixels, is possible estimate the a and b values, that then are used in the equation D.12. Then is possible to estimate the instantaneous LE as residual of the surface energy balance.

To estimate the instantaneous ET (ET_{inst}) in $\frac{mm}{h}$ the equation D.15 can be used, where λ ($\frac{J}{kg}$) is the latent heat of vaporization, and can be estimated with the equation D.16.

$$ET_{inst} = 3600 * \frac{LE}{\lambda} \tag{D.15}$$

$$\lambda = (2.501 - 0.00236 * (T_s - 273)) * 10^6 \tag{D.16}$$

To transform the values from instantaneous ET to daily ET ($\frac{mm}{day}$), the concept of "fraction of the reference evapotranspiration" (ET_rF) is considered (Allen et al., 2007). ET_rF is estimated with the equation D.17.

$$ET_rF = \frac{ET_{inst}}{ET_r} \tag{D.17}$$

Extrapolated ET to daily period (ET_{24}) is estimated using the equation D.18, where ET_{r24} is the ET_r for the daily period estimated at the meteorological station.

$$ET_{24} = ET_rF * ET_{r24} \tag{D.18}$$

Bibliography

Achanta, R.; Shaji, A.; Smith, K.; Lucchi, A.; Fua, P. and Süsstrunk, S.: ≪SLIC Superpixels Compared to State-of-the-Art Superpixel Methods≫. *Pattern Analysis and Machine Intelligence, IEEE Transactions on*, 2012, **34(11)**, pp. 2274 –2282. ISSN 0162-8828.

Allen, R.: ≪Assessing integrity of weather data for use in reference evapotranspiration estimation≫. *J. Irrig. and Drain. Engrg,. ASCE.*, 1996, **122(2)**, pp. (97–106).

Allen, R.; M., Tasumi; Trezza, R. and Kjaersgaard, J.: *METRIC. Mapping Evapotranspiration at High Resolution. Applications Manual for Landsat Satellite Imagery.* University of Idaho, Kimberly, Idaho, version 2.0.5th edition, 2010.

Allen, RG; Hartogensis, O and de Bruin, H: ≪Long-wave radiation over alfalfa during the RAPID field campaign in southern Idaho≫. *Technical Report*, Research Report, Kimberly, Univ. of Idaho, Id, 2000.

Allen, R.G.; Tasumi, M. and Trezza, R.: ≪Satellite-based energy balance for mapping evapotranspiration with internalized calibration (METRIC). Model≫. *Journal of Irrigation and Drainage Engineering*, 2007, **133(4)**, pp. 380–394.

Allen, Richard G.; Burnett, Boyd; Kramber, William; Huntington, Justin; Kjaersgaard, Jeppe; Kilic, Ayse; Kelly, Carlos and Trezza, Ricardo: ≪Automated Calibration of the METRIC-Landsat Evapotranspiration Process≫. *JAWRA Journal of the American Water Resources Association*, 2013, **49(3)**, pp. 563–576. ISSN 1752-1688.

Allen, Richard G; Pereira, LS; Raes, D and Smith, M: ≪FAO Irrigation and drainage paper No. 56≫. *Rome: Food and Agriculture Organization of the United Nations*, 1998, pp. 26–40.

Allen, Richard G; Pereira, Luis S; Howell, Terry A and Jensen, Marvin E: ≪Evapotranspiration information reporting: I. Factors governing measurement accuracy≫. *Agricultural Water Management*, 2011, **98(6)**, pp. 899–920.

Allen, TF: *Hierarchy: perspectives for ecological complexity/TFH Allen and Thomas B. Starr*. Chicago:, University of Chicago Press, 1982.

Anderson, James Richard: *A land use and land cover classification system for use with remote sensor data*. volume 964. US Government Printing Office, 1976.

Awan, Usman Khalid; Tischbein, Bernhard; Conrad, Christopher; Martius, Christopher and Hafeez, Mohsin: ≪Remote sensing and hydrological measurements for irrigation performance assessments in a water user association in the Lower Amu Darya River Basin≫. *Water resources management*, 2011, **25(10)**, pp. 2467–2485.

Aydin, Mehmet and Keçecioğlu, Suzan Filiz: ≪Sensitivity analysis of the evaporation module of the E-DiGOR model≫. *Turkish Journal of Agriculture and Forestry*, 2010, **34(6)**, pp. 497–507.

Baatz, M; Benz, U; Dehghani, S; Heynen, M; Höltje, A; Hofmann, P; Lingenfelder, I; Mimler, M; Sohlbach, M; Weber, M et al.: ≪eCognition professional user guide 4≫. *Definiens Imaging, Munich*, 2004.

Baatz, Martin and Schäpe, Arno: ≪Multiresolution segmentation: an optimization approach for high quality multi-scale image segmentation≫. *Angewandte Geographische Informationsverarbeitung XII*, 2000, pp. 12–23.

Bastiaanssen, W.: ≪Regionalization of surface flux densities and moisture indicators in composite terrain: A remote sensing approach under clear skies in Mediterranean climates.≫ *Ph.D. dissertation, CIP Data Koninklijke Bibliotheek, Den Haag, The Netherlands*, 1995, p. p273.

Bastiaanssen, WGM: ≪SEBAL-based sensible and latent heat fluxes in the irrigated Gediz Basin, Turkey≫. *Journal of hydrology*, 2000, **229(1)**, pp. 87–100.

Bastiaanssen, W.G.M.; Meneti, M.; Feddes, R.A. and Holtslag, A.: ≪A remote sensing surface energy balance algorithm for land (SEBAL). Formulation≫. *Journal of Hydrology*, 1998a, **212-213**, pp. 198–212.

Bastiaanssen, WGM; Noordman, EJM; Pelgrum, H; Davids, G; Thoreson, BP and Allen, RG: «SEBAL model with remotely sensed data to improve water-resources management under actual field conditions». *Journal of Irrigation and Drainage Engineering*, 2005, **131(1)**, pp. 85–93.

Bastiaanssen, W.G.M.; Pelgrum, H.; Wang, J.; Ma, Y.; Moreno, J.; Roerink, G. and Van der Wal, T.: «A remote sensing surface energy balance algorithm for land (SEBAL). Validation». *Journal of Hydrology*, 1998b, **212-213**, pp. 213–219.

Bauer, Eric and Kohavi, Ron: «An empirical comparison of voting classification algorithms: Bagging, boosting, and variants». *Machine learning*, 1999, **36(1-2)**, pp. 105–139.

Benz, Ursula C; Hofmann, Peter; Willhauck, Gregor; Lingenfelder, Iris and Heynen, Markus: «Multi-resolution, object-oriented fuzzy analysis of remote sensing data for GIS-ready information». *ISPRS Journal of photogrammetry and remote sensing*, 2004, **58(3)**, pp. 239–258.

Blaschke, T.: «Object based image analysis for remote sensing». *ISPRS Journal of Photogrammetry and Remote Sensing*, 2010, **65(1)**, pp. 2–16.

Blaschke, Thomas: «Object-based contextual image classification built on image segmentation». In: *Advances in Techniques for Analysis of Remotely Sensed Data, 2003 IEEE Workshop on*, pp. 113–119. IEEE, 2003.

Breiman, L.: «Random Forests». *Machine Learning*, 2001, **45**, pp. 5–32.

Breiman, Leo: «Bagging predictors». *Machine Learning*, 1996, **24(2)**, pp. 123–140.

Burkhalter, J Philip; Martin, Timothy C; Allen, Richard G; Kjaersgaard, Jeppe; Wilson, Erin; Alvarado, Ray and Polly, Jason S: «Estimating crop water use via remote sensing techniques vs. conventional methods in the South Platte River Basin, Colorado». *JAWRA Journal of the American Water Resources Association*, 2013, **49(3)**, pp. 498–517.

Burnett, C. and Blaschke, T.: «A multi-scale segmentation/object relationship modelling methodology for landscape analysis». *Ecological modelling*, 2003, **168(3)**, pp. 233–249.

Castillejo-González, I.L.; López-Granados, F.; García-Ferrer, A.; Peña-Barragán, J.M.; Jurado-Expósito, M.; de la Orden, M.S. and González-Audicana, M.: ≪Object-and pixel-based analysis for mapping crops and their agro-environmental associated measures using QuickBird imagery≫. *Computers and Electronics in Agriculture*, 2009, **68(2)**, pp. 207–215.

Chan, Jonathan Cheung-Wai and Paelinckx, Desiré: ≪Evaluation of Random Forest and Adaboost tree-based ensemble classification and spectral band selection for ecotope mapping using airborne hyperspectral imagery≫. *Remote Sensing of Environment*, 2008, **112(6)**, pp. 2999–3011.

Chen, J.; Zhu, X.; Vogelmann, J.E.; Gao, F. and Jin, S.: ≪A simple and effective method for filling gaps in Landsat ETM+ SLC-off images≫. *Remote Sensing of Environment*, 2011.

Chitiboi, T; Hennemuth, A; Tautz, L; Stolzmann, P; Donati, O F; Linsen, L and Hahn, H K: ≪Automatic detection of myocardial perfusion defects using object-based myocardium segmentation≫. In: *Computing in Cardiology Conference (CinC), 2013*, pp. 639–642, 2013.

Choi, Minha; Kustas, William P; Anderson, Martha C; Allen, Richard G; Li, Fuqin and Kjaersgaard, Jeppe H: ≪An intercomparison of three remote sensing-based surface energy balance algorithms over a corn and soybean production region (Iowa, US) during SMACEX≫. *Agricultural and forest meteorology*, 2009, **149(12)**, pp. 2082–2097.

Choragudi, Venkata Naga Ravi Kumar: ≪Sensitivity Analysis on Mapping EvapoTranspiration at High Resolution Using Internal Calibration (METRIC)≫. *Civil Engineering Theses, Dissertations, and Student Research. Paper 35. http://digitalcommons.unl.edu/civilengdiss/35*, 2011.

Chuvieco, E.: *Teledetección Ambiental: La observación de la Tierra desde el Espacio*. Ariel Ciencia, Barcelona, 2002.

Cieslak, David A and Chawla, Nitesh V: ≪Start globally, optimize locally, predict globally: Improving performance on imbalanced data≫. In: *Data Mining, 2008. ICDM'08. Eighth IEEE International Conference on*, pp. 143–152. IEEE, 2008.

Ciren: ≪Estudio agrologico VI Región, Descripciones de suelos≫. *Technical Report*, Ciren, 1996.

Ciren: ≪Estudio agrologico VIII Región, Descripciones de suelos≫. *Technical Report*, Ciren, 1999.

Coll, César; Galve, Joan Miquel; Sanchez, Juan Manuel and Caselles, Vicente: ≪Validation of Landsat-7/ETM+ thermal-band calibration and atmospheric correction with ground-based measurements≫. *Geoscience and Remote Sensing, IEEE Transactions on*, 2010, **48(1)**, pp. 547–555.

Corcoran, Jennifer; Knight, Joseph; Pelletier, Keith; Rampi, Lian and Wang, Yan: ≪The Effects of Point or Polygon Based Training Data on RandomForest Classification Accuracy of Wetlands≫. *Remote Sensing*, 2015, **7(4)**, pp. 4002–4025.

Droogers, Peter; Immerzeel, WW and Lorite, IJ: ≪Estimating actual irrigation application by remotely sensed evapotranspiration observations≫. *Agricultural Water Management*, 2010, **97(9)**, pp. 1351–1359.

Espindola, GM; Camara, G; Reis, IA; Bins, LS and Monteiro, AM: ≪Parameter selection for region-growing image segmentation algorithms using spatial autocorrelation≫. *International Journal of Remote Sensing*, 2006, **27(14)**, pp. 3035–3040.

Estévez, Javier; Gavilán, Pedro and Berengena, Joaquín: ≪Sensitivity analysis of a Penman–Monteith type equation to estimate reference evapotranspiration in southern Spain≫. *Hydrological processes*, 2009, **23(23)**, pp. 3342–3353.

Foken, Th; Wimmer, F; Mauder, M; Thomas, C and Liebethal, C: ≪Some aspects of the energy balance closure problem≫. *Atmospheric Chemistry and Physics*, 2006, **6(12)**, pp. 4395–4402.

Foken, Thomas: ≪The energy balance closure problem: An overview≫. *Ecological Applications*, 2008, **18(6)**, pp. 1351–1367.

Folhes, MT; Rennó, CD and Soares, JV: ≪Remote sensing for irrigation water management in the semi-arid Northeast of Brazil≫. *Agricultural Water Management*, 2009, **96(10)**, pp. 1398–1408.

Franks, S. W. and Beven, K.: «Conditioning a multiple-patch SVAT model using uncertain time-space estimates of latent heat flux as inferred from remotely sensed data». *Water Resources Research*, 1999, **35(9)**, pp. (2751–2761).

Galar, Mikel; Fernandez, Alberto; Barrenechea, Edurne; Bustince, Humberto and Herrera, Francisco: «A review on ensembles for the class imbalance problem: bagging-, boosting-, and hybrid-based approaches». *Systems, Man, and Cybernetics, Part C: Applications and Reviews, IEEE Transactions on*, 2012, **42(4)**, pp. 463–484.

Gao, Y. and Mas, J.F.: «A comparison of the performance of pixel-based and object-based classifications over images with various spatial resolutions». *Online Journal of Earth Sciences*, 2008, **2(1)**, pp. 27–35.

García, Gladys Tahiri Santis; Tahiri, Gladys et al.: *Mapa de reconocimiento de suelos de la Región de Bío-Bío (sector norte)*. Ph.D. thesis, Universidad de Chile, 2005.

Gelybó, Gy; Barcza, Z; Kern, A and Kljun, N: «Effect of spatial heterogeneity on the validation of remote sensing based GPP estimations». *Agricultural and Forest Meteorology*, 2013, **174**, pp. 43–53.

Gong, Lebing; Xu, Chong-yu; Chen, Deliang; Halldin, Sven and Chen, Yongqin David: «Sensitivity of the Penman–Monteith reference evapotranspiration to key climatic variables in the Changjiang (Yangtze River) basin». *Journal of Hydrology*, 2006, **329(3)**, pp. 620–629.

Gonzalez, Rafael C; Woods, Richard E and Eddins, Steven L: *Digital image processing using MATLAB*, 2004.

Gowda, Prasanna; Chavez, Jose; Colaizzi, Paul; Evett, Steve; Howell, Terry and Tolk, Judy: «ET mapping for agricultural water management: present status and challenges». *Irrigation Science*, 2008, **26(3)**, pp. 223–237.

Hay, GJ and Castilla, G.: «Geographic Object-Based Image Analysis (GEOBIA): A new name for a new discipline». *Object-Based Image Analysis*, 2008, pp. 75–89.

Hemakumara, HM; Chandrapala, Lalith and Moene, Arnold F: «Evapotranspiration fluxes over mixed vegetation areas measured from large aperture scintillometer». *Agricultural water management*, 2003, **58(2)**, pp. 109–122.

Homer, Collin; Huang, Chengquan; Yang, Limin; Wylie, Bruce and Coan, Michael: «Development of a 2001 national land-cover database for the United States». *Photogrammetric Engineering & Remote Sensing*, 2004, **70(7)**, pp. 829–840.

Homeyer A, Hahn H, Schwier M: «A Generic Concept for Object-based Image Analysis». In: *In VISAPP, 2010*, pp. 530–33, 2010.

Hsieh, C.I.; Katul, G. and Chi, T.: «An approximate analytical model for footprint estimation of scalar fluxes in thermally stratified atmospheric flows». *Advances in Water Resources*, 2000, **23(7)**, pp. 765–772.

Huang, Chengquan; Wylie, Bruce; Yang, Limin; Homer, Collin and Zylstra, Gregory: «Derivation of a tasselled cap transformation based on Landsat 7 at-satellite reflectance». *International Journal of Remote Sensing*, 2002, **23(8)**, pp. 1741–1748.

Jacob, F.; Olioso, A.; Gu, X. F.; Su, Z. and Seguin, B.: «Mapping surface fluxes using airborne visible, near infrared, thermal infrared remote sensing data as a spatialized surface energy balance model.» *Agronomie*, 2002, **22**, pp. (669–680).

Jacob, Frédéric; Petitcolin, François; Schmugge, Thomas; Vermote, Eric; French, Andrew and Ogawa, Kenta: «Comparison of land surface emissivity and radiometric temperature derived from MODIS and ASTER sensors». *Remote Sensing of Environment*, 2004, **90(2)**, pp. 137–152.

Johansen, K; Bartolo, R and Phinn, S: «SPECIAL FEATURE–Geographic Object-Based Image Analysis». *Journal of Spatial Science*, 2010, **55(1)**, pp. 3–7.

Johnson, Brian and Xie, Zhixiao: «Unsupervised image segmentation evaluation and refinement using a multi-scale approach». *ISPRS-J. Photogramm. Remote Sens.*, 2011, **66(4)**, pp. 473–483.

Ju, J. and Roy, D.P.: «The availability of cloud-free Landsat ETM+ data over the conterminous United States and globally». *Remote Sensing of Environment*, 2008, **112(3)**, pp. 1196–1211.

Kamble, Baburao; Irmak, Ayse; Hubbard, Kenneth; Gowda, Prasanna et al.: «Irrigation scheduling using remote sensing data assimilation approach». *Advances in Remote Sensing*, 2013, **2(03)**, p. 258.

Kim, Minho; Madden, Marguerite; Warner, Timothy A et al.: ≪Forest type mapping using object-specific texture measures from multispectral IKONOS imagery: Segmentation quality and image classification issues≫. *Photogramm. Eng. Remote Sens.*, 2009, **75(7)**, pp. 819–829.

Körting, Thales Sehn; Câmara, Gilberto and Fonseca, Leila Maria Garcia: ≪Land Cover Detection Using Temporal Features Based On Polar Representation≫, 2012.

Kuncheva, Ludmila I and Rodríguez, Juan J: ≪A weighted voting framework for classifiers ensembles≫. *Knowledge and Information Systems*, 2014, **38(2)**, pp. 259–275.

Kustas, W.P. and Norman, J.M.: ≪Evaluation of soil and vegetation heat flux predictions using a simple two-source model with radiometric temperatures for partial canopy cover≫. *Agricultural and Forest Meteorology*, 1999, **94(1)**, pp. 13–29.

Leblon, Brigitte; Gallant, Lisa and Granberg, Hardy: ≪Effects of shadowing types on ground-measured visible and near-infrared shadow reflectances≫. *Remote Sensing of Environment*, 1996, **58(3)**, pp. 322–328.

Levin, S.A.: ≪The problem of pattern and scale in ecology: the Robert H. MacArthur award lecture≫. *Ecology*, 1992, **73(6)**, pp. 1943–1967.

Li, Fuqin; Kustas, William P; Anderson, Martha C; Prueger, John H and Scott, Russell L: ≪Effect of remote sensing spatial resolution on interpreting tower-based flux observations≫. *Remote Sensing of Environment*, 2008, **112(2)**, pp. 337–349.

Loheide, S.P. and Gorelick, S.M.: ≪A local-scale, high-resolution evapotranspiration mapping algorithm (ETMA) with hydroecological applications at riparian meadow restoration sites≫. *Remote Sensing of Environment*, 2005, **98(2)**, pp. 182–200.

Long, Di and Singh, Vijay P: ≪Assessing the impact of end-member selection on the accuracy of satellite-based spatial variability models for actual evapotranspiration estimation≫. *Water Resources Research*, 2013, **49(5)**, pp. 2601–2618.

Long, Di; Singh, Vijay P and Li, Zhao-Liang: ≪How sensitive is SEBAL to changes in input variables, domain size and satellite sensor?≫ *Journal of Geophysical Research*, 2011, **116(D21)**, p. D21107.

Lu, Dengsheng and Weng, Qihao: ≪A survey of image classification methods and techniques for improving classification performance≫. *International journal of Remote sensing*, 2007, **28(5)**, pp. 823–870.

Lucchi, A; Smith, K; Achanta, R; Knott, G and Fua, P: ≪Supervoxel-Based Segmentation of Mitochondria in EM Image Stacks With Learned Shape Features≫. *IEEE Trans. Med. Imaging*, 2012, **31(2)**, pp. 474–486.

Markham, B. L. and Barker, J. L.: ≪Landsat MSS and TM postcalibration dynamic ranges, exoatmospheric reflectances and at-satellite temperatures.≫ *EOSAT Landsat Technical Notes*, 1986, **1**, pp. 3–8.

McCuen, R.H.: ≪A SENSITIVITY AND ERROR ANALYSIS CF PROCEDURES USED FOR ESTIMATING EVAPORATION1≫. *JAWRA Journal of the American Water Resources Association*, 1974, **10(3)**, pp. 486–497.

Meneti, M. and Choudhary, BJ: ≪Parameterization of land surface evapotranspiration using a location dependent potential evapotranspiration and surface temperature range. Exchange Processes at the land Surface for a Range of Space and time series, Bolle, HJ, Feddes, RA, and Kalma, JD≫. *International Association of Hydrological Sciences Publication*, 1993, **212**, pp. 561–568.

Morton, Charles G: *Assessing Calibration Uncertainty and Automation for Estimating Evapotranspiration from Agricultural Areas Using METRIC*. Ph.D. thesis, Department of Geography, University of Nevada, 2013.

Novoa, R.; Villaseca, S.; del Canto, P.; Rouanet, J. and y A. del Pozo, C. Sierra: ≪Mapa Agroclimático de Chile, INIA≫. *Santiago, Chile.*, 1989.

Otukei, JR and Blaschke, T: ≪Land cover change assessment using decision trees, support vector machines and maximum likelihood classification algorithms≫. *International Journal of Applied Earth Observation and Geoinformation*, 2010, **12**, pp. S27–S31.

Pal, M: ≪Random forest classifier for remote sensing classification≫. *International Journal of Remote Sensing*, 2005, **26(1)**, pp. 217–222.

Peña Barragan, J.M.; Ngugi, M.K.; Plant, R.E. and Six, J.: ≪Object-based crop identification using multiple vegetation indices, textural features and crop phenology≫. *Remote Sensing of Environment*, 2011.

Perrier, Alain: ≪Land surface processes: vegetation≫. *Land surface processes in atmospheric general circulation models*, 1982, pp. 395–448.

Pôças, Isabel; Nogueira, António; Paço, Teresa A; Sousa, Adélia; Valente, Fernanda; Silvestre, José; Andrade, José A; Santos, Francisco L; Pereira, Luís S and Allen, Richard G: ≪METRIC model for the estimation and mapping of evapotranspiration in a super intensive olive orchard in Southern Portugal≫. In: *EGU General Assembly Conference Abstracts*, volume 15, p. 4280, 2013.

Poças, Isabel; Paço, Teresa A; Cunha, Mário; Andrade, José A; Silvestre, José; Sousa, Adélia; Santos, Francisco L; Pereira, Luís S and Allen, Richard G: ≪Satellite-based evapotranspiration of a super-intensive olive orchard: Application of METRIC algorithms≫. *Biosystems Engineering*, 2014.

Prasad, Anantha M; Iverson, Louis R and Liaw, Andy: ≪Newer classification and regression tree techniques: bagging and random forests for ecological prediction≫. *Ecosystems*, 2006, **9(2)**, pp. 181–199.

Rodriguez-Galiano, VF; Chica-Olmo, M; Abarca-Hernandez, F; Atkinson, PM and Jeganathan, C: ≪Random Forest classification of Mediterranean land cover using multi-seasonal imagery and multi-seasonal texture≫. *Remote Sensing of Environment*, 2012a, **121**, pp. 93–107.

Rodriguez-Galiano, VF; Ghimire, B; Rogan, J; Chica-Olmo, M and Rigol-Sanchez, JP: ≪An assessment of the effectiveness of a random forest classifier for land-cover classification≫. *ISPRS Journal of Photogrammetry and Remote Sensing*, 2012b, **67**, pp. 93–104.

Rooney, GG: ≪Comparison of upwind land use and roughness length measured in the urban boundary layer≫. *Boundary-layer meteorology*, 2001, **100(3)**, pp. 469–485.

Santos, C; Lorite, Ignacio J; Tasumi, M; Allen, RG and Fereres, E: ≪Performance assessment of an irrigation scheme using indicators determined with remote sensing techniques≫. *Irrigation science*, 2010, **28(6)**, pp. 461–477.

Santos, C; Lorite, IJ; Allen, RG and Tasumi, M: «Aerodynamic parameterization of the satellite-based energy balance (METRIC) model for ET estimation in rainfed olive orchards of Andalusia, Spain». *Water resources management*, 2012, **26(11)**, pp. 3267–3283.

Santos, C; Lorite, IJ; Tasumi, M; Allen, RG and Fereres, E: «Integrating satellite-based evapotranspiration with simulation models for irrigation management at the scheme level». *Irrigation Science*, 2008, **26(3)**, pp. 277–288.

Scaramuzza, P.; Micijevic, E. and Chander, G.: «SLC gap-filled products: Phase one methodology». *USGS Landsat 7 Technical Documentation,¡ http://landsat. usgs. gov/resources/files/SLC_Gap_Fill_Methodology. pdf*, 2004.

Sexton, Joseph O; Urban, Dean L; Donohue, Michael J and Song, Conghe: «Long-term land cover dynamics by multi-temporal classification across the Landsat-5 record». *Remote Sensing of Environment*, 2013, **128**, pp. 246–258.

Shackelford, Aaron K and Davis, Curt H: «A hierarchical fuzzy classification approach for high-resolution multispectral data over urban areas». *Geoscience and Remote Sensing, IEEE Transactions on*, 2003, **41(9)**, pp. 1920–1932.

Singh, Ramesh K and Irmak, Ayse: «Estimation of crop coefficients using satellite remote sensing». *Journal of Irrigation and Drainage Engineering*, 2009, **135(5)**, pp. 597–608.

Singh, Ramesh K and Irmak, Ayse: «Treatment of anchor pixels in the METRIC model for improved estimation of sensible and latent heat fluxes». *Hydrological sciences journal*, 2011, **56(5)**, pp. 895–906.

Singh, Ramesh K; Liu, Shuguang; Tieszen, Larry L; Suyker, Andrew E and Verma, Shashi B: «Estimating seasonal evapotranspiration from temporal satellite images». *Irrigation Science*, 2012, **30(4)**, pp. 303–313.

Storey, J.; Scaramuzza, P.; Schmidt, G. and Barsi, J.: «Landsat 7 scan line corrector-off gap filled product development». In: *Pecora*, volume 16, pp. 23–27, 2005.

Sun, Ju; Wu, Xiao; Yan, Shuicheng; Cheong, Loong-Fah; Chua, Tat-Seng and Li, Jintao: «Hierarchical spatio-temporal context modeling for action recognition». In:

Computer Vision and Pattern Recognition, 2009. CVPR 2009. IEEE Conference on, pp. 2004–2011. IEEE, 2009.

Tang, Qiuhong; Peterson, Shannon; Cuenca, Richard H; Hagimoto, Yutaka and Lettenmaier, Dennis P: ≪Satellite-based near-real-time estimation of irrigated crop water consumption≫. *Journal of Geophysical Research: Atmospheres (1984–2012)*, 2009, **114(D5)**.

Tasumi, M.: ≪Progress in operational estimation of regional evapotranspiration using satellite imagery.≫ *Ph. D. Dissertation, University of Idaho, Moscow, ID*, 2003.

Tasumi, M.; Allen, R.G. and Trezza, R.: ≪At-surface albedo from Landsat and MODIS satellites for use in energy balance studies of evapotranspiration≫. *Journal of Hydrolog. Eng.*, 2008, **13**, pp. (51–63).

Tasumi, M.; Trezza, R. and Allen, R.: ≪Development of Emissivity Equations. Appendix 2 of Tasumi (2003), Progress in operational estimation of regional evapotranspiration using satellite imagery.≫ *Ph. D. Dissertation, University of Idaho, Moscow, ID.*, 2003c, pp. (p239–247).

Tasumi, Masahiro; Allen, Richard G; Trezza, Ricardo and Wright, James L: ≪Satellite-based energy balance to assess within-population variance of crop coefficient curves≫. *Journal of Irrigation and Drainage Engineering*, 2005, **131(1)**, pp. 94–109.

Trias-Sanz, Roger; Stamon, Georges and Louchet, Jean: ≪Using colour, texture, and hierarchial segmentation for high-resolution remote sensing≫. *ISPRS-J. Photogramm. Remote Sens.*, 2008, **63(2)**, pp. 156–168.

Twine, Tracy E; Kustas, WP; Norman, JM; Cook, DR; Houser, PRea; Meyers, TP; Prueger, JH; Starks, PJ and Wesely, ML: ≪Correcting eddy-covariance flux underestimates over a grassland≫. *Agricultural and Forest Meteorology*, 2000, **103(3)**, pp. 279–300.

Vieira, M.A.; Formaggio, A.R.; Rennó, C.D.; Atzberger, C.; Aguiar, D.A. and Mello, M.P.: ≪Object Based Image Analysis and Data Mining applied to a remotely sensed Landsat time-series to map sugarcane over large areas≫. *Remote Sens. Environ.*, 2012, **123**, pp. 553–562.

Walker, Wayne S; Stickler, Claudia M; Kellndorfer, Josef M; Kirsch, Katie M and Nepstad, Daniel C: ≪Large-area classification and mapping of forest and land cover in the Brazilian Amazon: A comparative analysis of ALOS/PALSAR and Landsat data sources≫. *Selected Topics in Applied Earth Observations and Remote Sensing, IEEE Journal of*, 2010, **3(4)**, pp. 594–604.

Walter, Ivan A; Allen, Richard G; Elliott, Ronald; Itenfisu, Daniel; Brown, Paul; Jensen, Marvin E; Mecham, Brent; Howell, Terry A; Snyder, Richard; Eching, Simon et al.: ≪Task Committee on Standardization of Reference Evapotranspiration≫, 2005.

Wang, J.; Ma, J.; Menenti, M.; Bastiaanssen, W. and Mitsuta, Y.: ≪The scaling up of land surface processes over a heterogeneous landscape with satellite observations.≫ *J. Meteorol. Soc. Jpn.*, 1995, **73(6)**, pp. (1235–1244).

Wang, J; Sammis, TW; Gutschick, VP; Gebremichael, M and Miller, DR: ≪Sensitivity analysis of the surface energy balance algorithm for land (SEBAL)≫. *Transactions of the ASABE*, 2009, **52(3)**, pp. 801–811.

Webb, EK; Pearman, GI; Leuning, R et al.: ≪Correction of flux measurements for density effects due to heat and water vapour transfer≫. *Quarterly Journal of the Royal Meteorological Society*, 1980, **106(447)**, pp. 85–100.

Whiteside, Timothy G.; Boggs, Guy S. and Maier, Stefan W.: ≪Comparing object-based and pixel-based classifications for mapping savannas≫. *International Journal of Applied Earth Observation and Geoinformation*, 2011, **13(6)**, pp. 884 – 893. ISSN 0303-2434.

Wilczak, James M; Oncley, Steven P and Stage, Steven A: ≪Sonic anemometer tilt correction algorithms≫. *Boundary-Layer Meteorology*, 2001, **99(1)**, pp. 127–150.

Wilson, Kell; Goldstein, Allen; Falge, Eva; Aubinet, Marc; Baldocchi, Dennis; Berbigier, Paul; Bernhofer, Christian; Ceulemans, Reinhart; Dolman, Han; Field, Chris et al.: ≪Energy balance closure at FLUXNET sites≫. *Agricultural and Forest Meteorology*, 2002, **113(1)**, pp. 223–243.

Wukelic, G. E.; Gibbons, D. E.; Martucci, L. M. and Foote, H. P.:

≪Radiometric calibration of Landsat thematic mapper thermal band≫. *Remote Sensing of Environment*, 1989, **28**, pp. (339–347).

Xu, Hanqiu: ≪Modification of normalised difference water index (NDWI) to enhance open water features in remotely sensed imagery≫. *International Journal of Remote Sensing*, 2006, **27(14)**, pp. 3025–3033.

Yan, Gao; Mas, J-F; Maathuis, BHP; Xiangmin, Zhang and Van Dijk, PM: ≪Comparison of pixel-based and object-oriented image classification approaches. A case study in a coal fire area, Wuda, Inner Mongolia, China≫. *International Journal of Remote Sensing*, 2006, **27(18)**, pp. 4039–4055.

Zeng, Chao; Shen, Huanfeng and Zhang, Liangpei: ≪Recovering missing pixels for Landsat ETM+ SLC-off imagery using multi-temporal regression analysis and a regularization method≫. *Remote Sensing of Environment*, 2013, **131**, pp. 182–194.

Zhou, Weiqi and Troy, Austin: ≪Development of an object-based framework for classifying and inventorying human-dominated forest ecosystems≫. *Int. J. Remote Sens.*, 2009, **30(23)**, pp. 6343–6360.

Zwart, Sander J and Leclert, Lucie MC: ≪A remote sensing-based irrigation performance assessment: a case study of the Office du Niger in Mali≫. *Irrigation Science*, 2010, **28(5)**, pp. 371–385.